UNIVERSITY OF SOUTHAMPTON

FACULTY OF PHYSICAL AND APPLIED SCIENCES

Physics

Quantitative modelling of fine scale auroral emissions and electric fields at sub-second resolution

by

Sam Arthur Tuttle

Thesis for the degree of Doctor of Philosophy

October 2017

UNIVERSITY OF SOUTHAMPTON

ABSTRACT

FACULTY OF PHYSICAL AND APPLIED SCIENCES
Physics

Doctor of Philosophy

QUANTITATIVE MODELLING OF FINE SCALE AURORAL EMISSIONS AND ELECTRIC FIELDS AT SUB-SECOND RESOLUTION

by Sam Arthur Tuttle

The structuring and dynamics of auroral emissions at fine spatial and temporal scales, down to tens of metres and fractions of a second, is an oft-observed but poorly understood phenomenon. One particular theory for such fine scale structure involves magnetic reconnection in the auroral acceleration region initiating Alfvén waves which structure and energise the precipitating particles. Such theories are testable using measurements of the ionospheric electric fields associated with the observed fine scale structure. This thesis presents attempts to measure ionospheric electric fields, using a novel model that tracks emission from a long-lived ion produced at times of auroral particle precipitation, so that the theories that seek to explain the fine scale structuring of the aurora can be evaluated. However, such modelling requires knowledge of the energy spectrum of the precipitation, and the resulting emissions, at the spatial and temporal resolutions of the observed fine scale aurora.

This thesis presents such new work concerning the modelling of auroral electron energy spectra and fine scale auroral emissions at sub-kilometre and sub-second resolutions using ground based observations, and the subsequent application of a novel method to estimate ionospheric electric fields using a long-lived ion produced during times of auroral precipitation. Two novel methods are presented. The first method utilises a fusion of multi-monochromatic auroral observations at optical and near-infrared (NIR) wavelengths together with simultaneous radar observations. The second uses only multi-monochromatic observations, to be used when complementary radar observations are unavailable. Each technique is applied to an observed auroral event to determine the energy spectra of the precipitating electrons and resulting 3-D distribution of auroral emissions. Modelled images of the emissions verify the accuracy of the recovered spectra.

The recovered spectra are used as input to a novel model which solves the continuity equation of a long-lived ion produced at times of auroral precipitation. This model uses a parameterised ion velocity, and optimises the velocity parameters by comparing observed and modelled images of emission from this ion. A simple velocity parameterisation, a uniform flow perpendicular to the magnetic field, yields plasma velocities of 0.4-2.4 km s^{-1}, with the plasma velocities being enhanced at times when the auroral brightness is high. Comparison of the recovered velocities to radar observations of ionospheric plasma velocities shows agreement in direction, but the recovered velocities are larger, more so when the aurora is brighter. Electric fields, inferred from the modelled plasma velocities, of up to 120 mV m^{-1} are found at the time when the auroral brightness was intensified. A more complex flow parameterisation is presented and tested, but does not succeed for the event analysed.

Contents

List of Figures

List of Tables

Declaration of Authorship

I, Sam Arthur Tuttle , declare that the thesis entitled *Quantitative modelling of fine scale auroral emissions and electric fields at sub-second resolution* and the work presented in the thesis are both my own, and have been generated by me as the result of my own original research. I confirm that:

- this work was done wholly or mainly while in candidature for a research degree at this University;
- where any part of this thesis has previously been submitted for a degree or any other qualification at this University or any other institution, this has been clearly stated;
- where I have consulted the published work of others, this is always clearly attributed;
- where I have quoted from the work of others, the source is always given. With the exception of such quotations, this thesis is entirely my own work;
- I have acknowledged all main sources of help;
- where the thesis is based on work done by myself jointly with others, I have made clear exactly what was done by others and what I have contributed myself;
- parts of this work have been published as: (Tuttle et al., 2014)

Signed:.....

Date:.....

Acknowledgements

There are many people who I would like to recognise for their assistance in the work that I have done. The main thanks must to go to my supervisor, Betty Lanchester. She is a true expert in the field of auroral physics, some of which has successfully rubbed off on me. She has provided me with so much support and encouragement to complete my thesis over the many years that I have been working on it.

Many of the foundations of the modelling techniques used in the works presented here originate from my colleague and frequent collaborator Bjorn Gustavsson. During our time working together at Southampton, Bjorn has shared much of his knowledge and technical know-how with me.

At the beginning of my PhD studies my fellow students and office-mates, Dan Whiter and Brendan Goodbody, were ever-friendly and always willing to share their knowledge of auroral physics and their expertise with the many complex instruments and computer programs that we use as part of the research that we do.

I have shared not only our office in Southampton, but also many exciting and adventurous fieldwork campaigns, with a larger number of colleagues who I have got to know quite well over the years, so thank you Hanna, John, Olli, Nada and Nicola.

Finally, I'd like to thank all my family and friends, both past and present, near and far, who have supported and encouraged me over the years. Completing this thesis would not have been possible without you!

Chapter 1

Introduction

At the Earth, the aurora borealis and aurora australis, or northern and southern lights, are fantastic displays of light that are visible in the night sky at high latitudes. Early theories that attempted to explain the cause of the aurora were heavily grounded in superstition. Many scientific advances were needed, such as electromagnetic theory and the discovery of the electron, before the theories started to converge with reality. In the space age direct measurements have confirmed that the aurorae are caused by charged particles, primarily electrons but also protons, precipitating into and interacting with the atmosphere.

Observations have shown the aurora can take a variety of forms spanning many orders of magnitude in scale and existing on timescales of hours to fractions of a second. At the largest scales are the auroral ovals which can be thousands of kilometres in size. These ovals are bands encircling each of the poles where aurora typically occur. Within the ovals are arc systems that can measure hundreds of kilometres in width. These arc systems are comprised of a number of individual auroral arcs each of which can be tens of kilometres in width. It is at the scale of arc systems or individual arcs that auroral observers are most familiar with the aurora. However, structuring of aurora can occur on much smaller scales than an individual auroral arc. With the advance of imaging technology and the development of single photon observation, structuring and dynamics of the aurora at spatial and temporal scales as fine as tens of metres and tens of milliseconds have been revealed.

While the auroral width spectrum has been well studied (Maggs and Davis, 1968; Borovsky et al., 1991; Knudsen et al., 2001; Partamies et al., 2010), there are still open questions as to the formation mechanisms for fine scale features, which have widths of hundreds of metres or less. Localised and dynamic mechanisms, such as near-Earth reconnection or Alfvén waves, have been suggested. However the electrodynamics that link the source of aurora in the magnetosphere with the effects measured and observed in

the upper atmosphere are not well-understood. There is therefore a need to apply measurements at the finest resolutions, both spatial and temporal, to the theories of auroral arc formation in order to determine where the source of the structuring is, and how the energy is transferred. Of particular interest are measurements of arc-associated electric fields at temporal resolutions comparable to the observed optical dynamics of fine scale aurora, which are of the order of fractions of a second. Presently available instrumentation, such as ground-based radars and rocket or satellite based-measurements, is not capable of making such measurements at the spatial and temporal resolutions necessary, and new methods are needed. Chapter 2 describes the relevant theories that explain the aurora, as well as describing existing methods which have been used to measure and quantify auroral particle precipitation and electric fields at various scales.

As the subject of this thesis is the highly structured and dynamic fine scale aurora, observations at sufficiently high spatial and temporal resolutions are required. The observations presented in this thesis are obtained from two main sources. The optical observations presented in chapters 5, 6, and 7 are obtained from the Auroral Structure and Kinetics instrument (ASK), which is a state-of-the-art multi-monochromatic auroral imager capable of making observations at very high spatial (10s of metres) and temporal (up to 40 Hz) resolutions. The ASK instrument was originally designed to measure fine scale electric fields close to aurora using the long-lived metastable oxygen ion as a tracer. The main motivation of the work presented here, in particular for the work in chapter 7, is showing that this unique method is feasible. Radar observations from the European Incoherent Scatter (EISCAT) radar facility in Norway are used in chapter 5 to investigate the energy spectrum of the particle precipitation which produces the aurora. Radar observations from the Super Dual Auroral Radar Network (SuperDARN) are used in chapter 7 to validate the recovered electric fields. These observation platforms are discussed in greater detail in chapter 3.

A number of modelling techniques are used to complement and interpret these observations. These techniques allow the energy spectrum of precipitating particles to be determined from radar observations and allow the ionospheric response to the aforementioned particle precipitation to be modelled using an atmospheric ion-chemistry model. Modelling of the auroral emissions observed by the ASK instrument is of particular interest. Further discussion and detail on these techniques are presented in chapter 4.

The original work presented in this thesis is contained in chapters 5, 6 and 7. Chapters 5 and 6 explore new ways in which the particle precipitation, and resulting auroral emissions, can be modelled using ground-based instrumentation at sub-kilometre resolution in a volume that has a size of a few 10s of km perpendicular to the magnetic field. Such techniques are required to allow the ionospheric electric fields to be extracted, using the combination of observations and modelling presented in chapter 7, from optical observations of auroral emission from a long-lived ion observed by the ASK instrument. In particular, chapter 5 explores a novel method of combining radar and

optical observations to model the auroral electron energy spectrum and the resulting emissions and is applied to an auroral event exhibiting fine scale structure that occurred on 12 December 2006. Chapter 6 examines a second method for estimating the auroral electron energy spectrum and the resulting emissions, this time using optical data only, and is applied to an auroral event that occurred on 9 November 2006, when no radar data were available. Such techniques can be applied to, or adapted for, most fine scale auroral imagers.

Chapter 7 presents a novel method for extracting ionospheric electric fields from optical observations of auroral emissions from a long-lived ion. The modelling techniques presented in chapters 5 and 6 are used to model the auroral production of this ion in 3-D. The events in both chapters are analysed using flow parameterisation schemes that model the background ionospheric flow and the arc-associated flows. An optimisation is run on this 3-D distribution of ions to extract the ion velocity, from which the ionospheric electric fields are found. The recovered velocities are then interpreted in the context of the radar observations from SuperDARN, which suggest a successful extraction of the plasma velocities. Finally, conclusions drawn from the techniques and results presented in chapters 5, 6 and 7 are presented in chapter 8.

Chapter 2

Theory

The ultimate source of the aurora is the Sun which is continuously emitting charged particles. These charged particles, which are mainly protons and electrons but also nuclei of lighter elements such as helium, form a fully ionised plasma which flows outward into the heliosphere from the Sun, forming the solar wind. The high conductivity of the solar wind plasma results in the magnetic field of the Sun being frozen into the plasma. As the plasma flows away from the Sun, the magnetic field is carried with it. This magnetic field, which fills the heliosphere, is called the interplanetary magnetic field, or IMF. The Earth's magnetic field, hereafter referred to as the geomagnetic field, forms an obstacle to the solar wind, carving out a bubble surrounding the Earth in which the effects of the geomagnetic field are dominant over that of the IMF; this bubble is known as the magnetosphere. The structure of the magnetosphere and the orientation of the geomagnetic field within it are shown in figure 2.1. In this figure, the Sun (not shown) is far to the left, and the solar wind flows from left to right.

A useful co-ordinate system to introduce here is the Geocentric Solar Ecliptic, or GSE, system. In GSE co-ordinates the x-axis is directed from the centre of the Earth towards the Sun and the z-axis is directed perpendicular to the plane of the Earth's orbit around the Sun, with the positive z-direction pointing northward. Using figure 2.1 as a reference, the positive x-direction points to the left, the positive z-direction points up the page, and the positive y-direction points out of the page. Where components of the IMF are discussed, the subscript on the component indicates the direction of that component.

Plasma can be transferred into and out of the magnetosphere through a process called magnetic reconnection. This process occurs predominantly when magnetic fields of opposing directions interact, and reconfigure their magnetic topologies to reach a lower magnetic energy state. At the sunward edge of the magnetopause the direction of the geomagnetic field is directed northwards, or in the positive B_z direction. Therefore for reconnection to occur at the magnetopause, the IMF B_z component must be negative, or point southward. During the reconnection process, energy is transferred from the

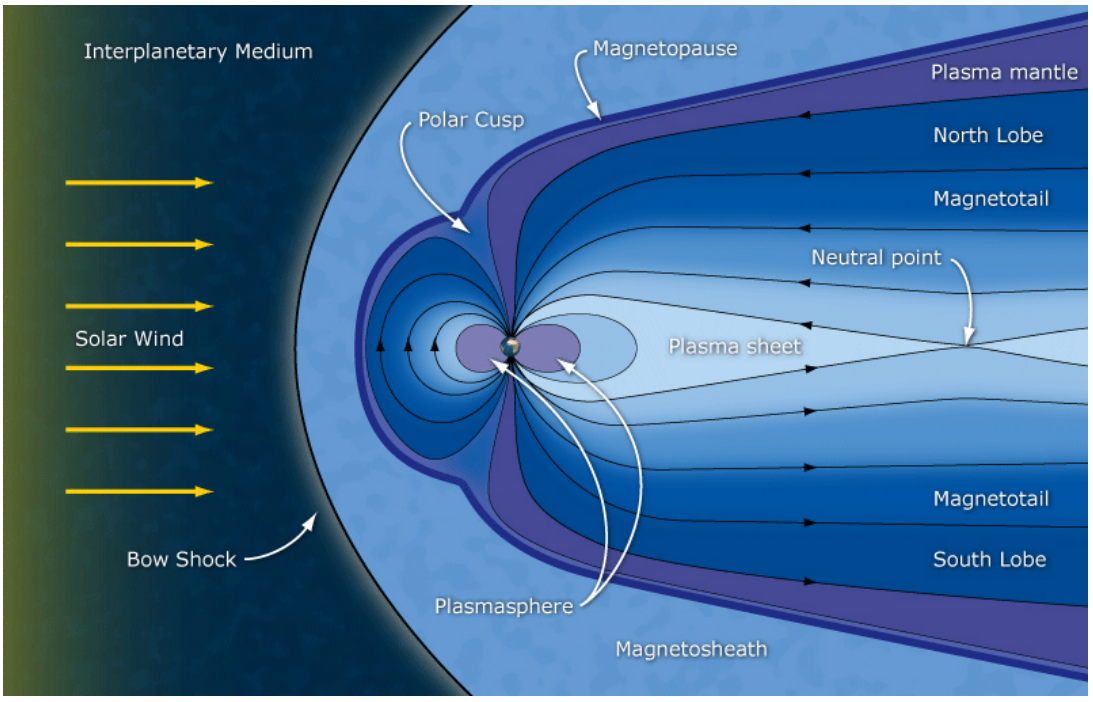

Figure 2.1: Diagram of the Earth's Magnetosphere showing the major regions and the structure and direction of the geomagnetic field (black arrows). Figure originally produced by the European Space Agency (ESA).

magnetic field to the particles of the plasma, accelerating the particles along the field lines. If the particles are accelerated Earthward, and the energies of these accelerated particles are great enough such that they do not get trapped by the magnetic mirroring effect, caused by to the gradient in the magnetic field strength as the particles move closer to the Earth, the particles will precipitate into the Earth's atmosphere on the day-side. Observations of the precipitating electrons have revealed low or 'soft' precipitation energies, which are of the order of hundreds of eV.

Reconnection can also happen at the location labelled 'neutral point' in figure 2.1, which lies anti-sunward from the Earth in the magnetotail. Through a process called the Dungey cycle the magnetic field lines convect from the day-side, over the poles and into the night-side, towards the neutral point. At the 'neutral point', the oppositely directed magnetic fields and are in a high magnetic energy configuration. Through reconnection the magnetic field is again reconfigured, with the two field lines to the left of the arrow that indicates the position of the neutral point forming a single field line, and the two field lines to the right of this arrow forming the second field line. This process again transfers energy from the magnetic field to the particles in the plasma, accelerating the plasma either earthward or anti-Earthward depending upon which new magnetic field line the plasma is on. The plasma that is accelerated Earthward precipitates into the atmosphere on the night-side of the Earth. Observations of the energies of precipitating electrons on the night-side have revealed higher, or 'harder', energies of the order of a few, or a few 10s of, keV.

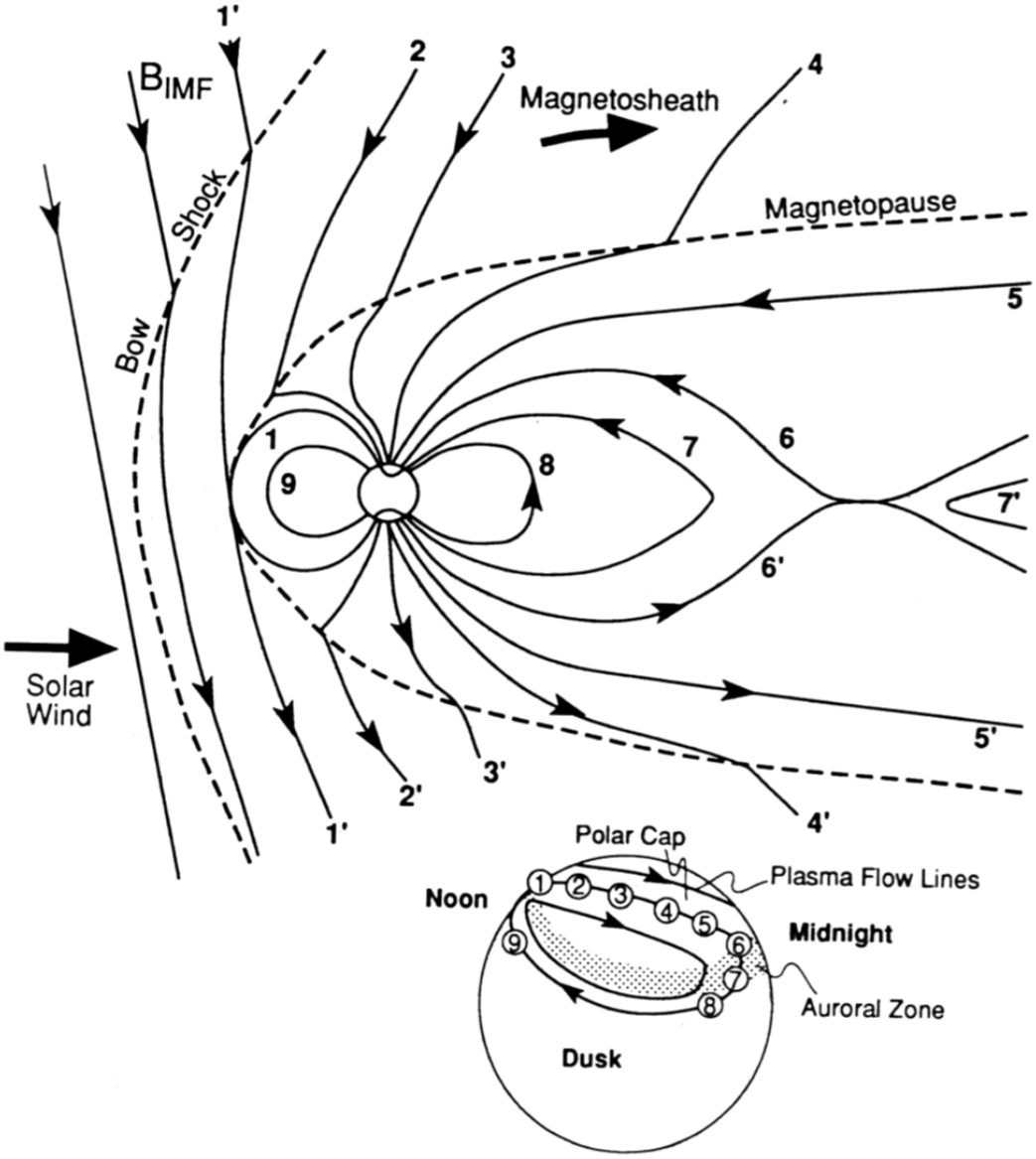

Figure 2.2: Top: Convection of magnetospheric plasma driven by magnetic reconnection. The arrowed lines 1-1' through 9 indicate the motion of an individual magnetic field line. Bottom: Convection of the ionospheric footpoint of the magnetic field lines numbered 1 through 9 in the top diagram. Figure reproduced from Kivelson and Russell (1995).

It is reconnection, both at the magnetopause and in the tail, that initially energises the electrons that produce the day- and night-side aurora. Other, smaller scale, processes further accelerate and structure the particles as they travel along the magnetic field towards the Earth. Such processes are discussed in section 2.3.

At the Earth, magnetic reconnection occurs at the magnetopause and in the magnetotail as part of a large-scale process which convects magnetic field lines around and through the magnetosphere. This process is called the Dungey cycle (Dungey, 1961), and is

illustrated in figure 2.2. This figure shows a cross-section through the magnetosphere at a time of southward, or negative B_z, IMF. Reconnection at the magnetopause cause the IMF field line labelled 1 to be broken, opening the geomagnetic field to the IMF in the solar wind and allowing solar wind particles into the magnetosphere. The flow of the solar wind past the Earth convects the open field line 1-1' over the polar cap and into the magnetotail, with subsequent positions indicated by the field lines labelled 2-2', 3-3', 4-4', and 5-5'. Magnetic pressure, exerted by convecting field lines from subsequent reconnection events, compresses the field and the plasma in the tail until reconnection occurs along the field line labelled 6-6'. This once again closes the geomagnetic field, disconnecting it from the IMF in the solar wind. This closed field line then convects from the night-side to the day-side, with interim positions indicated by the field lines labelled 7, 8, and 9. The schematic at the bottom of figure 2.2 shows the motion of the atmospheric footpoints of the field lines on the duskward side of the polar cap, with the numbers corresponding to the numbered field lines in the upper part of the figure. A second flow also convects field lines from the night-side to the day-side along the dawn-ward side of the polar cap. These convective flows in the upper atmosphere will be re-examined and further discussed after the atmosphere and ionosphere have been introduced and discussed.

At high altitudes, typically above 70 km, an ionised layer called the ionosphere is formed in the Earth's atmosphere through photo-ionisation of atmospheric neutrals by solar radiation and by ionising collisions between precipitating particles and atmospheric neutrals. The portion of the ionosphere at high latitude, where the geomagnetic field dips into the atmosphere and particle precipitation occurs, is called the auroral ionosphere. The middle and right-most plots in figure 2.3 show variation of the ionospheric ion, and atmospheric neutral densities with altitude. It should be noted that the ionospheric electron density will be equal to the ionospheric ion density because the atmosphere remains electrically neutral overall. These plots show the degree of ionisation in the ionosphere at lower altitudes is very low, and that the degree of ionisation changes with altitude. At high altitudes the ionosphere becomes fully ionised, and merges into the magnetosphere.

The Dungey cycle implies a convection of magnetospheric plasma across the polar cap, setting up an electric field ($\mathbf{E}$) which is given by:

$$\mathbf{E} = -\mathbf{v} \times \mathbf{B} \tag{2.1}$$

where $\mathbf{B}$ is the geomagnetic field vector and $\mathbf{v}$ is the convection velocity of the plasma. Figure 2.4 shows a view of the twin-cell polar cap convection pattern, and associated electric fields, under southward IMF conditions with different directions to the B_y component. The relative size of each convection cell is therefore dependent on the IMF B_y component.

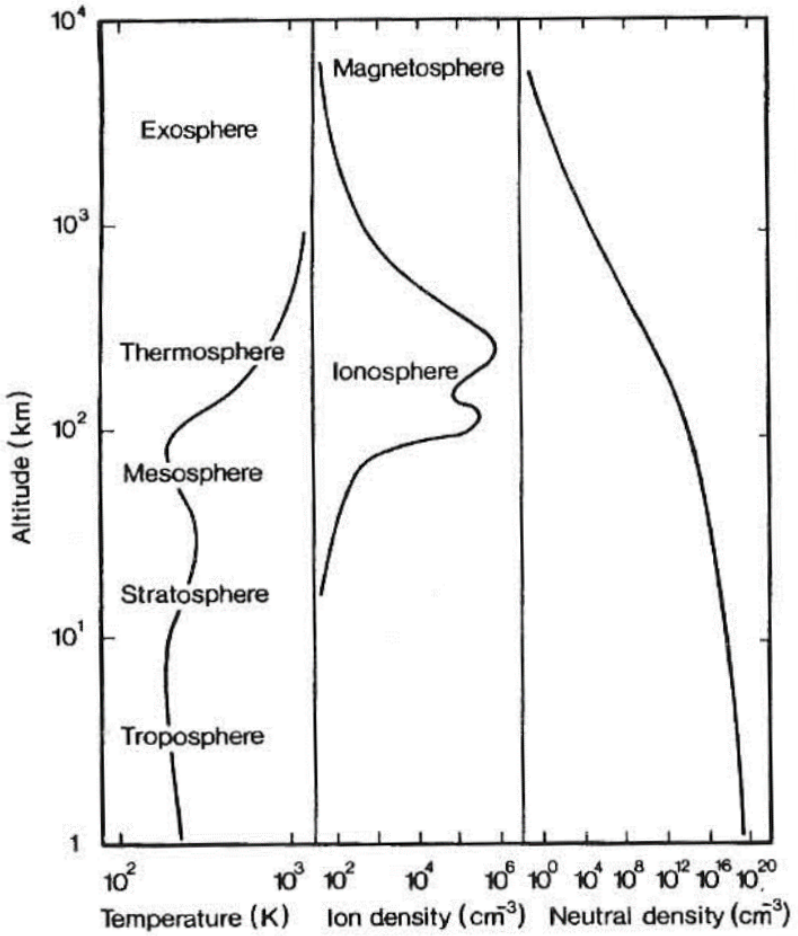

Figure 2.3: Plot showing the variation with altitude of the: neutral temperature (left), ionospheric ion density (middle), and neutral density (right). Figure reproduced from Rees (1989).

These electric field and convections patterns are mapped down the ionosphere by a system of currents which loop through the ionosphere and magnetosphere. Figure 2.5 shows the configuration of this current system as if looking down on the polar cap from above. The currents labelled 'region 1' and 'region 2' are the so-called Birkeland currents which are aligned parallel to the geomagnetic field. These currents represent the precipitation of plasma into the ionosphere, and the return of plasma from the ionosphere to the magnetosphere. Electrical currents also flow within the ionosphere. Pedersen currents flowing along the direction of the ionospheric electric field connect the region 1 and region 2 currents, and Hall currents flow in direction of the circulating ionospheric plasma. Figure 2.6 is a 3-D representation of this current system, and more clearly shows the ionospheric currents.

The relative importance of these Hall and Pedersen currents at any given altitude is determined by the ratio of the collision frequency between the convecting plasma and the neutral atmosphere, ν_{in}, to the ion gyrofrequency, Ω_i. The ion gyrofrequency represents

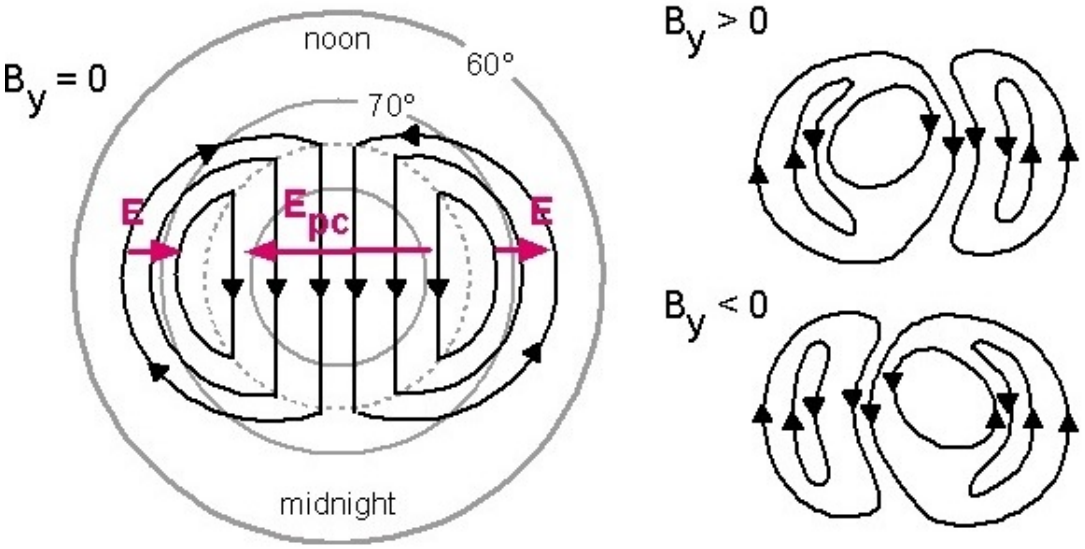

Figure 2.4: Ionospheric convection electric fields for a southward IMF, with the indicated B_y directions. Black lines indicate the direction of plasma flow and purple lines indicate the direction of the electric fields. Figure provided by Oulu university.

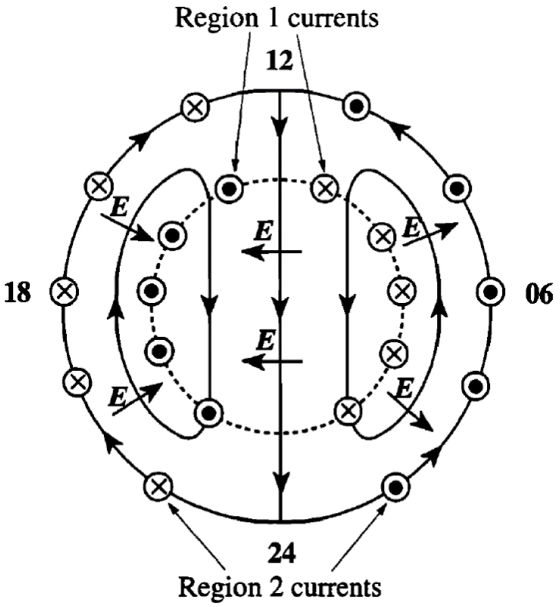

Figure 2.5: Dungey cycle flow mapped into the ionosphere. The numbers '06', '12', '18', and '24' represent the directions of dawn, noon, dusk, and midnight respectively. Short arrows indicate ionospheric electric fields and continuous arrowed lines indicate the direction of plasma flow. The dotted and crossed circles indicate the directions of electrical currents into and out of the ionosphere respectively. The dashed circle represents the boundary between open and closed magnetic field lines. This figure is a reproduction of figure 1 of Cowley (2013).

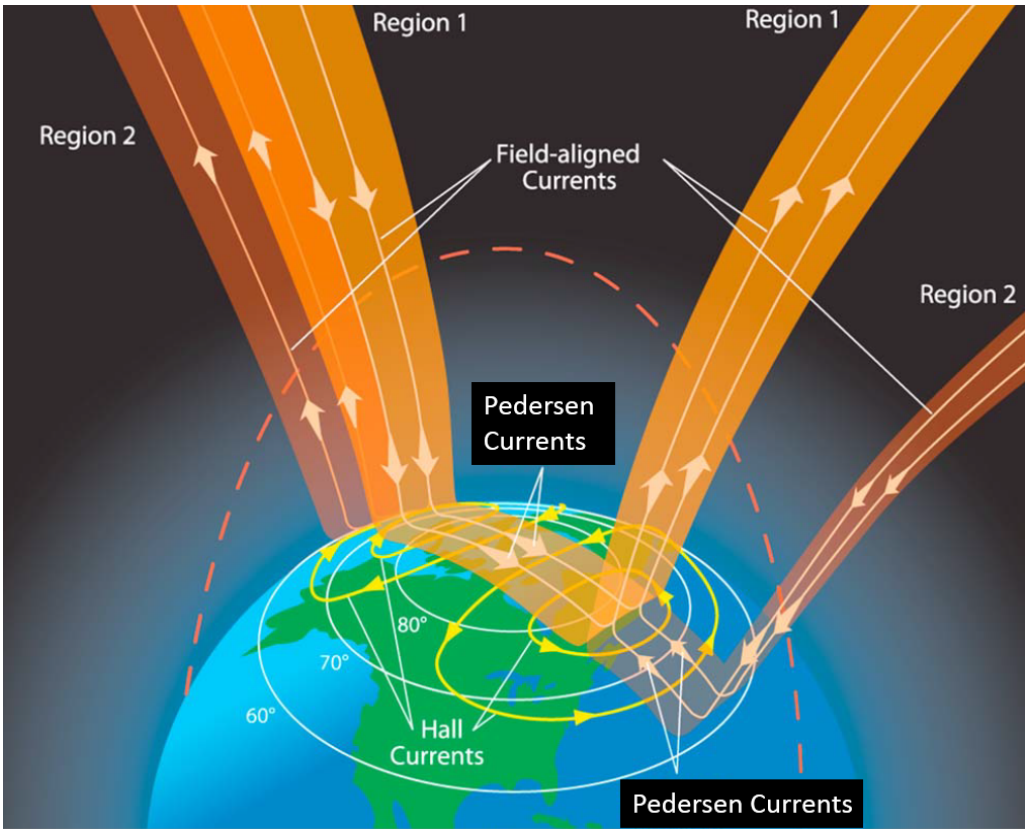

Figure 2.6: Three dimensional representation of the region 1 and region 2 field-aligned currents, or Birkeland currents, which electrically connect the ionosphere and magnetosphere. Also shown are the Hall and Pedersen currents in the ionosphere. This figure is a reproduction of figure 1 of Le et al. (2010) with annotations to correct spelling mistakes.

the frequency of ion oscillations about the geomagnetic field, and is given by:

$$\Omega_i = \frac{eB}{m_i} \tag{2.2}$$

where e is the elementary charge and m_i is the mass of the ion. Taking the neutral atmosphere as a reference, the force balance equation for the convecting ions is given by:

$$e\left(\mathbf{E} + \mathbf{v}_i \times \mathbf{B}\right) = m_i \nu_{in} \mathbf{v}_i \tag{2.3}$$

where $\mathbf{v}_i$ is the convection velocity of the ion. The ion flow velocity perpendicular to the magnetic field, $\mathbf{v}_{i,\perp}$, is then given by:

$$\mathbf{v}_{i,\perp} = \frac{1}{1 + \left(\frac{\nu_{in}}{\Omega_i}\right)^2} \left[\frac{\mathbf{E} \times \mathbf{B}}{B^2} + \left(\frac{\nu_{in}}{\Omega_i}\right) \frac{\mathbf{E}}{B}\right] \tag{2.4}$$

The ion-neutral collision frequency and ion gyrofrequency are equal at about 125 km (Richmond and Thayer, 2013). At altitudes higher than about 125 km, the rapidly

decreasing neutral density causing the ion-neutral collision frequency to fall. The ion gyrofrequency will also decrease, as the magnetic field strength decreases, but not as much as the collision frequency decreases. Therefore at altitudes greater than about 125 km, the is dominant, and the ion convection velocity perpendicular to the magnetic field can be approximated to:

$$\mathbf{v}_{i,\perp} \approx \frac{\mathbf{E} \times \mathbf{B}}{B^2} \tag{2.5}$$

This ion motion is directed perpendicular to the geomagnetic and electric fields as given by $\mathbf{E}\times\mathbf{B}$. The plasma flows and electric fields calculated later in chapter 7 are interpreted as measurements of this large scale plasma motion at altitudes higher than 125 km.

At altitudes lower than about 125 km, the ion-neutral collision frequency is dominant, and the convection velocity can be approximated to:

$$\mathbf{v}_{i,\perp} \approx \frac{\Omega_i}{\nu_{in}} \frac{\mathbf{E}}{B} \tag{2.6}$$

These ion motions are parallel to the electric field.A similar analysis applied to the electrons yield an electron drift velocity perpendicular to the magnetic field, $\mathbf{v}_{e,\perp}$, given by:

$$\mathbf{v}_e \approx \frac{\mathbf{E} \times \mathbf{B}}{B^2} \tag{2.7}$$

The behaviour for the electrons results from the significantly increased electron gryoradius.

The net current density perpendicular to the magnetic field, $\mathbf{j}_\perp$ due to the relative motions of electrons and ions is given by:

$$\mathbf{j}_\perp = ne\left(\mathbf{v}_{i,\perp} - \mathbf{v}_{e,\perp}\right) \tag{2.8}$$

where n is the number density of ions and electrons and all ion species are assumed to convect in the same way. Substituting the expressions for the ion and electron velocities from equations 2.4 and 2.7 respectively into equation 2.8, yields:

$$\mathbf{j}_\perp = \frac{ne\left(\frac{\nu_{in}}{\Omega_i}\right)}{\left(1+\left(\frac{\nu_{in}}{\Omega_i}\right)^2\right)}\left[\frac{\mathbf{E}}{B} - \left(\frac{\nu_{in}}{\Omega_i}\right)\frac{\mathbf{E}\times\mathbf{B}}{B^2}\right] \tag{2.9}$$

The first term represents the Pedersen current density, which flows aligned to the magnetic field and is dominant above 125 km. Here, the contributions to the current density from the $\mathbf{E}\times\mathbf{B}$ drifts of the ions and electrons cancel, leaving only a contribution due to the mobility of the ions in the direction of the electric field. The second term represents the Hall current density, which flows in the opposite direction to the $\mathbf{E}\times\mathbf{B}$ drift and is dominant below 125 km. Here contributions from ion motions are suppressed, by collisions with the denser neutral atmosphere at lower altitudes, leaving only a contribution

due from the $\mathbf{E} \times \mathbf{B}$ drift of the electrons.

2.1 The auroral electron energy spectrum

Most aurora is produced by electrons of varying energies precipitating into, and interacting with, the neutral atmosphere. Precipitating protons can also produce auroral emissions, however this proton aurora is less structured and is therefore not useful for the investigation of fine scale auroral structures. Observed energy spectra of these precipitating electrons exhibits variance both in energy and spectra shape, and this variance can be used to infer the acceleration processes responsible for producing the observed energy distributions of electrons.

When referring to the energy and flux of the electron energy spectrum, care must be taken as to exactly what 'energy' and 'flux' refer to. The total electron flux refers to the total number of supra-thermal precipitating electrons per unit area per unit time, and the total energy flux refers to the total energy carried by the supra-thermal electrons per unit area per unit time. Figure 2.7 shows the differential electron flux for purely Gaussian (red) and Maxwellian (blue) energy spectra which both have a total energy flux 1 mW m^{-2}. Both energy spectra have the same peak energy, 3 keV, where the peak energy is the energy at which the differential electron flux, in units of m^{-2} s^{-1} eV^{-1}, is the largest. The Gaussian spectrum has a half-width of 500 eV. The average energy of the precipitating electrons is given by the ratio of the total energy flux to the total electron flux. The total electron fluxes for each spectrum are found by integrating the area under the curves and, here, the total energy fluxes are 1 mW m^{-2}. The Gaussian spectra carries twice as many electrons as the Maxwellian spectrum for the same energy flux, which yields the result that the average energy for the Maxwellian spectrum (6 keV) is twice the average energy of the Gaussian spectrum (3 keV).

However the energy flux of measured electron spectra is not known a priori, and must instead be calculated. Figure 2.8 shows the differential energy flux, measured in units of eV m^{-2} s^{-1} eV^{-1}, for the two spectra shown in figure 2.7. These energy flux spectra show that the two spectra have peak energy fluxes at different energies, which has implications for the altitude of energy deposition in the atmosphere. The energies at which the energy flux is the greatest correspond to the average energies for the purely Gaussian or Maxwellian spectra. In the plots showing the pure spectra, a low energy tail has not been added. If a low-energy tail were included the total electron flux, for a fixed total energy flux of 1 mW m^{-2}, would be greatly increased, as many more electrons of lower energy are required to replace each electron of a higher energy, and the average energy would be decreased. The peak energy would be unaffected as the peak energy specifically refers to the energy of high energy component of the spectrum, that is the Maxwellian or Gaussian.

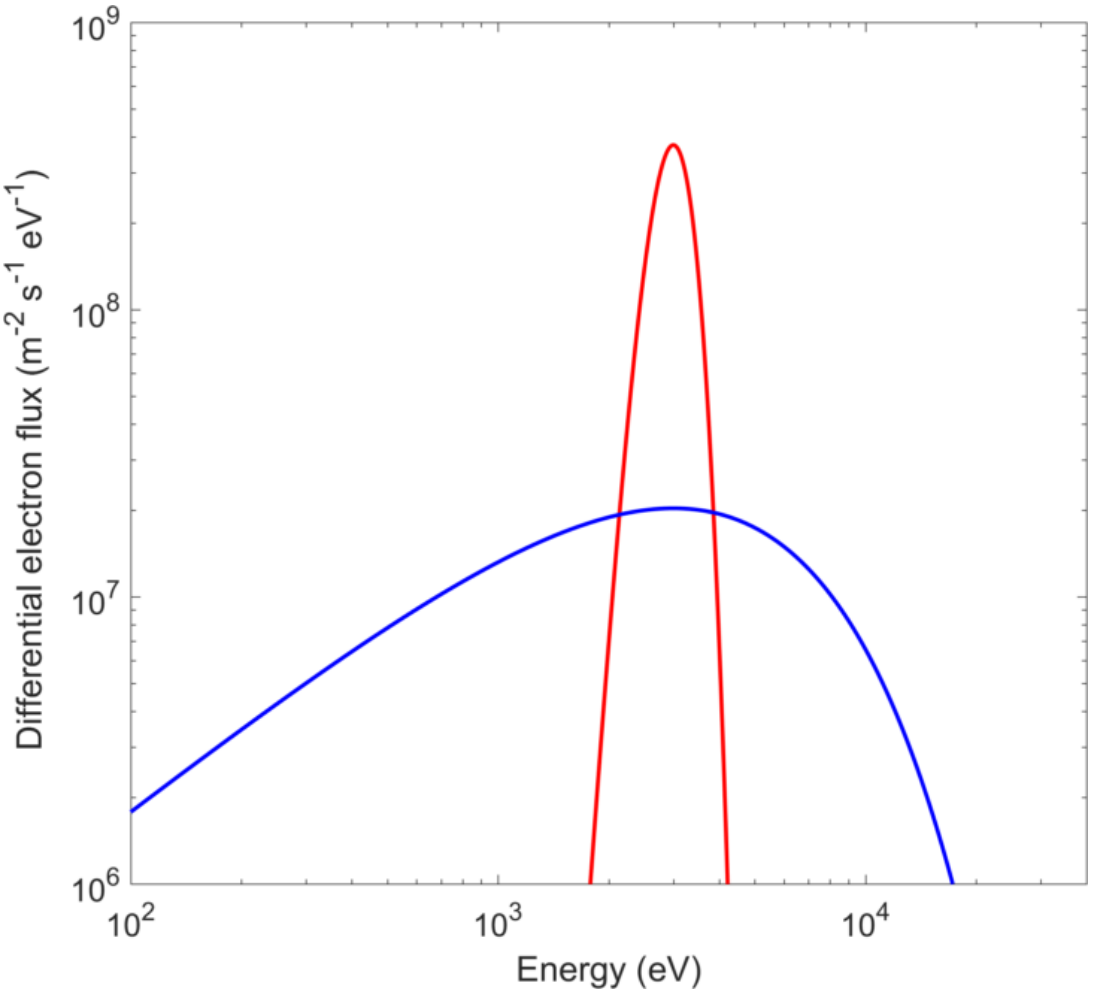

Figure 2.7: Simulated differential electron fluxes which exhibit pure Maxwellian (blue) or Gaussian (red) spectral shapes. Both spectra carry a total energy flux of 1 mW m^{-2}.

2.1.1 In-situ measurements

Direct observation of the energy spectra associated with auroral arcs and features is only possible by flying instrumentation through or above the observed auroral forms. The first such direct observations by McIlwain (1960) showed rapid variations in the total energy flux of the precipitation as the rocket passed through an auroral arc, suggesting that the observed almost-monoenergetic flux of electrons at about 6 keV was the main contributor (>75%) to the observed auroral brightness. Subsequent rocket-borne observations of further auroral arcs also show the presence of near-monoenergetic fluxes of electrons at keV energies (Albert, 1967; Evans, 1968). Such near-monoenergetic distributions are interpreted as being produced by an electrostatic acceleration process, such as a field-aligned electric potential drop.

However, these early experiments were unable to suitably measure the sub-keV component of the precipitating electrons. Measurements of energy spectrum at sub-keV

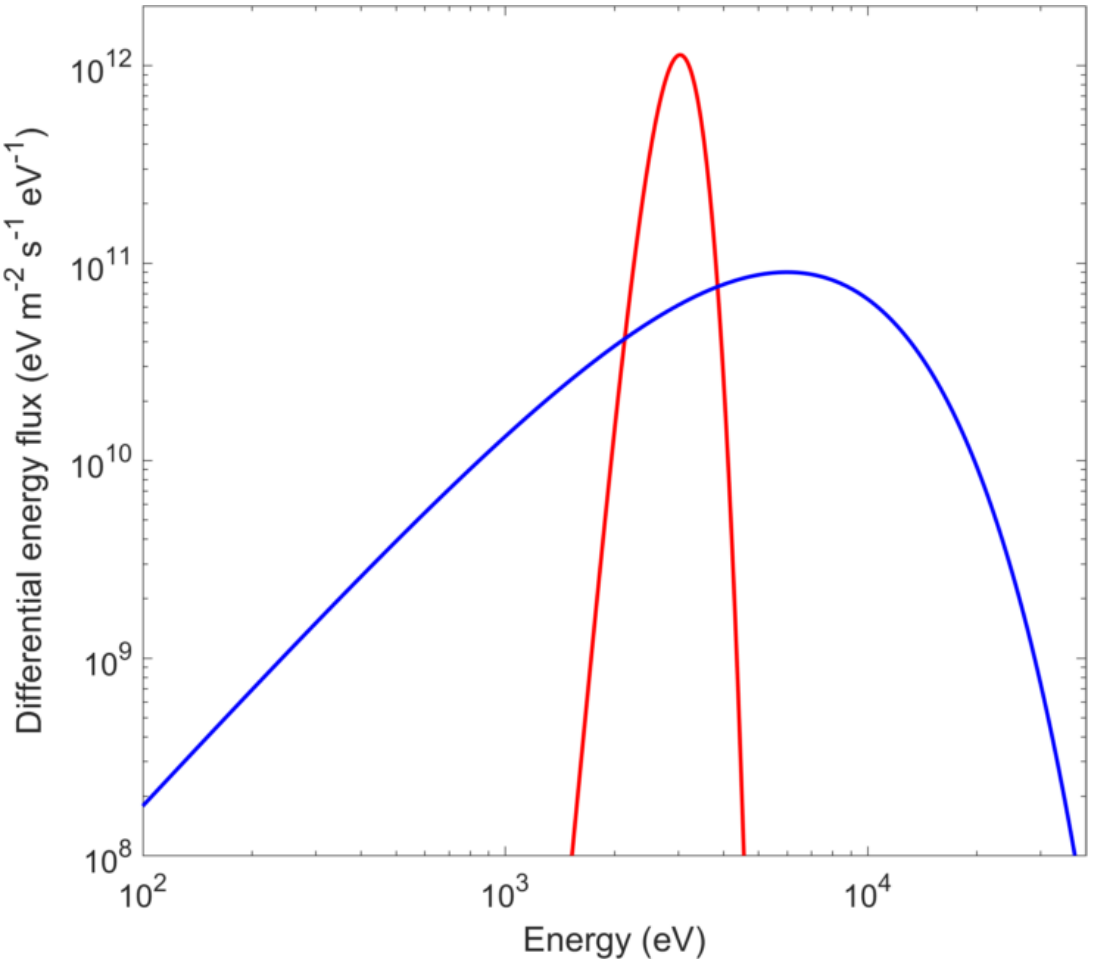

Figure 2.8: Simulated differential energy fluxes for the spectra presented in figure 2.7.

energies were first made by Westerlund (1969), extending the energy range of the measurements to as low as 45 eV. These measurements revealed significant downward fluxes of electrons at sub-keV energies, with the differential number flux of the energy spectrum related to the precipitation energy through a power-law with a negative exponent. A near-monoenergetic peak at keV energies was observed to be superimposed onto the power-law distribution. The cause of this power-law distribution was interpreted by Evans (1974) to be due to back-scattered electrons reflecting off the potential structure which produces the keV near-monoenergetic distribution. These back-scattered electrons have a lower energy than the precipitating near-monoenergetic electrons and therefore do not possess enough energy to overcome the potential structure.

The energy spectra of precipitating electrons have also been found to exhibit Maxwellian distributions. Frank and Ackerson (1971) used observations from the INJUN-5 satellite, which was in a low, almost-polar orbit, to extensively study particle precipitation into the atmosphere, finding the electron spectra to be typified by a power law distribution, with an exponent of between -2.5 and -1.5, at low energies (<a few hundred eV) and a Maxwellian distribution with a peak differential number flux at keV energies. Frank

and Ackerson (1971) also noted that the near-monoenergetic distributions presented in previous observations could not be reasonably approximated by Maxwellian spectral shapes.

Fontheim et al. (1982) performed a statistical analysis on electron energy spectra obtained from the Atmospheric Explorer-D (AE-D) satellite, modelling each observed energy spectrum as having contributions from power-law, Gaussian and Maxwellian distributions. Their results from the analysis of the sub-keV power-law component provide further support to the idea that this component is due to backscattered primary electrons and secondary electrons, which are produced during collisions between the primary electrons and the neutral atmosphere. Fontheim et al. (1982) also noted that not all observed spectra contained contributions from all three distributions, suggesting that distinct processes were responsible for the contribution of each component to the resulting measured energy spectrum.

Rocket and satellite based observations of auroral electron energy spectra can also provide information about the spatial structuring of the precipitation. Such spatial structuring is obtained by examining sequential observations of the energy spectrum as the observing instrument traverses the auroral arc. The high speeds of the rocket or satellite across the arc, typically of the order of km s^{-1}, allow differences in sequential observations to be interpreted as spatial variations across the arc. One commonly observed feature of such observations is the so-called inverted-V distribution. Figure 2.9, which is taken from McFadden et al. (1990), shows such a distribution obtained from rocket-borne observations. The inverted-V is characterised by a rise in the peak energy of the precipitation, which is the energy at which the differential number flux is largest, as the detector moves from the edge of the auroral arc to the centre and a subsequent decrease in peak energy as the detector moves from the centre of the arc to the other edge. The inverted-V feature is thought to be due to the spatial structuring of an electrostatic potential, which is discussed later in section 2.3. The event analysed by McFadden et al. (1990) is also notable as the observed auroral arc was somewhat narrow, with a width of about 10 km, the investigation was conducted using two rockets launched in rapid succession, and the complex structuring of the observed aurora highlighted the need for higher resolution, multi-spacecraft measurements.

However, as in-situ measurements are often thought of as spatial, rather than temporal, variations, such observations are not suitable for modelling or analysing the structuring and dynamics of fine scale aurora. Ground-based techniques have been developed to better study the auroral electron energy spectrum at finer scales. Existing techniques use radar or optical observations of the aurora to infer the energy spectrum of the electron precipitation, or characteristics of the spectrum, such as characteristic energy or total energy flux. Modelling the effect of electron precipitation into the ionosphere is a necessary step of such techniques because the observations used to infer the energy spectrum or its characteristics are a direct consequence of the electron precipitation.

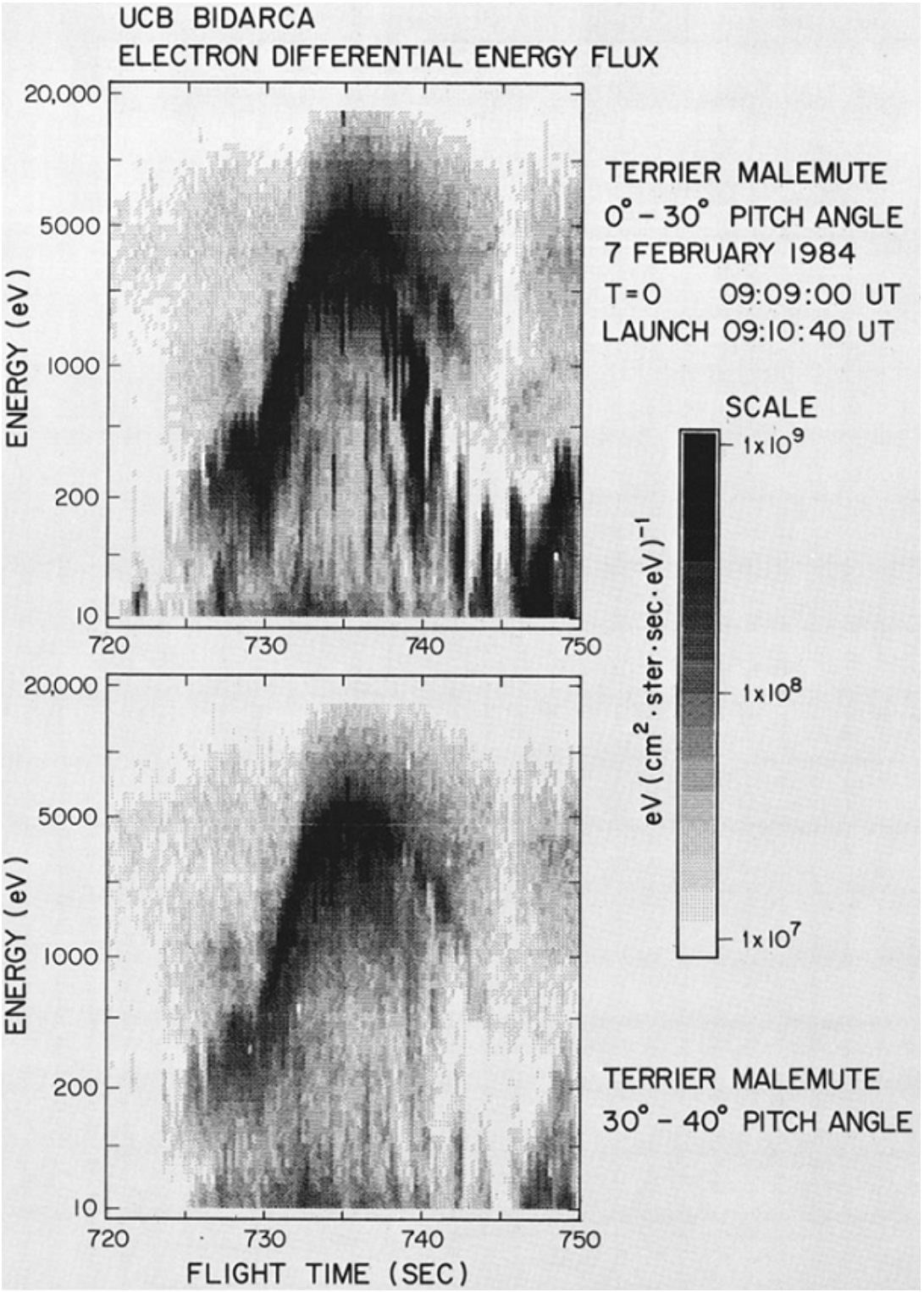

Figure 2.9: Measured electron energy spectra which exhibit an inverted-V spatial distribution. Reproduced from figure 5 of McFadden et al. (1990).

Forward modelling of the brightnesses or electron densities using an assumed electron energy spectrum allows the observations to be compared to the modelled results, and the energy spectrum, or characteristics of, to be inferred.

2.1.2 Optical Methods

Emission brightness ratios and tomographic methods are two well-established methods that are commonly used to estimate the characteristics of the electron precipitation which causes the aurora. Tomographic methods (Gustavsson, 1998; Partamies et al., 2003; Simon-Wedlund et al., 2013) are well suited to situations where multiple, simultaneous observations of aurora from separate locations are available. However, due to the relatively wide fields of view used in such observations, tomographic methods typically result in spatially coarse estimates of the precipitation characteristics. Such estimates, typically at resolutions of greater than 1 kilometre, are unsuitable to analyse the characteristics of fine scale aurora.

Emissions brightness ratios have often been used to study the fine scale characteristics of auroral precipitation. Early works which utilised ratios of emissions used ratios between the brightest auroral emissions, the red (630.0 nm) and green (577.7 nm) lines from atomic oxygen and the blue band emission (427.8 nm) from ionized molecular nitrogen (Rees and Luckey, 1974). However, the red and green lines are not suitable for observing aurora at fine spatial or temporal resolutions due to the long lifetimes of the emitting excited states, which are 110 s and 0.75 s respectively.

A preference for observations of emissions which are prompt, that is they are instantaneous or near-enough instantaneous, exists because observations of prompt emission remove additional complexity in the modelling of the emission, which must account for motion due to neutral winds or electric fields if the emission is from a long-lived state. Observations of prompt emissions also allow estimates of the characteristics of the precipitation to be determine at higher temporal resolutions. Advances in imaging technology have permitted the imaging of emissions which have lower brightnesses, but that are prompt, to be used in emission ratio techniques (Meier et al., 1989; Strickland et al., 1989; Hecht et al., 1989, 1999; Hecht et al., 2006). Further technological advances have permitted observations at the single-photon level. Such observations were used by Lanchester et al. (2009), using emissions at 673.0 nm and 777.4 nm, and by Dahlgren et al. (2011), using emissions at 562.0 nm and 777.4 nm, to estimate the energy and energy flux of the electron precipitation using a combination of observations and ionospheric modelling. These works highlight the applicability of combining auroral and ionospheric modelling with auroral observations to determine the characteristics of auroral precipitation along the magnetic zenith.

Tuttle et al. (2014) examined the fusion of radar and optical data at sub-kilometre and sub-second resolution. They showed that estimates of the electron energy spectra in the magnetic zenith, obtained by inversion of radar estimates of electron density, could be characterized by optical estimates of the energy and flux of the precipitation, also in the zenith. Using this characterisation, they extrapolated energy spectra to regions surrounding the magnetic zenith and found agreement between modelled and observed images of the emission brightness at multiple wavelengths, noting that an underestimate of brightness in the modelled images was a result of the arc not filling the radar field of view. These results are one component of the new work presented in this thesis and are fully described and discussed in chapter 5.

Methods using brightness ratios are usually applied only to observations in the magnetic zenith in order to avoid perspective effects. The electrons which cause the aurora precipitate along magnetic field lines, producing auroral emission extended parallel to the field. However, optical observations from auroral imagers are often made from a single location, with lines of sight that intersect the magnetic field. Perspective effects arise when the aurora is observed outside of the local magnetic zenith, causing a component of the altitude extent of the emissions to be visible. This component can be significant, due to the large vertical-to-horizontal aspect ratios that are often present in the aurora (up to a few hundred); it complicates analysis and interpretation of auroral observations within a few degrees of the zenith and prevents accurate interpretation at larger zenith angles (Semeter, 2012). The work presented in chapter 6 is a first attempt at correcting for perspective effects when observing outside of the magnetic zenith.

2.1.3 Radar methods

Radar observations are also used to estimate the auroral electron energy spectrum, or characteristics thereof. One major limitation of such observations is that the observations must be aligned with the geomagnetic field. Such observations are said to be made in the magnetic zenith. The electron precipitation which causes the aurora is confined to a single field line, which means that the energy spectra of precipitation along neighbouring field lines may be vastly different. Consequently, any radar observation across multiple field lines would result in partial observations of potentially, many energy spectra. Such observations would be unsuitable for analysis.

Radar observations of electron density are used to estimate the precipitation. One such method, the "flux-first" method (Palmer, 1995; Lanchester et al., 1996, 1997, 1998, 2001) uses a library of ionisation rate profiles, from spectra of a given energy, flux and shape, to determine the ionisation profile, and hence energy spectrum, that causes the observed electron densities. Other methods, such as inversion of radar data have also been used (Semeter and Kamalabadi, 2005; Dahlgren et al., 2011). However, due to the

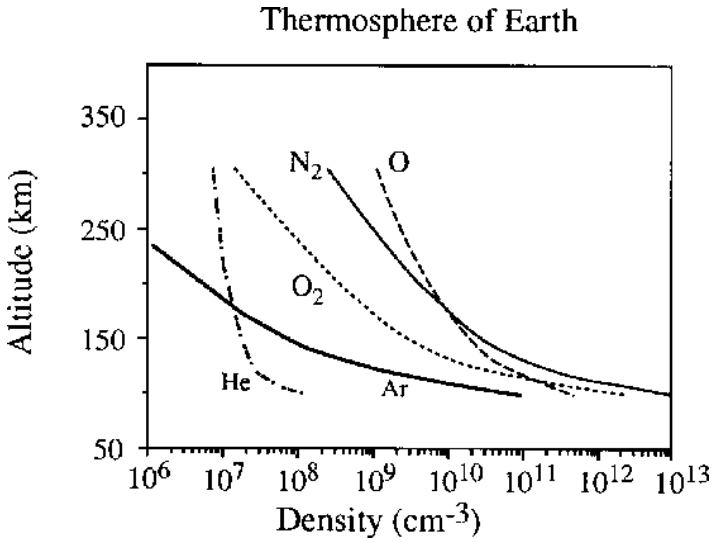

Figure 2.10: Neutral atmosphere densities for the main constituents of the Earth's atmosphere at auroral altitudes. Figure reproduced from Cravens (1997).

requirement to observe in the magnetic zenith, any radar method is limited to measuring only what passes through the field of view of the radar.

2.2 Auroral Emissions

As the electrons precipitate into the atmosphere they collide with the atoms and molecules in the atmosphere, transferring energy and exciting or ionising the atoms and molecules. Figure 2.10 shows the variation in altitude of the densities of the main constituents of Earth's atmosphere. The densities of molecular nitrogen and both atomic and molecular oxygen are dominant at altitudes of auroral interest. This dominance causes insignificant fractions of energy of the auroral precipitation to be deposited into the other minor atmospheric species. For the purposes of analysis of auroral emissions, the atmosphere can therefore be thought of as being composed only of molecular nitrogen, molecular oxygen, and atomic oxygen.

The cross-section for interaction between a precipitating electron and an atmospheric particle is energy dependent. Figures 2.11, 2.12 and 2.13 show the total cross-sections for excitation and ionisation of molecular nitrogen, molecular oxygen, and atomic oxygen respectively by precipitating electrons. These cross-sections all have peaks in the eV or tens of eV range. The cross-sections at typical energies for auroral precipitation, which are keV or tens of keV, are at least an order of magnitude smaller than at eV or tens of eV energies, making the precipitating primary electrons rather inefficient at production of excited or ionised states.

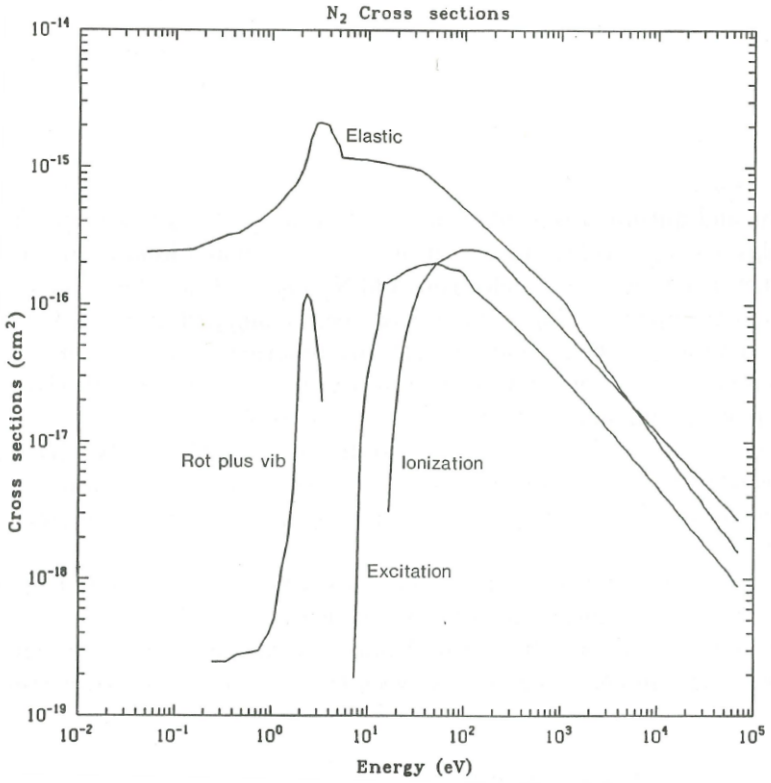

Figure 2.11: Cross-sections as a function of energy for excitation and ionisation of atmospheric N_2 by electrons. Figure reproduced from Rees (1989).

Therefore, the energies of the primary electrons determine the penetration depth into the atmosphere, with higher energy electrons penetrating further than lower energy electrons. Figure 2.14 illustrates this by showing the total ion production rate for monoenergetic beams of electrons that each have the same energy flux, but differing energies, precipitating into the atmosphere. This figure also shows that as the energy is increased, fractionally more of the production occurs at lower altitudes than at higher altitudes. This too is a consequence of the energy dependence of the cross-sections, as the higher energy electrons are less likely to interact at higher altitudes due to both the reduced cross-section at higher energy and the reduced atmospheric densities at higher altitudes. The production rates for energy spectra which have a Maxwellian spectral shape will have a lower altitude of peak ionisation, because greater energy fluxes are contained at higher energies (see figure 2.8). Maxwellian spectra also exhibit a greater spread in energies across their energy spectrum, causing energy from Maxwellian spectra to be deposited over a wider altitude range than Gaussian spectra. Finally, production of excited and ionised states occurs predominantly by the energy-degraded primary and secondary electrons as these lower energy electrons have a larger cross-section for interaction.

The excited or ionised states of N_2, O_2 and O eventually recombine or de-excite, losing energy in the process. This energy is often lost radiatively, through the emission of a photon, but can also be lost through collisional de-excitation for long-lived excited or

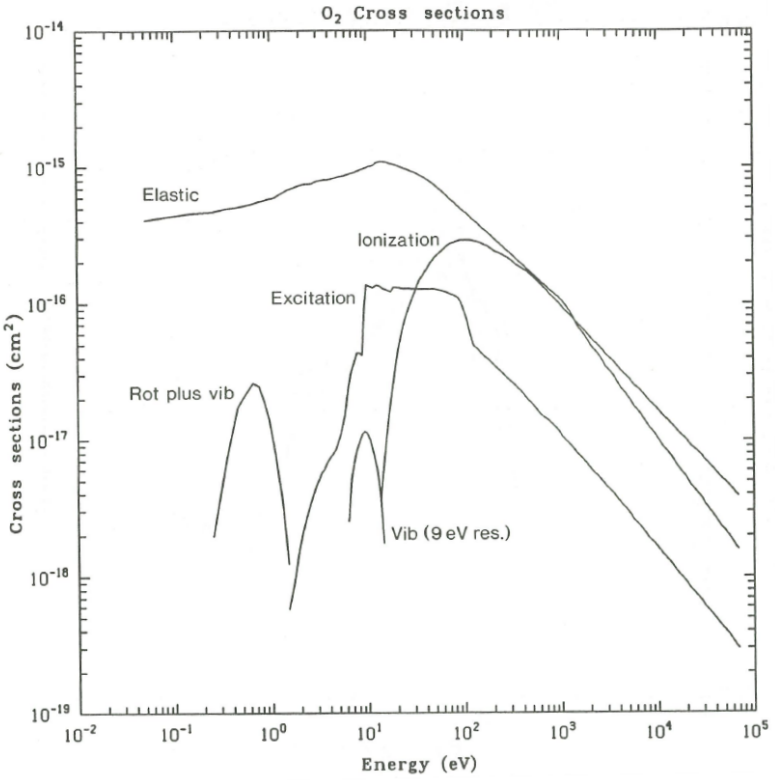

Figure 2.12: Cross-sections as a function of energy for excitation and ionisation of atmospheric O_2 by electrons. Figure reproduced from Rees (1989).

ionised states. The wavelength of these emitted photons depends on the energy gap between the transitioning states in the excited or ionised atoms and molecules. While multi-wavelength observations of the aurora, such as white-light imagers, are able to provide some information about the characteristics and behaviour of the aurora, spectral observations are required to fully investigate and quantify the physics of the aurora.

As both atomic and molecular species are excited or ionised by the auroral precipitation, the auroral emission spectrum will exhibit both atomic and molecular features. Atomic emissions are characterised by line emission due to electron transitions between the electronic states in the atom, whereas molecular spectra are more complex, and exhibit a distinct band-like structure. The band-like structure arises because molecules have additional degrees of freedom in the form of vibrational and rotational states.

Figures 2.15, 2.16 and 2.17 show the auroral spectrum at wavelengths between 4500 Å and 9000 Å, where the unit Å is the Angstrom and 1 Å = 0.1 nm. The top panels of these plots show an observed (solid line) and a synthetic (dashed line) auroral spectrum, and also indicate the wavelengths of the atomic transitions. The bottom panels show the relative contributions to the auroral brightness from the different electron transitions in the N_2 and O_2 molecules. Transitions between different electronic levels produce a band

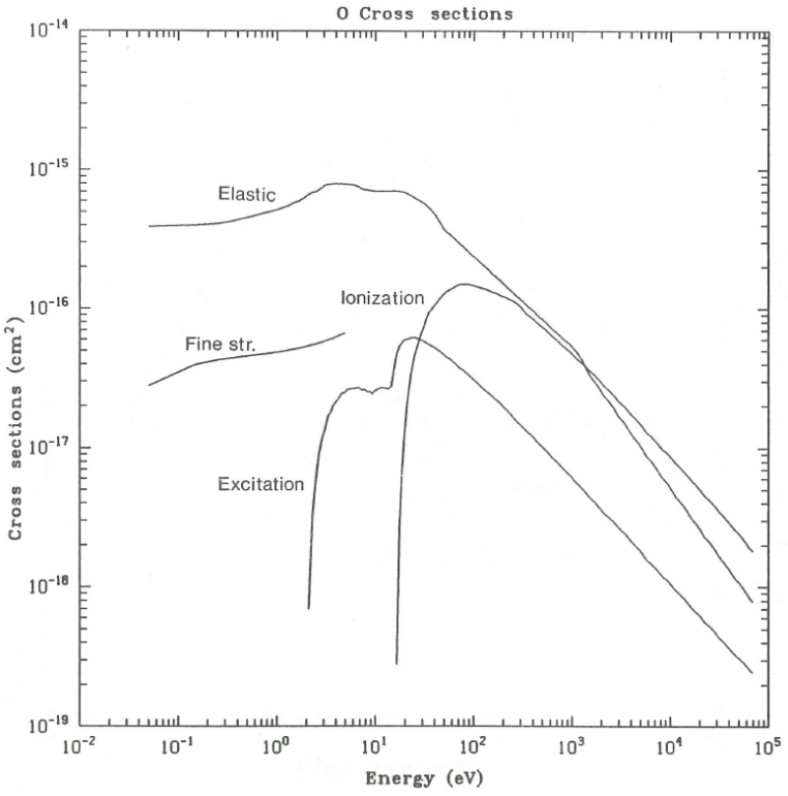

Figure 2.13: Cross-sections as a function of energy for excitation and ionisation of atmospheric O by electrons. Figure reproduced from Rees (1989).

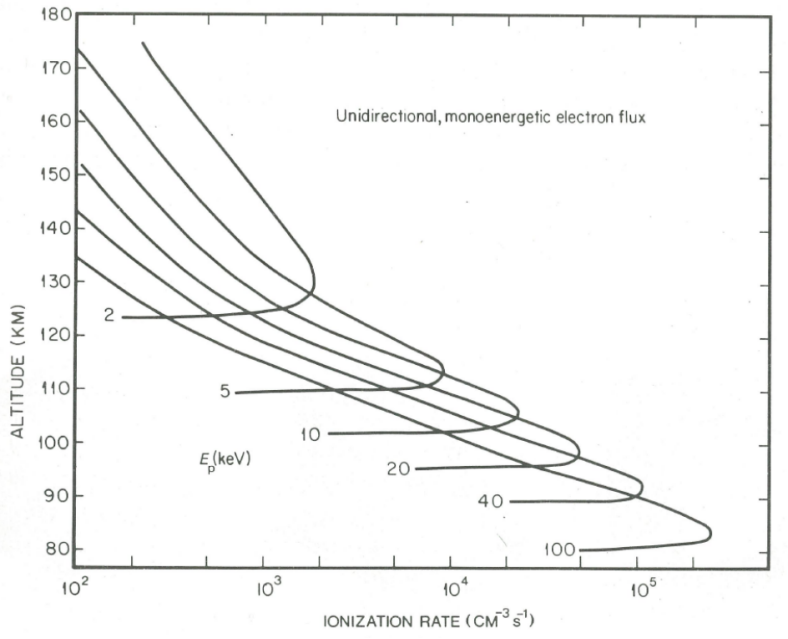

Figure 2.14: Ionisation rate profiles for monoenergetic electron precipitation with energies E_p. Figure reproduced from Rees (1989).

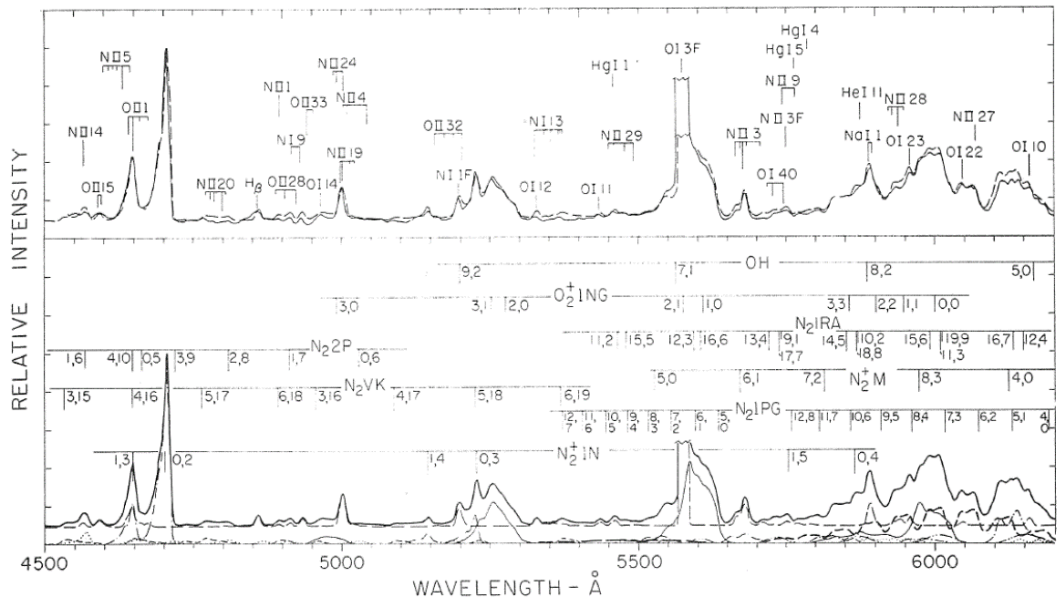

Figure 2.15: The auroral emission spectrum between 4500 Å and 6200 Å at 10 Å resolution. Figure reproduced from Jones (1974).

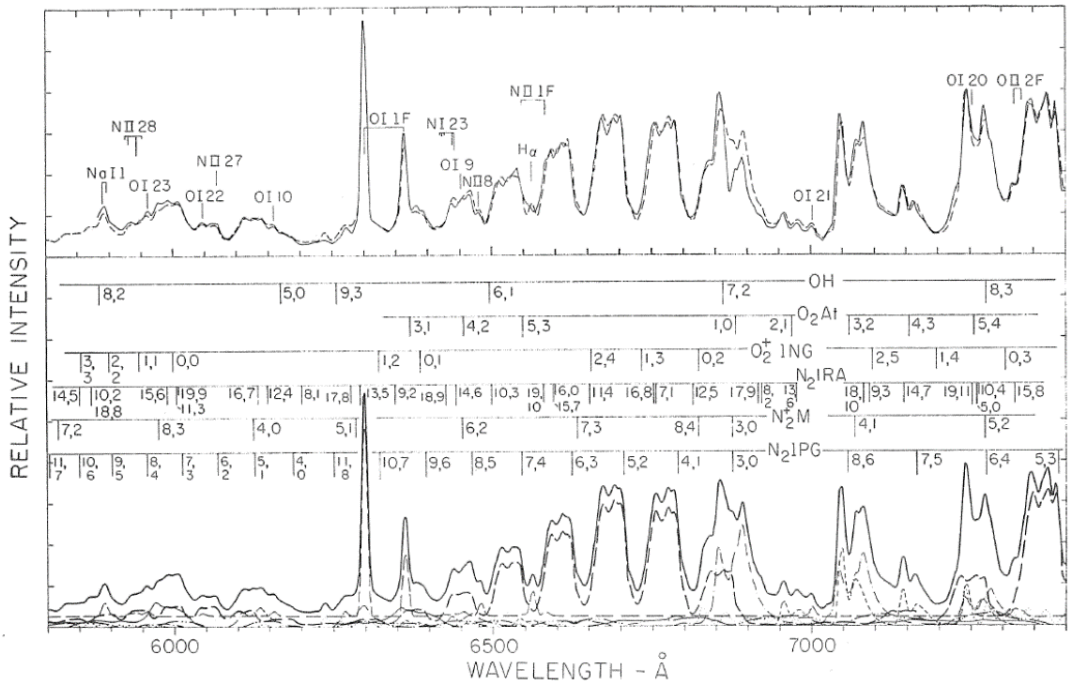

Figure 2.16: The auroral emission spectrum between 5800 Å and 7400 Å, continued from figure 2.15. Figure reproduced from Jones (1974).

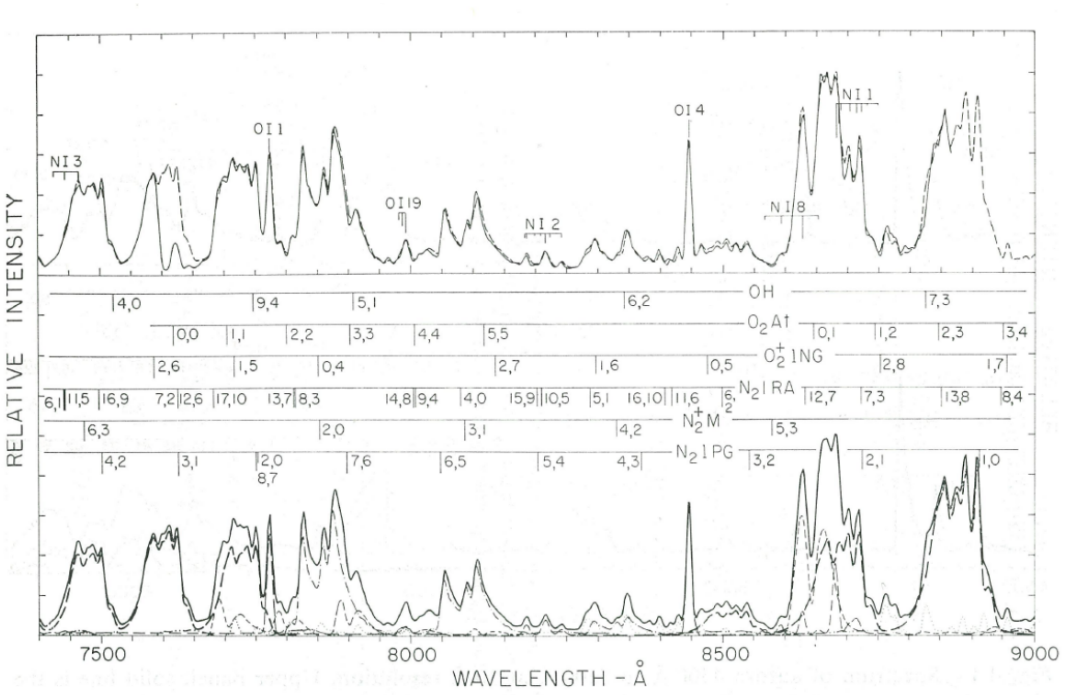

Figure 2.17: The auroral emission spectrum between 7400 Å and 9000 Å, continued from figure 2.16. Figure reproduced from Jones (1974).

of emission and are referred to by specific names, which are indicated in the middle panels of these figures.

The notation used for molecular electronic states are molecular term symbols in the form ${}^{2S+1}\Lambda^{+,-}_{u,g}$, where S is the spin quantum number, Λ is the orbital angular momentum quantum number, and the $+, -$ superscripts and u, g subscripts indicate various parities of the molecule. The angular momentum quantum number is itself denoted by a Greek capital letter, where $\Sigma = 0$, $\Pi = 1$, $\Delta = 2$, $\Phi = 3$. The superscript after the angular momentum quantum number indicates the nature of the reflection symmetry of the electron wavefunction about a plane containing the inter-nuclear axis; a '+' indicates symmetry whereas a '−' indicates anti-symmetry. This superscript is only used for Σ states and is dropped for higher order angular momentum states, which are degenerate and contain both symmetric and anti-symmetric states. The 'g' and 'u' subscripts stand for 'gerade' and 'ungerade', which are German for 'even' and 'odd' respectively, and indicate even or odd parity of the electron wavefunction about a centre of symmetry, which will be the mid-point between the two atoms for N_2 and O_2. Finally, the Roman characters are used to denote different electronic states of the molecule, where 'X' represents the ground state and excited states are labelled in order of increasing energy by the letters 'A', 'B', and so on. An upper-case character indicates that the excited state has the same multiplicity as the ground state, whereas a lower-case character indicates that it does not.

For example, the emissions labelled '$N_2$1PG' are the 1^{st} positive band system, and

represent transitions between B $^3\Pi_g$ and A $^3\Sigma_u^+$ electronic states in molecular nitrogen. The potential energy curves for these two electronic states are shown in figure 2.18 and the ground states of these energy levels are shown in figure 2.19. Each molecular electronic state is split vibrationally and the numbers separated by commas, in the form $(i,\ j)$, represent transitions between the i'th vibrational state in the upper electronic state, to the j'th vibrational state in the lower electronic state. These individual bands are then further split by the rotational states, such that they produce the distinct bands of emission shown in figures 2.15, 2.16 and 2.17. The specific emissions observed by the ASK instrument are further discussed in section 3.1.

Observed aurora has two generally morphologies: diffuse and discrete. Discrete aurora are bright and distinct features with sharp outlines whereas diffuse aurora are less intense and have no distinct form. The morphology of the aurora can also be determined from the energy spectrum of the precipitating electrons. Discrete forms typically have a more Gaussian or monoenergetic spectrum, indicative of field-aligned acceleration processes, whereas diffuse forms have more Maxwellian spectral shapes, and are indicative of thermalised plasma sheet electrons which are scattered into the loss-cone and subsequently precipitate into the atmosphere.

2.3 Acceleration Processes

The energy spectra of precipitating auroral electrons show the electrons reach the upper atmosphere with energies in the keV or tens of keV range. These precipitating electrons must be accelerated by an electric field that is aligned with the magnetic field to gain enough energy to overcome the magnetic mirroring effect and precipitate into the atmosphere. Such electric fields are typically referred to as parallel electric fields. Early evidence for parallel electric fields came from measurements of the energy spectrum of the precipitating electrons and velocity distributions of ions.

Evans (1974) modelled the effects of a parallel electric field and showed that these could reasonably reproduce previously observed monoenergetic peaks in electron spectra. Evans (1974) also explained the presence of the low-energy tail in the spectrum as being due to albedo electrons. These albedo electrons are back-scattered primary or secondary electrons, and possess a lower energy than before the collisions. The energy of the albedo electrons is insufficient to overcome the parallel electric field which initially accelerated the primaries, and so the albedo electrons are reflected downwards by the parallel electric field. Measurements of ion velocity distributions at altitude of >1 R_E have shown significant upward ion flows (Mozer et al., 1980). The lack of any corresponding signature in complementary electron velocity distribution measurements indicates that the ions are being accelerated upwards from below, consistent with a parallel electric field that accelerates electrons downwards.

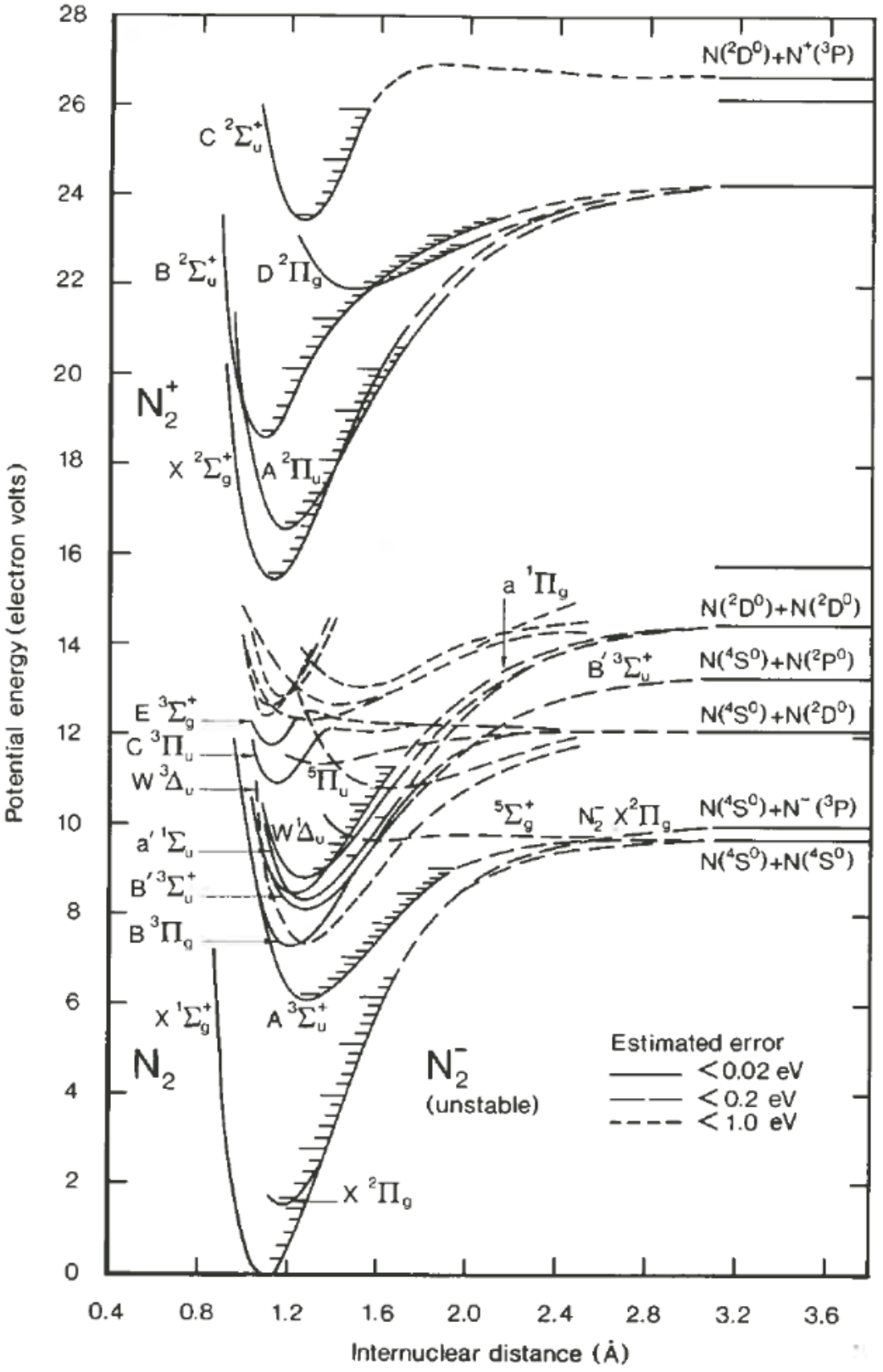

Figure 2.18: Potential energy curves for the electronic states of neutral and ionised N_2 molecules. Figure reproduced from Rees (1989).

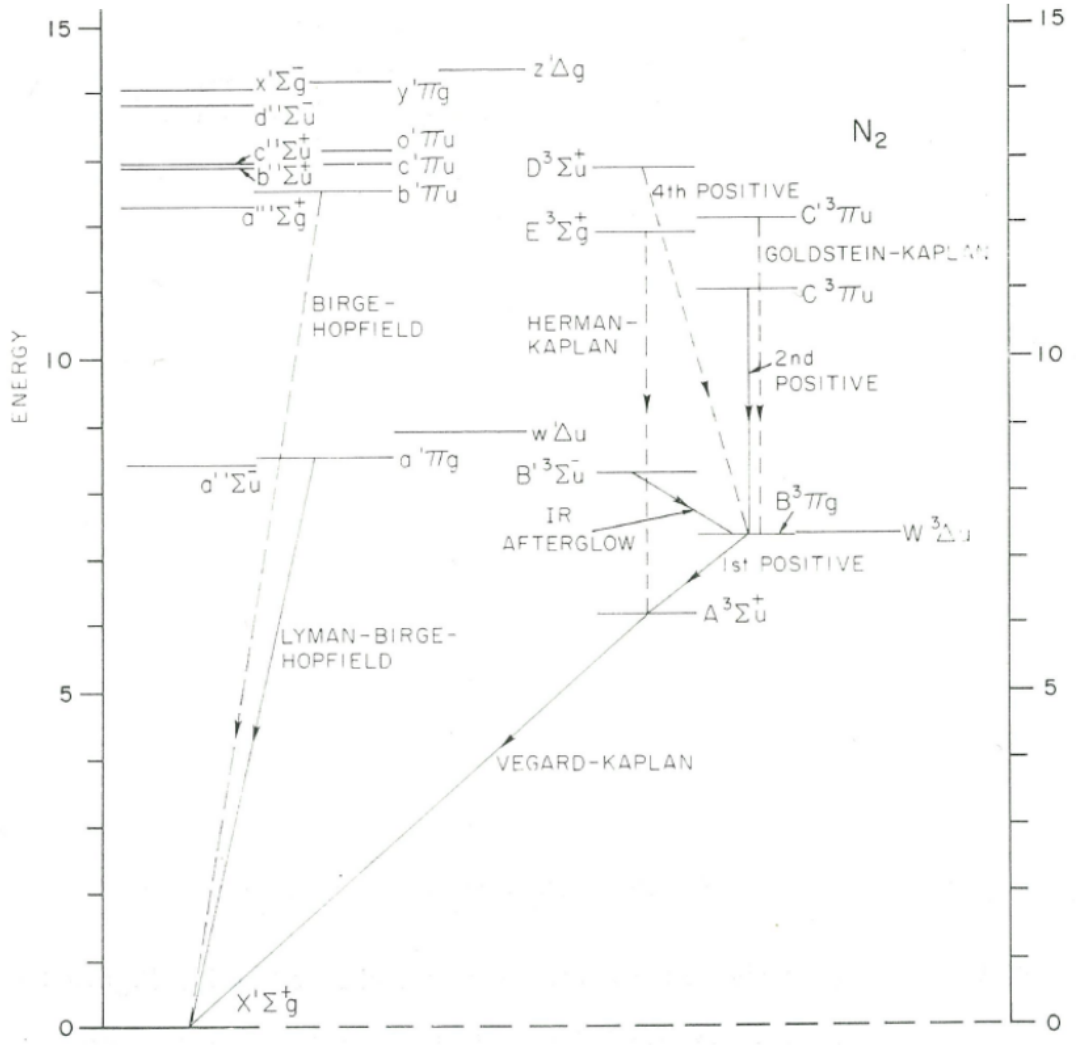

Figure 2.19: Energy level diagram showing the energies of the ground vibrational states in each electronic state of the N_2 molecule. Figure adapted from Jones (1974).

Reiff et al. (1988) used conjunctive satellite-based particle measurements from two satellites at different altitudes along the same auroral magnetic field line to infer the presence of a kV-sized field-aligned potential drop below 1-2 R_E, where R_E is the Earth radius. These field-aligned potential drops and the presence of the inverted-V signatures in the spatial structuring of the auroral electron energy spectrum suggest a U-shaped electric potential configuration at altitudes of 5000-8000 km. However, simultaneous multi-point observations are required to confirm the existence of such potential structures. Marklund et al. (2001) used such multi-point observations from the Cluster satellites to investigate the formation of such a potential structure, albeit for a positively charged potential structure. The inferred potential structure, and associated diverging electric fields, are shown on the right side of figure 2.20. Such quasi-static, potential structures are thought to be the cause of larger scale aurora. The structure of the associated negatively charged potential structure, which powers larger scale auroral features such as auroral arcs or

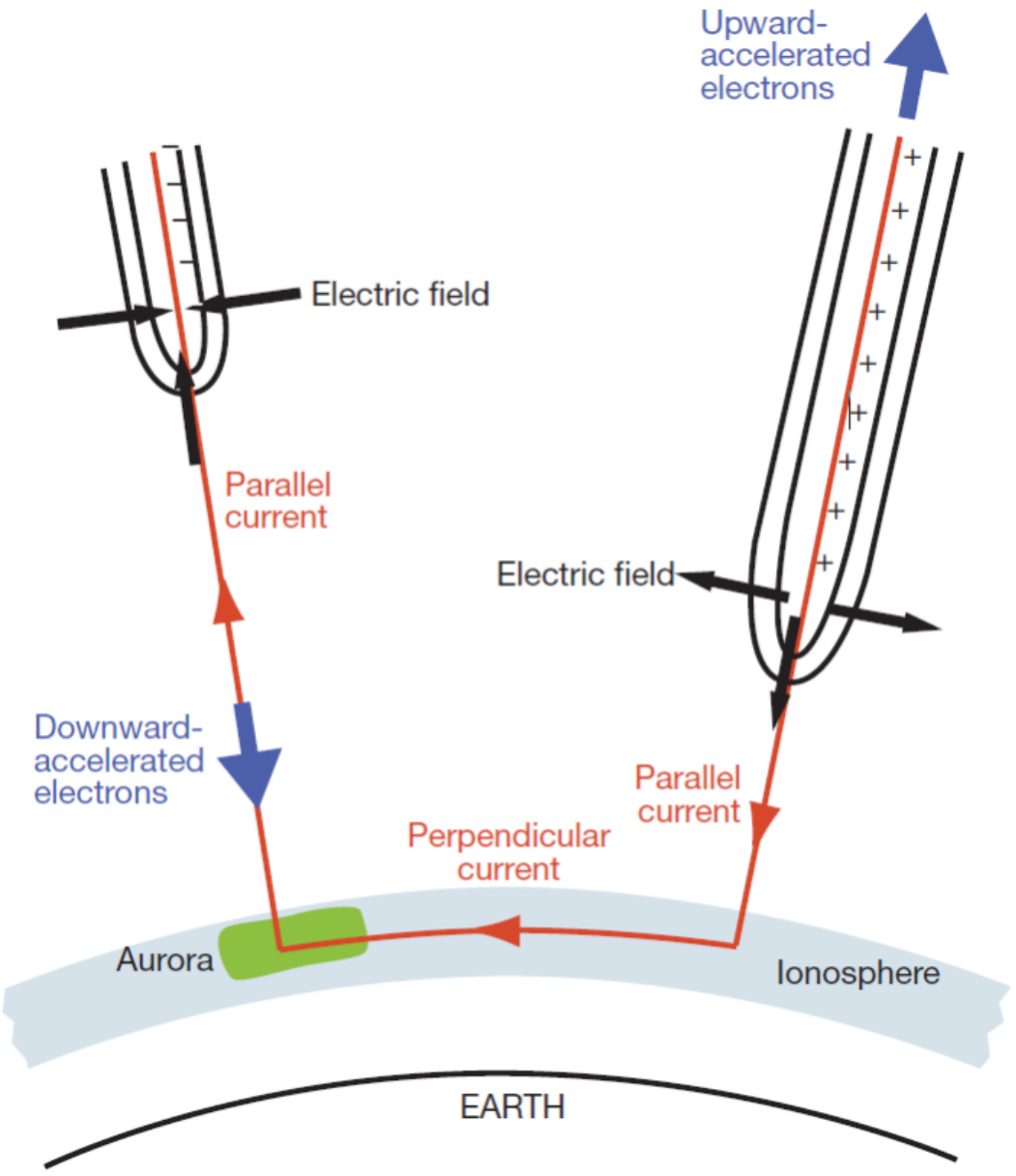

Figure 2.20: Auroral acceleration structures and associated electric fields for large scale aurora. Figure reproduced from figure 1 of Marklund et al. (2001).

arc systems, is shown on the left side of this same figure.

While quasi-static potential structures satisfactoraly explain the acceleration processes which cause larger scale aurora, they are unable to explain the finer scale structuring. A statistical study of the scale size of intense auroral electric fields, observed by the Cluster satellites, yielded scales sizes of a few kilometres, with a peak at 4 km (Johansson et al., 2007). A plethora of other theories have been proposed to explain the generation of parallel electric fields and acceleration of auroral electrons, however the most widely invoked, and successfully applied, has been that of Alfvén waves (Hasegawa, 1976; Goertz and Boswell, 1979; Stasiewicz et al., 2000).

Alfvén waves are electromagnetic oscillations inside a plasma at frequencies lower than the ion cyclotron frequency. The magnetic field inside the plasma provides a restoring force to the oscillations and the mass of the ions inside the plasma provide a source of inertia. Alfvén waves propagate along the magnetic field lines, with the oscillations in the electric and magnetic fields perpendicular to both each other and the direction of the wave motion. However, such an Alfvén wave, by definition, cannot produce a parallel electric field and is unable to accelerate charged particles. To generate a parallel electric field, the Alfvén wave must propagate obliquely to the magnetic field lines. Such waves are called shear Alfvén waves and are initiated by sheared plasma flows perpendicular to the magnetic field. These Alfvén waves are a key component of the coupling and feedback between the magnetosphere and ionosphere, allowing the transfer of energy and particles between the two.

Chaston et al. (2003) examined the widths and brightnesses of auroral arcs driven by inertial Alfvén waves, which are Alfvén waves which propagate faster than the electron thermal velocity. Using satellite observations and results from a magneto-hydrodynamic (MHD) simulation they showed that inertial Alfvén waves could produce bright auroral arcs, but that typical widths of such arcs were of the order of 900 m. More recently, Chaston et al. (2011) showed sheared flows, and associated magnetic reconnection, may drive a cascade of structuring to smaller scales, with energy being transferred from Alfvén waves with large wavelengths to those with smaller wavelengths.

However Alfvén waves are only the method by which the electrons are accelerated. Shear Alfvén waves are initiated by sheared plasma flows perpendicular to the magnetic field. As the magnetic field moves with the plasma, this induces a shear in the magnetic field itself. If the shear becomes too large, localised near-Earth reconnection occurs, launching Alfvén waves. 3-D multi-fluid simulations of shear-induced reconnection have shown the formation of fine scale structuring in the form of striated current sheets (Otto and Birk, 1993) and narrow and dynamic field aligned potential drops (Lanchester et al., 1997).

MHD simulations have also shown the formation of small scale structuring (Chaston et al., 2011). Chaston and Seki (2010) used a resistive layer between the magnetosphere and ionosphere to investigate the relative effects of magnetic reconnection and the Kelvin-Helmholtz instability. When the resistive layer was absent, a highly structured and filamentary potential profile developed, which was interpreted primarily by magnetic reconnection, whereas when the resistive layer was included, a more quasi-static or inverted-V type potential structure was formed. More recently, Chaston (2015) presented optical and particle observations and analysis that provide clear evidence for magnetic reconnection structuring the aurora at small scales. A vorticity analysis of the prompt optical observations suggests a sheared flow perpendicular to the magnetic field across the auroral arc. As these observations are prompt these flows represent the motion of the generator, in the auroral acceleration region, and not motions in the ionosphere. The results of Lanchester et al. (1997) showed sheared flow across a simulated

auroral arc, but in the ionosphere, that was initiated by magnetic reconnection. These two results suggest that shears in the ionosphere and magnetosphere may be linked by this process of magnetic reconnection.

2.4 Electric fields

Electric fields are a ubiquitous feature of the ionosphere. They are caused by the motions of electrons and ions and act to modify the motions to preserve a divergence-free current density. As the ionospheric response to energetic particle precipitation, the aurora is intimately linked with electric fields. This relation has been studied at both large and small scales using a multitude of instrumentation. Satellite and rocket observations can provide in-situ measurements of electric fields at sub-millisecond temporal resolution. Due to the rapid motion of the rocket or satellite, such observations are typically interpreted as measurements of the spatial, not temporal, variation of the electric field. Marklund et al. (1982) studied the electrodynamics of an auroral feature, 20 km in size and aligned in the east-west direction, using rocket-borne electric field measurements. These observations revealed a strong, predominantly northward electric field directed toward the southern boundary of the auroral feature. At smaller scales, (Marklund et al., 1994) reported on regions of very narrow (≈1km) and intense (≈1V/m) electric field observed by the Freja satellite, tentatively linking these fields to an east-west aligned vortex street structures of black aurora.

Radar observations from the ground allow the temporal evolution of auroral arc electric fields to be studied, though typically at resolutions not better than orders of a minute. Electric field measurements are not obtained directly, rather they are inferred from the observed plasma velocities using the $\mathbf{E} \times \mathbf{B}$ drift. Additionally, optical observations are often used to aid interpretation of the radar observations. Aikio et al. (2002) used the mainland EISCAT radars to investigate the electric fields of stable auroral arcs, between 15 and 50 km in size, as they drifted through the radar beam. The measured electric fields were found to be directed perpendicular to the optical auroral arc and up to 100 mV/m in strength. At smaller scales, Lanchester et al. (1996) studied the electrodynamics of a narrow auroral filament, with a width of about 1 km, using the EISCAT radars. These observations, at 3 second resolution, found electric fields of up to 400 mV/m at an altitude of 278 km surrounding a bright auroral filament. Further, the electric field beside the filament increased in magnitude when the auroral brightness increased, suggesting that larger electric fields could exist on even shorter timescales. These results of Lanchester et al. (1996) were the motivation for the design and construction of the ASK instrument described in section 3.1, with the method described in chapter 7 vital to the design rationale.

Estimates of ionospheric parameters, including electric fields, have also been extracted from optical observations of airglow and aurora. Gustavsson et al. (2001) used optical observations of heater induced airglow to estimate the neutral wind velocities at the peak emission height. More recently, Dahlgren et al. (2009) used observations of auroral brightness from the ASK instrument to estimate plasma velocities, from which ionospheric electric fields were inferred. Plasma velocities were extracted from the observations by tracking the motion of the afterglow from the metastable O^+ ion, which was produced during auroral precipitation just prior, using an assumed emission height for the afterglow. Inferred electric fields of the order of a few tens of mV m^{-1} were obtained after the auroral precipitation subsided; however, as the motions of the precipitation source and the plasma could not be separated using optical observations alone, their method could not be applied whilst the precipitation was occurring.

A model based on the methods of Gustavsson et al. (2001) and Dahlgren et al. (2009) is used in chapter 7 to estimate the plasma velocities and ionospheric electric fields during an active auroral event at sub-second resolution for the first time. This method goes beyond that presented in Dahlgren et al. (2009) as it overcomes the two main limitations of that method. By solving the continuity equation for O^+ ions in a 3-D volume, and having knowledge of the auroral particle precipitation that is occurring, the effects of production, drift, and emission for the O^+ ions can be separated and quantified.

Chapter 3

Instrumentation

This chapter describes the optical and radar instrumentation that is used in this work to study the aurora and the auroral ionosphere. The author has been involved in the maintenance and operation of the optical instrumentation during the winter dark seasons since October 2010. This involved numerous tasks such as selecting data for archiving or deletion, focusing and aligning the optical instrumentation and calibrating the data. The author has also been responsible for operating the EISCAT Svalbard Radar (ESR) during observation campaigns.

3.1 ASK

The Auroral Structure and Kinetics (ASK) instrument is used to make simultaneous multi-monochromatic observations of the aurora. The ASK instrument consists of three identical imaging systems, which utilize electron-multiplying charge coupled device (EMCCD) technology, and two photometers. The photometers are not used in this work. Each imaging system is produced by combining an EMCCD detector with a 75 mm f/1 lens, yielding an imager which has a field of view of 6.2° x 6.2°. Each imaging system can also be equipped with a telescope, further reducing the field of view to 3.1° x 3.1°. Each detector is 512 by 512 pixels in size, however observations are downsampled to 256 by 256 pixels to improve the signal to noise ratio and reduce data storage demands. Downsampling results in images that have a spatial resolution of approximately 20 m at typical auroral stopping heights for energetic precipitation.

Attached to each imaging system is one of four narrowband interference filters. The filter passbands are centred on auroral emissions at 562.0 nm, 673.0 nm, 732.0 nm and 777.4 nm, selecting emissions from O_2^+, N_2, O^+ and O respectively. The transmittance curves for each filter are shown in figure 3.1; these curves are produced from digitization of hardcopies supplied by the filter manufacturer. The specifics of the emissions observed

by each filter are outlined below. The sensitivities of each emission to the energy of the precipitation is discussed more fully in section 4.2.

562.0 nm

The 562.0 nm filter, which has a full width half maximum (FWHM) passband of 2.6 nm, selects a particular band of emission from the O_2^+ 1^{st} negative band system. This band system is often abbreviated to O_2^+ 1NG, and originates from the $b^4\Sigma_g^- \rightarrow a^4\Pi_u$ electronic transition. In O_2^+, the $a^4\Pi_u$ state represents the first excited electronic state, and the $b^4\Sigma_g^-$ state represents the third excited electronic state. These electronic states are further split, by the vibrational and rotational degrees of freedom of the molecule. The 562.0 nm filter selects only the (1,0) band, which represents a transition from the first excited vibrational state of $b^4\Sigma_g^-$ electronic state to the ground vibrational state of $a^4\Pi_u$ electronic state, within the O_2^+ 1NG system. Figure 2.15 shows the wavelength position of the (1,0) band head within the auroral emission spectrum.

The O_2^+ ions are produced by ionisation of atmospheric molecular oxygen by energetic electron precipitation. The cross-sections for O_2, shown in figure 2.12, peak at energies of around 10 eV; however significant production of O_2^+ ions does not occur below energies of around 1 keV. At lower energies the production of O_2^+ ions is diminished because the stopping altitude rises as the energy falls, and at the stopping altitudes for sub-keV energies the mixing ratio of molecular oxygen is significantly reduced compared to the altitudes for keV energies. The 562.0 nm emission is therefore an indicator of energetic (keV-energy) electron precipitation.

673.0 nm

The 673.0 nm filter, which has a FWHM passband of 14 nm, selects emission from a pair of bands within the N_2 1^{st} positive band system. This band system is hereafter referred to as the N_2 1PG band system, and is produced by the $B^3\Pi_g \rightarrow A^3\Sigma_u^+$ electronic transition. The 673.0 nm filter isolates emissions from the (5,2) and (4,1) bands of the N_2 1PG band system, where the number notation used here has identical meaning to that of the O_2^+ 1NG band system.

The total cross-sections for excitation of the N_2 molecule in figure 2.11 show a peak at around 5 eV. However, production of N_2 molecules into the $B^3\Pi_g$ state occurs at both keV and sub-keV electron precipitation energies. The cause for this relative insensitivity is that the N_2 mixing ratio does not experience as significant a reduction as that for O_2. Later work presented in this thesis, in particular the results of the modelled height integrated brightnesses in figure 4.2, does however show a slight reduction in sensitivity at lower precipitation energies; however this reduction is not as pronounced as that for the O_2^+ ion.

The wavelength region surrounding the (4,1) and (5,2) bands is devoid of any significant auroral or airglow contamination, which allows the wavelength passband to be wider compared to the other three filters. As a result of this wide passband, images taken using the 673.0 nm filter have the best signal-to-noise ratio.

732.0 nm

The 732.0 nm filter, which has a FWHM passband of 1.0 nm, isolates emissions, that form an emission doublet at 732.0 nm, from metastable O^+ ions. The dynamics of the O^+ ion are discussed in section 7.2. Production of these ions exhibits no strong dependence upon the energy of the electron precipitation. However, the observed brightnesses do exhibit a strong energy dependence; they are brighter when the energy of the precipitation is low. This is due to strong quenching of the O^+ ions at lower altitudes, leaving the ions produced at higher altitudes, by lower energy precipitation, to emit.

Contaminating emissions are present within the passband of the ASK2 filter. Emission from the (8,3) band of Hydroxyl (OH) is one contaminant, however the OH emission brightness is assumed not to vary significantly over the short timescales of the events studied here, and is adequately removed by background subtraction. Auroral emissions from the (5,3) band of the N_2 1PG band system are also present. Dahlgren et al. (2008a) examined spectrographic data from auroral emissions at wavelengths between 730 nm and 740 nm, finding that at times of energetic precipitation the spectrum was dominated by emissions from N_2, whereas at times of lower energy precipitation the auroral spectrum was dominated by O emission. Determination of the energy here was performed using radar observations of electron density to which the 'flux-first' method was applied (Palmer, 1995; Lanchester et al., 1996). Spectrographic observations may allow the removal of the contaminating (5,3) band emission, however such a technique would require these complementary observations. Spry et al. (2014) presented a technique to allow removal of the contamination using observations from ASK at 673.0 nm. This technique uses the fact that the brightness of the (5,3) band emission, which contaminates the 732.0 nm observations, is proportional to the brightness of the (5,2) and (4,1) band emissions, which are measured when the 673.0 nm filter is used. Spry et al. (2014) developed a temperature dependent synthetic spectrum of emission from the N_2 1PG band system, which allows the brightness of the (5,3) band emission to be estimated, and removed, using observations of the 673.0 nm brightness and the neutral temperature. Where observations at 673.0 nm are not available, the modelling methods described in chapters 5 and 6 can be used to produce modelled images of the emission observed through the 673.0 nm filter to permit use of the Spry et al. (2014) technique. These techniques are described in greater detail in the analysis of the 732.0 nm emission presented in chapter 7.

777.4 nm

The 777.4 nm filter, which has a FWHM passband of 1.5 nm, selects an emission triplet which is due to the 3s ^{5}S - 3p ^{5}P transition in atomic oxygen. There are two processes that produce the upper state of this transition: dissociation of molecular oxygen and excitation of atomic oxygen. Both of these processes are due to interaction with energetic electrons and both occur under auroral precipitation conditions. The dissociative process occurs when the energy of the precipitation is high; allowing the electrons to penetrate the atmosphere to altitudes at which the molecular oxygen mixing ratio is significant. In contrast, the excitative process occurs when the energy of the precipitation is low. Again, this is due to the mixing ratio being significant at altitudes that correspond to typical penetration depths for low energy precipitation. There are no contaminating auroral emissions present in this filter.

Observations made by using these filters may contain contaminating emissions which must be removed prior to analysis of the observations. Contamination may be present due to contaminating auroral or airglow emissions, such as discussed with the 732.0 nm emission. Airglow contamination is removed by 'background subtraction' under the assumption that the airglow brightness does not vary significantly over the timescales of the analysed events. In the analysis presented in the later chapters, a minimum background is used. This minimum background corresponds to the lowest median observed brightness, over the imager field of view and a period of two seconds, in an interval 20 minutes long surrounding the event.

The three cameras are co-aligned with each other and ASK observes in the direction of the local magnetic zenith. The events studied in this work all come from the winter 2006-07 dark season. During this season ASK was co-located with the EISCAT Tromsø radar station near Ramfjordmoen, Norway (69.6° N, 19.2° E). However in all other seasons of ASK operation, the instrument was co-located with the EISCAT Svalbard radars (78.2° N, 16.0° E).

The capability of switching filters and field of view of each imager, by adding or removing the telescope, allows the ASK instrument to be adapted. During this first observation seasons, the filters on the ASK instrument were switched somewhat frequently. The event first analysed in chapter 5 was observed using the 562.0 nm, 732.0 nm and 777.4 nm filters, whereas the event first analysed in chapter 6 was observed using the 673.0 nm, 732.0 nm and 777.4 nm filters. In these observations the 777.4 nm emission is a vital observation, as this emission exhibits a clear sensitivity to precipitation energy. Observations at 732.0 nm have almost always been available, as this emission is necessary to be able to track the motions of long-lived ions using the techniques discussed in chapter 7.

For the analysis of ionospheric plasma flows using the long-lived O^+ ion, the third imager should use the filter at 673.0 nm. These observations are required to allow removal of the contamination from the observed 732.0 nm emission and to estimate characteristics of the precipitating electrons (Lanchester et al., 2009). The 562.0 nm emission can also be used to estimate precipitation characteristics (Dahlgren et al., 2008b), and while the emission modelling techniques developed in the later chapters of this thesis do allow modelled images of the 673.0 nm emission to be produced, the contamination is more reliably removed if observations of the 673.0 nm emission are present. The 562.0 nm emission is also disadvantaged over the 673.0 nm emission when used in the emission ratio technique to estimate energy. The emission brightnesses of the (5,2) and (4,1) bands of the $N_2$1PG system are significantly higher than the (1,0) band of the O_2^+ 1NG system (Jones, 1974). The transmittances of the filters, shown in figure 3.1, show that the transmittances of the 562.0 nm filter are lower than that of the 673.0 nm filter, further amplifying the difference in emission brightness. The reduced brightness of the observed 562.0 nm emission causes noise present in the observations to result in the precipitation characteristics having larger uncertainties when the 562.0 nm filter is used compared to when the 673.0 nm filter is used.

Data is acquired by the imaging systems in blocks of data, known as megablocks, that are 20 minutes in duration. Megablocks from each camera are produced simultaneously, so that metadata, such as the start time and framerate, are consistent. Each camera produces two megablocks of data during a given interval: a high resolution megablock, with a framerate of between 5 and 40 Hz, and a low resolution megablock, with a framerate of 0.5 Hz. The images in the low resolution megablock are derived from the high resolution megablock using frame averaging. For most of the dark season, high resolution megablocks are typically obtained using a framerate of 20 Hz. This framerate provides a good trade-off between capturing the dynamics of the aurora and the storage and archiving needs of acquired data. ASK is often used during specific observational campaigns when complementary data from a variety of other instrumentation, such as radar or wider field of view optics, are also acquired. During these campaigns a higher framerate, of 32 Hz, is used.

Each camera is controlled by a desktop computer, which is in turn controlled by a master computer. The camera computers each have 200 GB data storage and the master computer has 840 GB of data storage. Data from the camera computers are periodically cleaned and moved to the master computer, where they are archived to magnetic tape. The data is cleaned and archived at least once daily, as when operating at 20 Hz the 200 GB disks are full after only 26 hours. The process of cleaning the data involves removing irrelevant high resolution observations, such as those of cloudy skies or of clear skies with no aurora present. The low resolution observations are always kept. The cleaned data are moved to the master computer to free up disk space for further

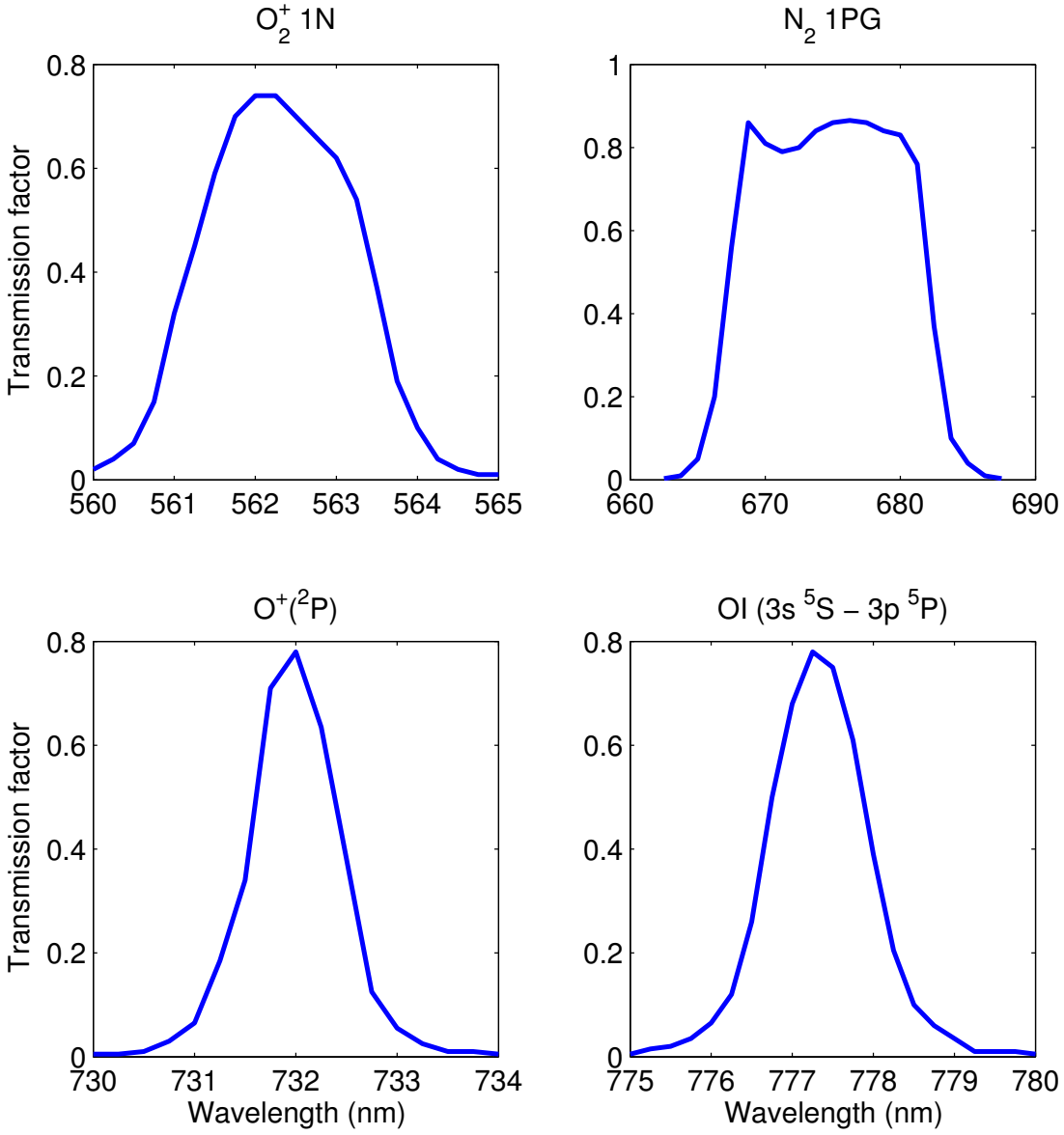

Figure 3.1: Transmission curves for the filters which observe O_2^+ at 562.0 nm (upper left), N_2 at 673.0 nm (upper right), O^+ at 732.0 nm (lower left) and O at 777.4 nm (lower right). All axes have wavelength, in nm, along the horizontal axis and transmission co-efficient along the vertical axis.

observations. Long term archiving of the data is achieved through the use of 200 GB LT02 magnetic tapes.

3.2 Radar

Properties of the auroral ionosphere can be sensed remotely by radars using coherent or incoherent scatter techniques. Both techniques utilise the Thomson scattering of radio waves by ionospheric electrons. In coherent scatter the radio waves are scattered by structured field-aligned ionospheric irregularities, which are electron density gradients along the propagation path of the radio wave. Such irregularities are produced by auroral electron precipitation. At typical duty cycle powers (hundreds of Watts) and integration times (minutes) used in coherent scatter radars, backscatter from a single irregularity is undetectable. However, where scatter from multiple irregularities constructively interferes a detectable signal results. Such constructive interference relies on satisfying the Bragg condition, that is the wavevector of the field-aligned ionospheric irregularities is twice the wavevector of the radio waves (Milan et al., 1997). Radio waves are also scattered by weaker density gradients, such as those due to random thermal motions of the electrons. The backscatter is termed incoherent scatter, because it does not originate from a coherent structure, and is typically much weaker than coherent scatter.

Thermal fluctuations in the electron densities on scales larger than the Debye length are attenuated by the larger, more massive ions to maintain the quasi-neutrality of the ionosphere at large scales. Therefore, although the radio waves are scattered by the electrons, the spectrum at wavelengths longer than the Debye length are dominated by the properties and characteristics of the ionospheric ions. The spectrum of the backscatter can be used to extract various ionospheric parameters, such as the electron density, ion temperature, ratio of electron to ion temperature, and line of sight plasma velocity. However, the random nature of the thermal fluctuations means that a single measurement of the backscattered spectrum cannot be used individually to determine ionospheric plasma parameters. Instead multiple measurements from a short period of time, typically of the order of a few seconds, are cross-correlated to smooth out the fluctuations, however this limits the temporal resolution of the measurements.

Data from two radar systems are used in this thesis. Incoherent scatter measurements of electron densities from the European Incoherent Scatter Radars (EISCAT) are used in chapter 5 to determine the energy spectrum of precipitating electrons by solving the electron continuity equation, as described in section 4.1. These data were obtained using the ultra high frequency (UHF) radar, operating at 931 MHz and located near Tromsø in Norway, in a field-aligned mode, that is measuring parallel to the magnetic field. Coherent scatter measurements of plasma velocities from the Super Dual Auroral Radar Network (SuperDARN) are used in chapter 7 to interpret plasma velocities obtained from

a novel optical-modelling method to estimate ionospheric plasma velocities. The line of sight plasma velocities are obtained from the Doppler shift of the scattered radio waves. If multi-station observations of the plasma velocity in a given volume are available, then the line of sight velocities can be combined to deduce the vector plasma velocity.

The observations from the EISCAT Tromsø radar were made using a radar experiment called 'arc1'. This experiment is able to make measurements of ionospheric electron densities at ranges between 96 and 422 km with a range resolution of around 0.9 km and at a temporal resolution of 0.44 s. These fine scale observations are necessary for the application of the inversion technique presented in section 4.1. To enable measurements to be made at such fine temporal resolutions, an alternative method of measuring the electron densities is used. The total power of the backscattered radio waves measured by the receiving antenna is directly proportional to the electron density, as higher electron densities present a larger target cross-section for the incident radio waves to scatter off. Measurements of the power profiles while still somewhat noisy, as evidenced by the recovered electron densities presented in figure 5.4, do not require an integration time as the cross-correlation of the incoherent scatter spectrum does, and allows the electron densities to probes at temporal resolutions closer to that of the sub-second dynamics of the fine scale aurora.

Chapter 4

Modelling

The aurora is primarily caused by electron precipitation into the atmosphere. Since the advent of auroral research, the need to quantify this electron precipitation and its effects on the atmosphere has driven the development of a plethora of tools to model and analyse the precipitation and its effects. This chapter focuses on several such tools that have been used in this work. In section 4.1 the method to determine the auroral electron energy spectrum is presented. Section 4.2 presents the combined electron transport and ion-chemistry model that is used to determine the effects of the electron precipitation on the upper atmosphere, primarily in terms of the excited and ionised species the precipitation produces. Finally, the tools used to model the three-dimensional distribution of selected auroral emissions are presented in section 4.3.

Both models described in sections 4.1 and 4.2 have only one spatial dimension that is parallel to the magnetic field, and are unable to model the motion of plasma perpendicular to the magnetic field. Further, neither model considers the motion of plasma along the magnetic field. The inability of these models to account for the plasma motion implies the assumption that any changes in the electron densities are solely due to the effects of electron precipitation and recombination. The effects of plasma motion need consideration when modelling of the electron energy spectrum, and the effects of excluding the plasma motion are discussed in section 4.1.

Plasma motion is less important for the modelling of the production and prompt emission rates as these are primarily dependent on the densities of the parent states (O_2, N_2, O, etc), which are assumed not to vary significantly during the short time periods of the event analysed in this work, and the energy spectrum of the precipitating electrons. However, the effects of plasma motion must be considered when modelling emission from the long-lived $O^+(^2P)$ ion, which is observed by the ASK2 camera at 732.0 nm. This ion can drift with the plasma, so the position of the production and emission for this ion depend on the plasma motion. The effects of production and drift of this ion

are considered separately. The plasma drift is analysed in chapter 7, and the production of the ion is considered here, in section 4.2.

4.1 Inversion of radar data

The inversion of radar observations of electron density is used to estimate the energy spectrum of auroral electron precipitation using the method described in the appendix of (Dahlgren et al., 2011). This inversion is achieved by parameterising the energy spectrum, using a set of node points in energy and energy flux connected by smooth cubic splines, and then searching for the parameters which minimise the Akaike Information Criterion (AIC) (Akaike, 1974). The AIC is defined as:

$$AIC = -2ln(L) + 2k \tag{4.1}$$

where k is the number of independent free parameters and L is the value of the likelihood function for the model. The AIC is used for model selection; it tests the relative accuracy of a set of statistical models for a given set of data. The first term is a goodness of fit term which decreases as the number of free parameters increase, because the model is able to better fit the data when a larger number of free parameters is used. The second term is a penalty term that penalises increasing complexity of the model; this term prevents arbitrarily complex models, which may fit to noise present in a dataset, from being selected. Therefore, the AIC determines the most likely model by making a compromise between goodness of fit and complexity of the model.

If a set of data has a finite number of observations, then a correction term is required. The corrected AIC, AIC_C, is the given by:

$$AIC_C = AIC + \frac{2k(k+1)}{n-k-1} \tag{4.2}$$

where n is the number of observations. Substituting equation 4.1 into equation 4.2 and re-arranging, the following expression is obtained:

$$AIC_C = -2ln(L) + \frac{2kn}{n-k-1} \tag{4.3}$$

The likelihood function for the χ^2 fit is given by:

$$L_{\chi^2} = \prod_{i=1}^{n} (\frac{1}{2\pi\sigma_i}) e^{-\sum_{i=1}^{n} \frac{(y_i - \tilde{y}_i)^2}{\sigma_i^2}} \tag{4.4}$$

where y_i are the values from the data, $\tilde{y}_i$ are the values obtained using the model and σ_i are the uncertainties in the observed data. The first term in equation 4.4 is a constant defined solely by the data. Substituting equation 4.4 into the expression for the corrected

AIC and re-arranging, the following expression is obtained:

$$AIC_C = \sum_{i=1}^{n} \frac{(y_i - \tilde{y}_i)^2}{\sigma_i^2} + \frac{2k(k+1)}{n-k-1} - 2C \tag{4.5}$$

where C is a constant and is the natural logarithm of the first term in equation 4.4. As the AIC informs only about the relative likelihood of a given model fitting a set of data the constant C will be the same for all models, as long as the data is unchanged, and can be neglected in the calculation of the AIC.

When applied to electron densities, the corrected AIC is given by:

$$AICc = \sum_{i=1}^{n} \frac{(n_e(z_i,t) - \tilde{n_e}(z_i,t))^2}{\sigma_{ne}^2} + \frac{2k(k+1)}{n-k-1} \tag{4.6}$$

where $n_e(z_i,t)$ is the electron density at altitude z_i and time t and $\tilde{n_e}$ is the modelled electron density.

Modelled electron density profiles are obtained using the electron continuity equation:

$$\frac{\partial \tilde{n}_e}{\partial t} = Q_{est} - (\alpha_1 n_{NO^+} + \alpha_2 n_{O_2^+} + \alpha_3 n_{N_2^+}) + \mathbf{v} \cdot \nabla \tilde{n}_e \tag{4.7}$$

where Q_{est} is the estimated production rate of electrons, n_{ION} is the density profile of the given ion, α_n is the recombination rate of electrons with the given ion and $\mathbf{v}$ is the convection velocity of the plasma.

Q_{est} is calculated as the sum of contributions from a set of monoenergetic electron spectra that are modified by the energy flux of the estimated electron energy spectrum at that energy using:

$$Q_{est} = A(z,E) \cdot \Phi_e(E,t) \tag{4.8}$$

where $A(z,E)$ is the ionisation profile matrix, which contains the calculated electron production rates for monoenergetic electron spectra with an energy E and a given energy flux, and $\Phi_e(E,t)$ is a matrix containing the time-series of estimated electron energy spectra.

The energy spectrum of precipitating electrons is modelled using the exponential of a cubic spline with $k/2$ knots. Each knot contributes two free parameters that can be fit to; one in energy and one in energy flux, resulting in k free parameters. An iterative process is used to search over the possible free parameters to find the energy spectrum that produces a modelled electron density profile most similar to the observed electron density profile. To find the true minimum of the AIC every possible function shape should be tried, however the exponential cubic spline method should be general enough to reasonably reproduce any given function shape.

In this thesis, the AIC method is applied to radar observations from a single station, which measure the electron density as a function of range along the radar line-of-sight and time. No observations are available outside of the radar line-of-sight. As such, the AIC method is unable to model or account for changes in electron density due to plasma flowing into or out of the radar line-of-sight. Inclusion of the effects of the plasma motion would necessitate multiple observations parallel to the magnetic field, such as from a radar interferometer.

To allow the energy spectra to be obtained in the absence of knowledge of the plasma motion, the convection velocity of the plasma is assumed to be zero, which allows the final term in equation 4.7 to be neglected. However, care must be taking in the interpretation of the resulting energy spectra. The event analysed using the combined radar-optical method presented in chapter 5 was previously analysed by Dahlgren et al. (2011). In their analysis they compared the modelled electron densities, obtained by applying the method described in this section using the AIC, to observed electron densities. They found a good agreement between the modelled and observed electron densities whilst the auroral feature was in the radar beam, but at the times when the feature entered and exited the radar beam, there were drop-outs in the observed electron densities which were consistent with the convection of plasma through the radar beam. Without knowledge of the plasma surrounding the beam, or the flow velocity of the plasma, such effects cannot be corrected. Further, this event which is analysed by Dahlgren et al. (2011) and later in chapter 5 is the only application of the AIC method, and has not been tested with other events or compared, in detail, to other methods.

4.2 Southampton ion-chemistry model

Many auroral models have been used to study the effects of precipitation. These models can be split into two distinct types: those that attempt to solve the electron transport equation (Roble and Rees, 1977; Lummerzheim, 1987; Lummerzheim and Lilensten, 1994) and those that attempt to model the transport processes using Monte Carlo simulations (Sergienko and Ivanov, 1993; Solomon, 1993; Gattinger et al., 1996). A time-dependent, one dimensional auroral model is used in this work. This model is known as the Southampton ion-chemistry model and combines the electron transport method of Lummerzheim and Lilensten (1994) with the auroral model described in the appendix of Lanchester et al. (2001).

The effects of electron precipitation are calculated over the altitude range 75 - 500 km and over the energy range 0.05 eV - 70 keV. The altitude range of the model is selected such that interactions between precipitating electrons and the atmosphere are negligible above the upper limit and the scattering depth is large enough that electron transport is negligible below the lower limit. The model also assumes that the redistribution of

energy will always be to a lower energy. Therefore, an upper limit on the energy is the maximum energy of the precipitating electrons. The lower energy limit is defined as the energy boundary between the precipitating electrons and the ambient thermal population of electrons.

An electron energy spectrum is used as the energy input at the top of the model. This spectrum can have an assumed shape, such as a Maxwellian or Gaussian function, or be arbitrary, such as those obtained from satellite observation (Whiter et al., 2012). Spectra obtained from the inversion of radar data can also be used and several methods exist to obtain such spectra, such as those discussed in section 2.1.3. The densities of the major atmospheric neutrals and the corresponding elastic and inelastic collision cross-sections are also required. The neutral densities are obtained using the MSIS atmospheric model (Hedin, 1991), using the time and location of any supporting observations as input.

The electron transport component of the auroral model solves the electron transport equation to calculate the electron fluxes at all altitudes. The transport of electrons through a gas is described by:

$$\begin{aligned}\mu\frac{\partial}{\partial z}[I(E,z,\mu)] = &- B(E,z)I(E,z,\mu) \\ &+ n_e(z)\frac{\partial}{\partial E}[L(E)I(E,z,\mu)] \\ &+ C(E,z,\mu,I) \\ &+ Q(E,z,\mu,I)\end{aligned} \tag{4.9}$$

where the electron flux, $I(E,z,\mu)$, is in units of electrons $m^{-2}s^{-1}eV^{-1}$ (Lanchester and Gustavsson, 2012).

The first term on the right hand side describes collisional losses, which are due to inelastic collisions degrading the energy and elastic collisions changing the cosine pitch angle, μ, of the electrons. The cosine pitch angle is the cosine of the angle between the electron direction of motion and the magnetic field. The $B(E,z)$ term is given by:

$$B(E,z) = \sum_k n_k(z)\sigma_k^{tot}(E) \tag{4.10}$$

where $n_k(z)$ is the density of collisional species k and $\sigma_k^{tot}(E)$ is the collisional cross-sections for electrons interacting with species k. The $B(E,z)$ term describes the fraction of electrons lost at a given energy and altitude.

The second term describes the loss of energy to an ambient thermal population of electrons, $n_e(z)$, where $L(E)$ is the energy-dependent loss function. This loss function is empirically derived (Swartz et al., 1971) and is given by:

$$L(E) = \frac{3.37\times10^{-12}}{E^{0.94}n_e^{0.03}}\left(\frac{E-E_e}{E-0.53E_e}\right) \tag{4.11}$$

where $E_e = 8.618 \times 10^{-5} T_e$ and T_e is the electron temperature. Initial estimates of the electron temperature are obtained by assuming thermal equilibrium with the neutrals. The electron temperature then evolves with time in response to the input electron precipitation.

The third term describes elastic scattering of electrons into the cosine pitch angle and is given by:

$$C(E, z, \mu, I) = \sum_k n_k(z) \sigma_k^{el}(E) \int_{-1}^{1} p(E, \mu' \rightarrow \mu) I(E, z, \mu') d\mu' \tag{4.12}$$

where $\sum_k n_k(z)\sigma_k^{el}(E)$ is the total elastic collision frequency and $p(E, \mu' \rightarrow \mu)$ is the probability of an electron being scattered into the cosine pitch angle, μ, from some other cosine pitch angle, μ' (Lanchester and Gustavsson, 2012; Lanchester et al., 2001). Care must be taken in interpreting the first and third terms on the right-hand side of equation 4.9. These terms both treat the behaviour of elastic scattering, however the first term represents the losses of electrons at this E and μ to lower energies and into other cosine pitch angles, μ', whereas the third term represents the gain of electrons at this E and μ from higher energies and from other cosine pitch angles, μ'.

The fourth term describes all internal sources of electrons, which includes the energy degradation of the primary electrons due to collisions, production of secondary electrons due to ionisation and locally produced photoelectrons. This term is given by the following expression:

$$\begin{aligned} Q(E, z, \mu, I) \; &= Q_{photo}(E, z, \mu) \\ &+ \sum_k n_k(z) \sum_j \sigma_{kj}(\epsilon \rightarrow E) \int_{-1}^{1} p_{kj}(\epsilon, \mu' \rightarrow \mu) I(\epsilon, z, \mu') d\mu' \\ &+ \sum_k n_k(z) \int_{E+E^*}^{\infty} \sigma_{k,ion}(\epsilon \rightarrow E) \int_{-1}^{1} p_{k,ion}(\epsilon, \mu' \rightarrow \mu) I(\epsilon, z, \mu') d\mu' d\epsilon \end{aligned} \tag{4.13}$$

The first term on the right-hand side of equation 4.13 represents the production of photoelectrons; however as the events studied in this thesis are all from the nightside this term will be zero. The second term represents the gain of energy-degraded electrons of energy E and cosine pitch angle μ by inelastic collisions with neutral species k. Electrons of energy $\epsilon = E + \Delta E$ collide with species k exciting or ionising it into state j, with a collision cross-section of σ_{kj}. During the collision the electron loses energy ΔE, which is the excitation energy threshold of state j for species k or, in the case of energy degradation by ionisation, the sum of the ionisation energy of species k and the energy of the secondary electron. These collisions also redistribute the electron's cosine pitch angle, and the integral part of this term accounts for redistribution from $\mu' \rightarrow \mu$. The third term represents production of secondary electrons through the ionisation of neutral species k. The lower limit of the integral over energy ϵ in this term is $E + E^*$,

where E^* is the ionisation energy of species, as this is the minimum energy an electron requires to be able to ionise species k and have energy E after ionisation. The integral over the cosine pitch angle accounts for the production of secondary electrons into μ from ionisation caused by precipitating electrons with a cosine pitch angle of μ'.

The ion-chemistry component of the auroral model then solves the coupled continuity equations for all important positive ions and minor neutrals to calculate production rates of the excited and ionised states which produce the aurora. To analyse the emissions at wavelengths observed by ASK (section 3.1) production rates of O_2^+, specifically the first negative (1N) band system of O_2^+, and O^+ ions are required. Also required are production rates of the N_2 first positive (1PG) band system and the 3s ^{5}S excited state of atomic oxygen. The production rate profile of a species of interest, $q_i(z)$, by direct electron impact is given by:

$$q_i(z) = n_k(z) \int_0^\infty \sigma_{k,i}(E) I(E,z) dE \tag{4.14}$$

where $n_k(z)$ is the density profile of the parent species, $\sigma_{k,i}(E)$ is the cross section for production of species i from parent k and $I(E,z)$ is the energy dependent electron flux at altitude z.

Production rate profiles are used as source terms in the ion-chemistry continuity equations, which have the general form:

$$\frac{\partial}{\partial t}\rho_i(z,t) + \frac{\partial}{\partial z}\phi_i(z,t) = q_i(z,t) - L_i(z,t) \tag{4.15}$$

where $\rho_i(z,t)$ is the density profile of species i, $\phi_i(z,t)$ is the mass flux, $q_i(z,t)$ are the production rates, from direct electron impact as well as chemical sources, and $L_i(z,t)$ are the loss rates, emission and chemical losses. These equations can become coupled as the chemical production or loss rates of a given species can depend upon the presence of another.

Finally, the volume emission rate of an emission at wavelength λ is calculated by:

$$\eta_\lambda(z) = \frac{A_\lambda}{\sum_j A_j} \rho_i(z) \tag{4.16}$$

where A_λ is the Einstein co-efficient for the transition from state i which emits at the wavelength λ and $\sum_j A_j$ is the sum of Einstein co-efficients for all possible transitions from state i.

For the emissions observed by the ASK instrument, some simplifications can be made. Three of the observed emissions, 562.0 nm, 673.0 nm and 777.4 nm, are prompt. Therefore within the timestep of the model, the emission rate will be equal to the production rate. However, to obtain emission rates for the 732.0 nm emission, the continuity equation for $O^+(^2P)$ ions must be solved.

Emission rate profiles for the emissions observed by the ASK instrument are shown in Figure 4.1. These emission rates are for the event analysed in chapter 6 on 9 November 2006. The spectral shape of the input energy spectra is Gaussian and all input energy spectra have total energy fluxes of 1 mW m^{-2}. Emissions from the two molecular states are shown in the top two panels, with emission from the (1,0) band of the O_2^+ 1st positive band system on the left and emission from the (5,2) and (4,1) bands of the N_2 1st positive band system on the right. The shapes of the profiles are very similar, due to the scale heights of the parent N_2 and O_2 molecules being roughly the same, but display a marked difference in emission intensity. Emissions from the two atomic states are shown in the bottom two panels, with emission from the metastable $O^+(2P)$ ion on the left and emission from the 3s ^5S - 3p ^5P transition in atomic oxygen on the right. At low energies, the profile shapes of emission at 732.0 nm and 777.4 nm are similar because both are produced by electron impact on atomic oxygen. At high energies they are very different; emission rates for the 732.0 nm profiles are greatly reduced. This is because the more energetic an electron is, the lower the altitude the energy will be deposited at and at lower altitudes O^+ is strongly quenched, reducing the fraction of O^+ ions which decay radiatively.

The emission rate profiles are used to estimate the brightnesses of the emissions as they would appear when viewed in the magnetic zenith. The zenith brightnesses are obtained by integrating the emission rates with altitude:

$$B_\lambda = 10^{-10} \int_0^\infty \eta_\lambda(z) dz \tag{4.17}$$

where the factor of 10^{-10} is the conversion factor to Rayleighs as 1 Rayleigh = 10^{10} photons m^{-2} s^{-1}.

Some photons of the expected emission are not detected at the camera due to the filter transmittances and cut-offs. For each emission, the brightnesses are reduced by a filter factor, F_λ, such that:

$$B_\lambda^{ASK} = F_\lambda B_\lambda \tag{4.18}$$

where B_λ^{ASK} is the emission brightness as observed through the ASK filter for the wavelength λ.

The brightnesses of the emissions, as observed through the ASK filters, for different peak energies are shown in the top panel of Figure 4.2. The brightness of the 673.0 nm emission shows little variation, with a mean brightness of approximately 200 R across all energies. The brightness of the 562.0 nm emission, for energies above 1 keV, also shows little variation with energy, with a mean brightness of approximately 10 R across all energies. The lack of variation of brightness with energy allows the 673.0 nm emission, and to a lesser extent the 562.0 nm emission, to be used as a proxy for the energy flux

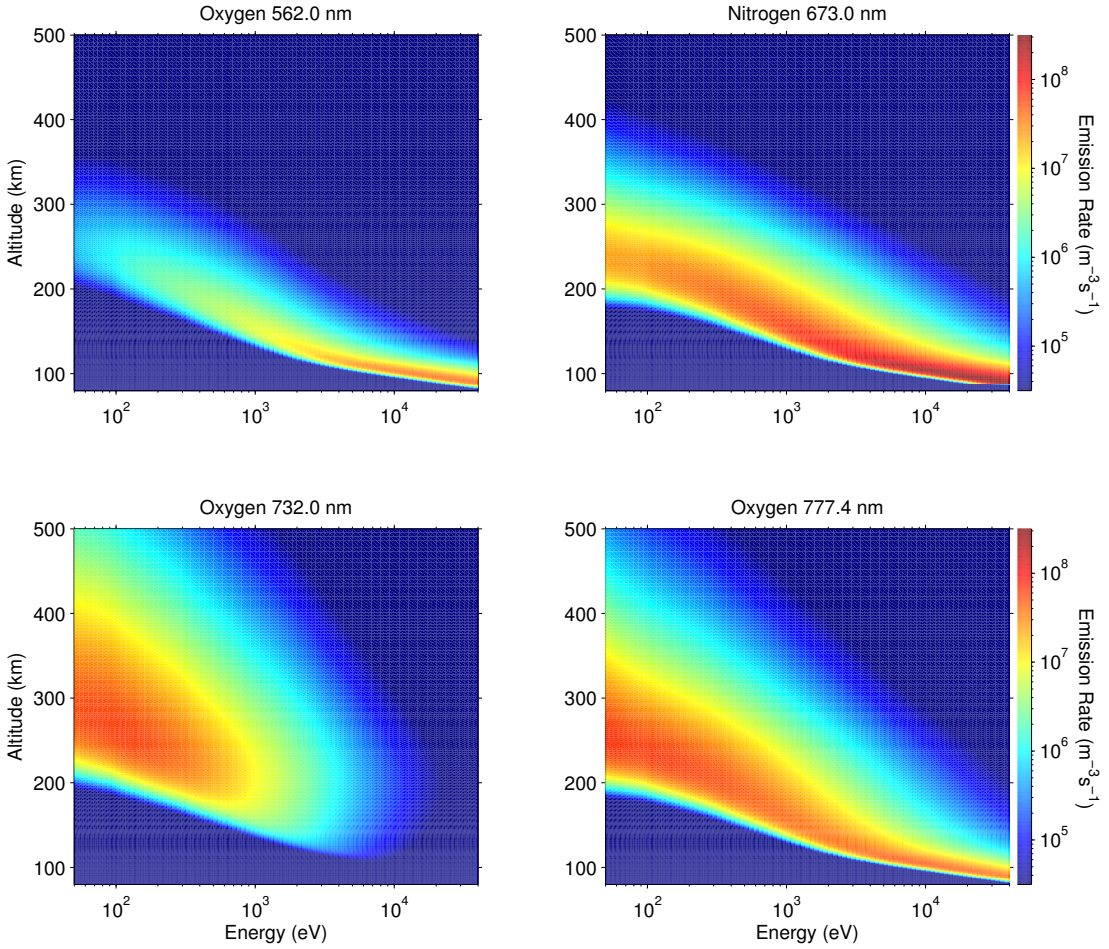

Figure 4.1: Emission rate profiles for O_2^+ at 562.0 nm (upper left), N_2 at 673.0 nm (upper right), O^+ at 732.0 nm (lower left) and O at 777.4 nm (lower right). The energy, altitude and emission rate axes are identical for all four plots.

of the precipitating electrons. The brightness of the 777.4 nm emission is sensitive to changes in energy, changing by an order of magnitude between 50 eV and 30 keV.

The ratio of brightnesses of specific auroral emissions has long been used as an estimator of the energy of the primary electrons. The bottom panel of Figure 4.2 shows the variation of brightness ratio with energy across a range of primary electron energies. The red line shows the ratio $B_{562.0}/B_{777.4}$ and the green line shows the ratio $B_{673.0}/B_{777.4}$. The two lines show that for each energy, there is a unique ratio of ASK emission brightnesses. The reverse is also true and this allows the ratio of emission brightnesses, obtained from images of the aurora taken using the ASK instrument, to be used to estimate the energy of the electron precipitation.

Uncertainties are present in the brightnesses estimated from the ion-chemistry model; these are estimated to be at least 35% (Whiter et al., 2010). The electron transport component of the ion-chemistry model has an uncertainty of at least 20%, which will be

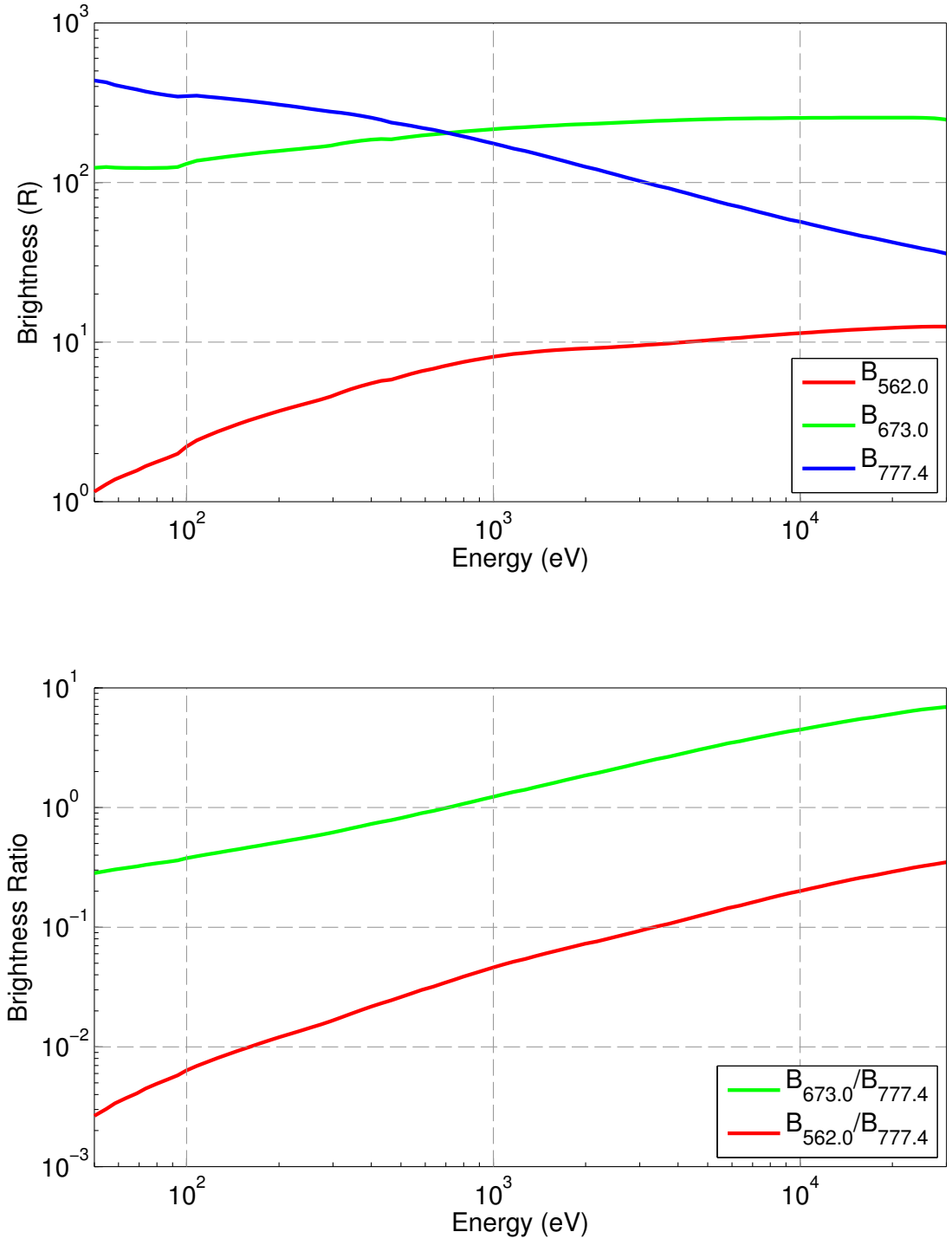

Figure 4.2: Top: Height integrated brightnesses of the emissions as observed through the ASK filters and in the magnetic zenith. Bottom: Brightness ratios of emissions observed by ASK.

increased if the atmospheric densities are not well known (Whiter et al., 2010). Further, the uncertainties in the cross-sections of the emissions observed by the ASK instrument are about 25% (Terrell et al., 2004; Julienne and Davis, 1976). The effect of variations in the oxygen density on the estimated energy of the primary electrons and modelled brightnesses of the 562.0 nm and 777.4 nm emissions was studied by Lanchester and Gustavsson (2012). For example, with an oxygen density of half the calculated MSIS value, the peak energy was found to increase by less than 5% for energies above 1keV.

4.3 Modelled auroral images

The work presented in chapters 5 and 6 models the spatio-temporal distribution and evolution of the auroral electron energy spectrum to determine the production rates of excited and ionised species that emit light which forms the aurora using the methods described in sections 4.1 and 4.2. The work then presented in chapter 7 uses modelled production rates for the long-lived $O^+(^2P)$ ion to model and track the dynamics and distribution of, and emission from, these ions to determine the ionospheric plasma velocities, and hence electric fields, surrounding fine scale aurora during times of electron precipitation. Validation of the recovered electron energy spectra, and their resulting production rates, is performed by comparing the observed images from the ASK instrument to intensity calibrated modelled images of the emission from the distributions of the excited neutrals or ions. Modelled images are also a key component of the method which determines the velocity of these ions, where modelled and observed images of the emission from the $O^+(^2P)$ ion at 732.0 nm are compared. Therefore, the methods by which the three-dimensional distributions of excited neutrals and ions, and the resulting auroral emissions, are produced needs discussion. These methods use the processes described in Rydesäter and Gustavsson (2001)

Distributions of excited neutrals and ions are modelled in a volume which fully encloses the horizontal extent of the ASK field of view, and spans the altitude range of significant auroral emission. This volume is segmented into a grid of cubic voxels. The grid of voxels has a uniform resolution, ds, in all directions and is oriented such that one axis of the grid is aligned with the direction of the magnetic field. Grid resolutions used in the work presented in this thesis are 200 m or 166 m, which correspond to 5 and 6 voxels per kilometre respectively. Each column of voxels is therefore aligned with the magnetic field, and can be thought of as a magnetic field line, allowing the 1-D production rates obtained from the Southampton ion-chemistry model to be placed along any given column, subject to interpolation between the resolutions of the ion-chemistry model and the grid. The direction of the magnetic field, within the ASK field of view and at auroral altitudes, is calculated using the International Geomagnetic Reference Field (IGRF) model. The orientation of the grid is determined using three basis unit vectors, one of which is the

magnetic field unit vector. The remaining two basis unit vectors are at right angles to both each other and the magnetic field unit vector.

Production rates at, and emission rates from, each voxel are modelled as 'blobs' which vary spatially as $\cos^2$. The blobs which model the rates have a maximum at the centre of the voxel and fall to zero at the centre of all orthogonally adjacent voxels. The blobs from adjacent voxels at the current voxel can therefore be thought to vary spatially as $\sin^2$, which, when combined with the $\cos^2$ spatial variation of the blob at the current voxel, yields a smooth distribution of production or emission if a uniform production or emission rate is present. The use of blobs which vary as $\cos^2$ presents an additional advantage in the fact that the $\cos^2$ blob appears the same no matter the direction it is viewed from. This invariance renders modelled observations of emission from the $\cos^2$ blobs invariant to the direction from which the blobs are observed. This invariance is not present for a uniformly emitting voxel, the centre of which would appear brighter if observed along a line of sight that passes through opposing vertices of the voxel than if the voxel were observed face-on along a line of sight which is parallel to the surface normal of one face of the voxel.

A reference position (r_0), which is the position of the bottom south-west vertex of the grid, is found. A uniform test image is projected along the pixel line of sights to the maximum altitude of the grid. The south-west-most position of the projected image is found and then traced down along the magnetic field to the minimum altitude of the grid to find r_0. A reference blob is positioned at r_0, and the positions of all other blobs are determined using r_0, the basis unit vectors and ds. Additionally, each blob is indexed using a set of indices; X, Y and Z along $\mathbf{e_1}$, $\mathbf{e_2}$ and $\mathbf{e_3}$ respectively. These indices are incremented or decremented when moving from one blob to the next along the basis unit vectors.

Before describing how the modelled volume is populated with production and emission rates, the method of producing a modelled image must first be described. Figure 4.3 illustrates the image modelling process. This figure shows two voxels, small and light grey boxes with circles at their centre, at different heights and horizontal positions within the modelled volume, which is the large grey box that contains the two voxels. The circles indicate the centres of the two voxels. The positions of the centres of the voxels within the modelled images is found by projecting along the pixel lines of sight, which are the thick black lines in the figure which connect the modelled volume, to the image plane on the ground, which is the combination of grids labelled 'Layer 0-2' in the figure. The pixel lines of sight are determined using the several key parameters of the ASK cameras, which are: the central pixels along the u and v image co-ordinates, the individual pixel field of view, the azimuth and elevation of the camera look direction, and the rotation of the camera about the camera look direction.

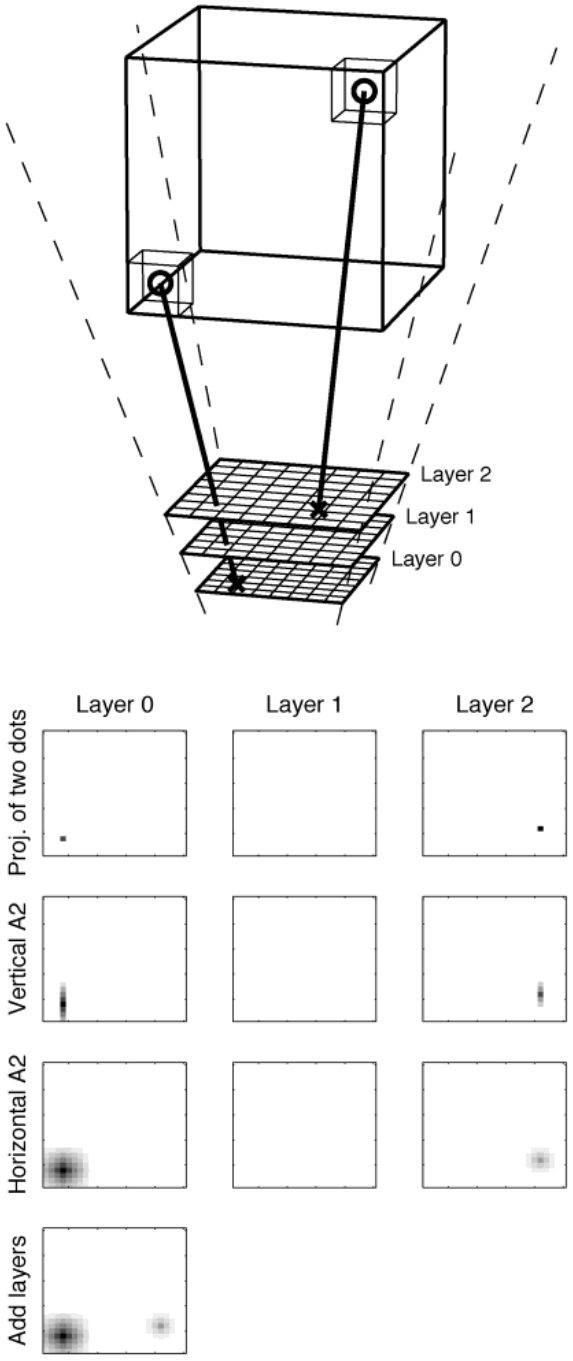

Figure 4.3: The top part of this figure shows the modelled volume. The spatial extend of the volume is delineated by the cuboid outlined by black lines. Two of the many voxels contained within this volume are shown using the light grey cuboids. The circles indicate the centres of the voxels. The grids below this volume, which are labelled 'Layer 0-2' indicate the plane of the modelled image on the ground. The solid black lines connecting the voxels and the image indicate the projection of the voxel from the modelled volume into the image. The images at the bottom illustrate how modelled images are formed by projections of the emission rates at each voxel. This figure is a reproduction of figure 1 from Rydesäter and Gustavsson (2001).

For the column of modelled images in figure 4.3 which are labelled 'Layer 0', the image labelled 'Proj. of two dots' shows a single point which is the position of the projection of the centre of the lower altitude voxel. This point is then convolved with the $\cos^2$ basis function both vertically and horizontally across the image to produce a modelled image, shown by the image labelled 'Horizontal A2' in the figure, of spatial extent across the image of the lower altitude voxel. This projection is then multiplied by the emission rate at the voxel to produce an image of emission from the voxel. The projection of the voxel at the higher altitude is shown in the column of images labelled 'Layer 2'. As this voxel is from a higher altitude, the effect of perspective will cause this voxel to appear smaller in the image than the voxel from the lower altitude. This perspective effect is dependent on the distance between the voxel and the image plane on the ground. This perspective effect is reproduced in the modelled image by using a $\cos^2$ basis function which has a smaller spatial extent. Voxels which have similar spatial extents in the modelled image are grouped together in the 'layers' and modelled in the image using the same basis function. The modelled image of the projection of the two voxels can be seen in the bottom-most image in the figure, which is labelled 'Add layers', and clearly shows the voxel at the lower altitude appears both larger and brighter. The projection of the many voxels from different altitudes into the image results in a very smooth modelled image of the emission from the volume.

However, these projected images are uncalibrated, which prevents a direct comparison of the brightness of the observed and modelled images. Calibration of the modelled images is achieved using the definition of the Rayleigh, which is the unit of surface brightness. A surface brightness of 1 Rayleigh (1 R) corresponds to a column emission rate of 10^{10} photons m^{-2} s^{-1} (Hunten et al., 1956). A modelled calibration image, which has a uniform surface brightness of 1 R, is produced by setting the emission rate along each field-aligned column of voxels in the volume to 10^{10} photons m^{-2} s^{-1} and then projecting this distribution of emission to the ground. Calibrated modelled images are then produced by dividing the uncalibrated images, formed by projection of the emission rates of a given emission at the modelled timestep, by the calibration image. The reductions in the brightness of the modelled images due to passing through the filters on the ASK instrument are already included in the modelling process of the emission rate profiles using equation 4.18.

Population of the modelled volume by production or emission rates is achieved by the reverse of the process described above for producing modelled images. A 'spectra map' is produced which contains estimates of the energy and energy flux at each pixel in the observed images using the methods described in section 4.2. These energies and fluxes are used to determine the electron energy spectrum, and hence the production rate profile that produces the observed image brightnesses. To populate the grid with production rates, the position of the altitude of peak production is needed. This position allows the grid column, or magnetic field line, along which the electrons precipitate, and

production occurs, to be found. The grid column could be found by locating the blob that minimises the Euclidean distance between the blob and the altitude of peak production, however this is slow computationally due to the large number of blobs within the grid. The process of finding the grid column can be sped up by simplifying the problem from three dimensions to two using the new method presented below.

Figure 4.4 shows a simplified vertical cross-section of the grid. The bottom-most plane of grid points forms a reference plane that allows the dimensionality of the problem to be reduced. Each pixel has a line of sight vector given by $\mathbf{e_p}$. $\mathbf{r_0}$ is the position vector from ASK to the reference position r_0, $\mathbf{r_p}$ is the position vector to the altitude of peak production of the production profile at that pixel and $\mathbf{r'_p}$ is the position vector to the point in the reference plane that lies along the same magnetic field line as the point given by $\mathbf{r_p}$.

The position vector $\mathbf{r_p}$ along $\mathbf{e_p}$ to the altitude of peak production (h) is given by:

$$\mathbf{r_p} = \mathbf{e_p}\frac{h}{e_p(3)} \tag{4.19}$$

where $e_p(3)$ is the component of $\mathbf{e_p}$ in the direction of the magnetic field.

The position vector between $\mathbf{r_0}$ and $\mathbf{r'_p}$ lies within the reference plane, therefore all points within the reference plane obey the following equation:

$$\mathbf{e_3} \cdot (\mathbf{r_0} - \mathbf{r'_p}) = 0 \tag{4.20}$$

Additionally, we can express $\mathbf{r'_p}$ in terms of the displacement (dl) along $\mathbf{e_3}$ from $\mathbf{r_p}$ as:

$$\mathbf{r'_p} = \mathbf{r_p} + dl\mathbf{e_3} \tag{4.21}$$

By combining equations 4.20 and 4.21 and re-arranging the following expression for dl is obtained:

$$dl = \mathbf{e_3} \cdot (\mathbf{r_0} - \mathbf{r_p}) \tag{4.22}$$

Finally, using equations 4.21 and 4.22, $\mathbf{r'_p}$ is then defined only in terms of known or easily calculated quantities:

$$\mathbf{r'_p} = \mathbf{r_p} + \mathbf{e_3} \cdot (\mathbf{r_0} - \mathbf{r_p}) \tag{4.23}$$

Equation 4.23 allows the position of the projection of the altitude of peak production to the reference plane to be found. The grid column is then found by minimising the distance between the position of the projection and each blob in the reference plane.

However, it is not enough to find only the column along which the production occurs. The $\cos^2$ function shape of each blob means that, in addition to a contribution to the production rate along the central column found above, there will be contributions to

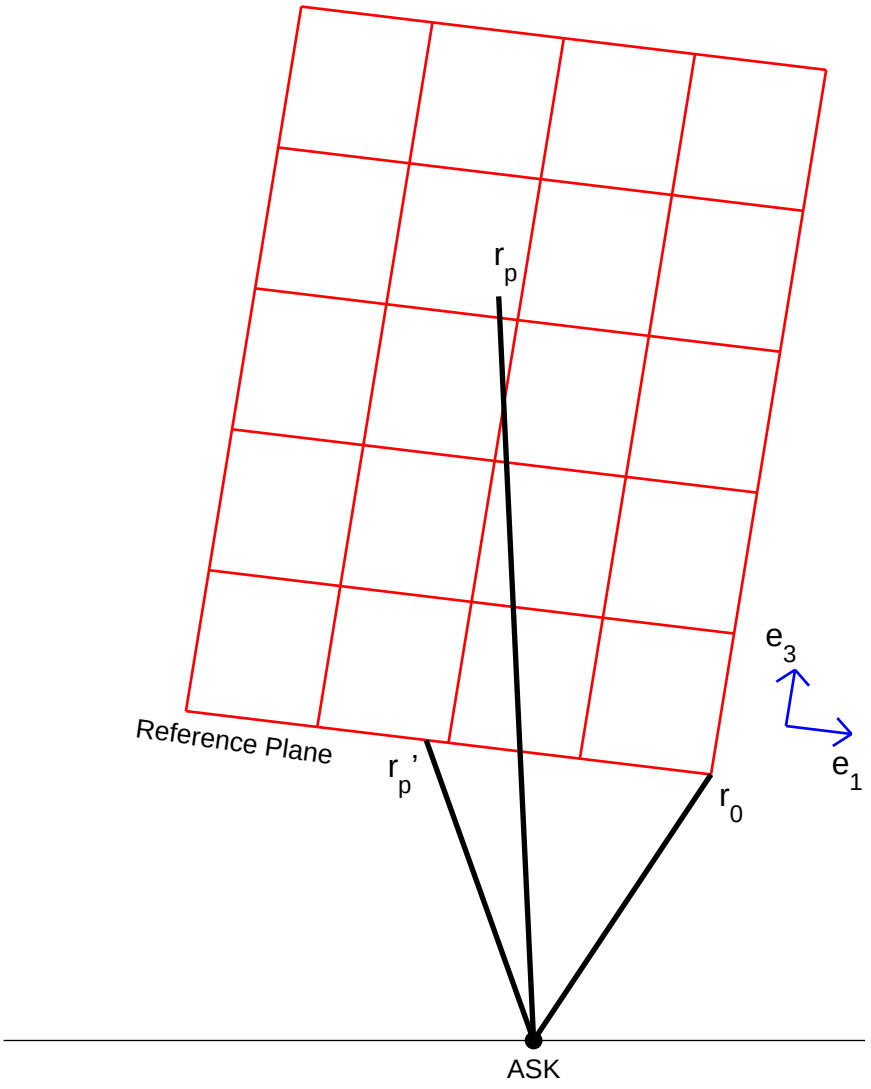

Figure 4.4: Simplified vertical cross-section through the 3-D grid for production.

three of the eight columns that surround the central column. These extra columns, and the contributions of the production rate profile to each of the columns must now be found.

The position vector $\mathbf{r''_p}$ from $\mathbf{r_0}$ to $\mathbf{r'_p}$ is:

$$\mathbf{r''_p} = \mathbf{r'_p} - \mathbf{r_0} = [r''_{p_{e_1}}, r''_{p_{e_2}}, 0] \tag{4.24}$$

where $r''_{p_{e_n}}$ are the components of $\mathbf{r''_p}$ along the basis vectors $\mathbf{e_n}$. The distances b_n, in fractions of a blob, along $\mathbf{e_n}$ from the centre of the column of blobs to $\mathbf{r'_p}$ are given by:

$$b_n = \frac{r''_{p_{e_n}}}{ds} - \mathsf{round}\left(\frac{r''_{p_{e_n}}}{ds}\right) \tag{4.25}$$

where round is the rounding function. The resulting fractional blob distances are in the range $-0.5 \leq b_n < 0.5$. The signs of b_1 and b_2 are used to determine which columns of blobs receive contributions to production rates. If the sign is positive, then one is added to the column subscript and if the sign is negative, then one is subtracted from the column subscript. For example, if b_1 is positive and b_2 is negative, then only columns with the indices $[X, Y]$, $[X+1, Y]$, $[X, Y-1]$, and $[X+1, Y-1]$ would receive contributions to the production rate.

The fractional contribution, $C(X, Y)$, of the production rate to the central blob is given by the product of the fractional blob amplitudes, c_X and c_Y, at $\mathbf{r'_p}$:

$$C(X, Y) = c_X c_Y \tag{4.26}$$

where c_X and c_Y are given by:

$$c_X = cos^2\left(\frac{\pi}{2} b_1\right) \tag{4.27}$$

$$c_Y = cos^2\left(\frac{\pi}{2} b_2\right) \tag{4.28}$$

The blobs are arranged such that, if the maximum amplitude of each blob were one, the sum of the fractional blob amplitudes at any given point would also be equal to one. The fractional blob amplitudes of blobs that also receive contributions can be calculated simply as:

$$c_X(X \pm 1) = 1 - c_X \tag{4.29}$$

$$c_Y(Y \pm 1) = 1 - c_Y \tag{4.30}$$

Taking the example given above, of $b_1 > 0$ and $b_2 < 0$, the contribution of the production rate profile to the columns of blobs surrounding the column at $[X, Y]$ would be given

by:

$$C(X+1,Y) = (1-c_X)c_Y \tag{4.31}$$

$$C(X,Y-1) = c_X(1-c_Y) \tag{4.32}$$

$$C(X+1,Y-1) = (1-c_X)(1-c_Y) \tag{4.33}$$

Finally, a look-up table is produced that, for each pixel in the spectra map, contains the indices of the columns which receive contributions and the fraction of the production rate that is contributed to each column. A separate look-up table is produced for each production rate that is modelled.

Because the spatial resolution of the spectra map is greater than the spatial resolution of the 3-D grid, the production rate along any given column within the grid will be the mean of the production rate profiles that contribute to it.

Chapter 5

Combined radar and optical modelling of the aurora

5.1 Introduction

This chapter describes a novel method to model the evolution of auroral electron energy spectra in a region surrounding the magnetic zenith at sub-kilometre and sub-second spatial and temporal resolution. Estimates of the auroral electron energy spectrum, characteristic energy and energy flux are derived from optical and radar observations using established methods. The characteristic energy here specifically refers to the peak energy, which is the energy at which the electron flux is the largest. Radar observations of electron density are used to estimate the energy spectrum, using the inversion method, and optical observations of auroral brightness are used to estimate the energy and flux, using the ratio method. However, these methods are limited in their application when observations are not made in the direction of the magnetic zenith. The novel method described in this chapter is used to extend the applicability of the established methods to regions surrounding the zenith. This method utilises the simultaneous radar and optical observations to characterise each radar estimate of the energy spectrum with an optical estimate of the energy and flux. This allows estimates of the energy spectrum to be extrapolated out of the magnetic zenith to a region that is covered by the field of view of ASK. Finally, modelled images of the auroral emissions are produced and are compared to observed images of the aurora to verify the estimated energy spectra.

5.2 Instrumentation

Data from both the ASK instrument and the EISCAT mainland radar at Tromsø were used in this work. The ASK instrument was co-located with the radar and was used to

obtain images of the aurora. The instrument was operated at a framerate of 32 Hz and the filters in use at this time were those with passbands centred at 562.0 nm, 732.0 nm and 777.4 nm. These filters select emission from the (1,0) band of the O_2^+ 1st Negative band system, the metastable $O^+(^2P)$ ion and the 3s ^5S - 3p ^5P transition in atomic oxygen respectively.

The EISCAT Tromsø radar was used to measure ionospheric electron densities at auroral altitudes along the magnetic zenith. The radar experiment 'arc1' was used. The measured power spectra were analysed using GUISDAP to obtain electron densities at 0.44 s resolution.

5.3 Event on 12 December 2006

The event analysed here was captured shortly after the sub-storm onset, which occurred at approximately 19:20 UT with a Kp index of 3. A bright and dynamic auroral arc was observed in the magnetic zenith above Ramfjordmoen near Tromsø, Norway shortly after 19:32 UT. Figure 5.1 shows the evolution of the arc, at 0.5 second intervals, observed through the ASK3 filter. The radar field of view is shown by a black circle. The arc first enters the radar field of view at 2.5 seconds after 19:32 UT and finally exits the radar field of view at 8.5 seconds after 19:32 UT. Prior to the appearance of the bright arc there are both diffuse aurora and some low intensity structured aurora present in the images. The bright arc of interest is orientated in a north-south direction. Counter-streaming regions of emissions are present on both sides of the arc which have been interpreted as evidence of shear motion (Dahlgren et al., 2011).

5.4 Method and Results

The radar data and results from the inversion model are presented in section 5.4.1. Section 5.4.2 presents the optical data and the results of applying the ratio method to determine the energy and energy flux. Section 5.4.3 covers the novel method of combining the radar and optical data and the resulting energy spectra. Finally, the accuracy of the method is examined in section 5.4.4 by comparing images of the modelled auroral brightness, which are due to the spectra obtained in section 5.4.3, to images of the observed auroral brightness.

5.4.1 Radar estimation of energy and flux

The electron density measurements for the duration of the event are shown in Figure 5.2. The profiles show an enhancement in electron density at altitudes from 105 to 140 km,

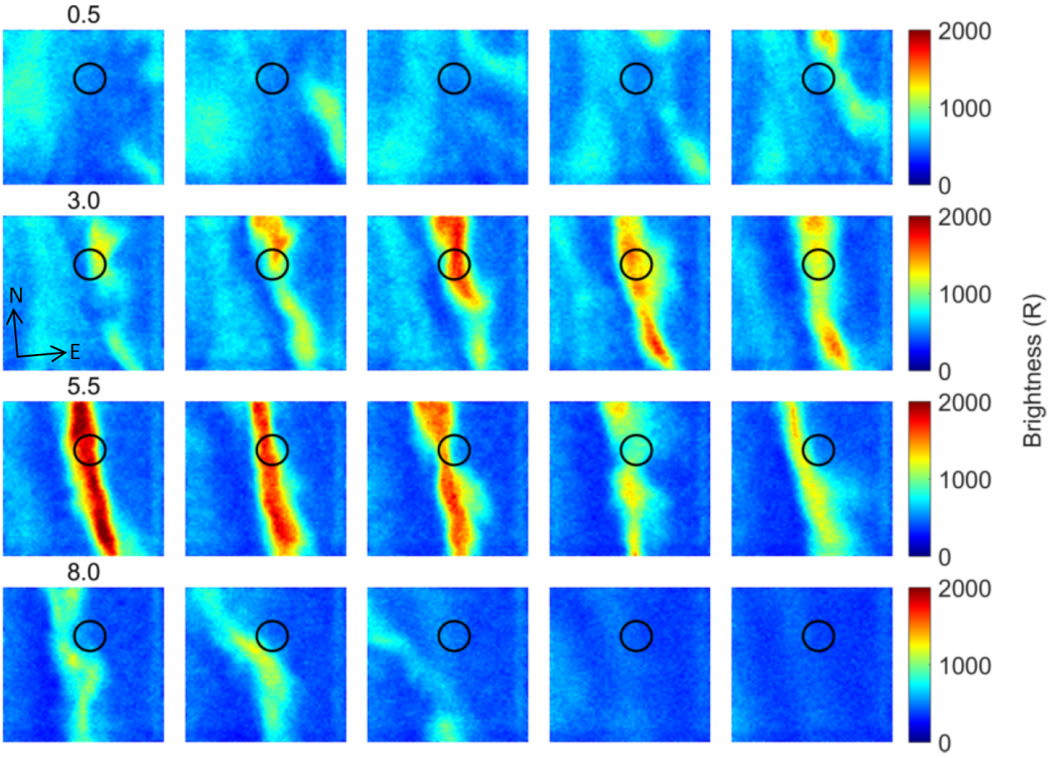

Figure 5.1: Images of the 777.4 nm emission at 0.5 second intervals starting at 0.5 seconds after 19:32 UT. The number of seconds after 19:32 UT are displayed above the first image in each row. The field of view covers an area about 5 km by 5 km at 100 km altitude. The black circles indicate the radar beam position at 100 km.

starting approximately 3 seconds after 19:32 UT. This enhancement corresponds to the brightening and movement of the arc across the ASK field of view and into the radar field of view. This enhancement lasts for 5 seconds after which the arc moves out of the radar field of view and fades. The electron density profile between 100 and 180 km at 5.3 seconds after 19:32 UT is shown in Figure 5.3.

The measurements of electron density are used as input to an inversion method that uses the Akaike information criterion and is described in section 4.1. Electron density profiles are obtained by integrating the electron density continuity equation using estimated electron energy spectra. The best-fit energy spectrum is obtained by minimising the weighted least square difference between the modelled and measured electron density profiles. In the least square minimization the residuals are weighted by the standard deviation of the electron density measurements. The fitting also includes a term which penalises increasing complexity to prevent the modelled energy spectrum from fitting to noise present in the electron density measurements. This method determines the best-fitting spectrum without making any assumptions about the shape of the spectrum.

The derived energy spectra are shown in the top panel of Figure 5.4. At 3 seconds after 19:32 UT, a strong enhancement in electron fluxes at energies between 2 and

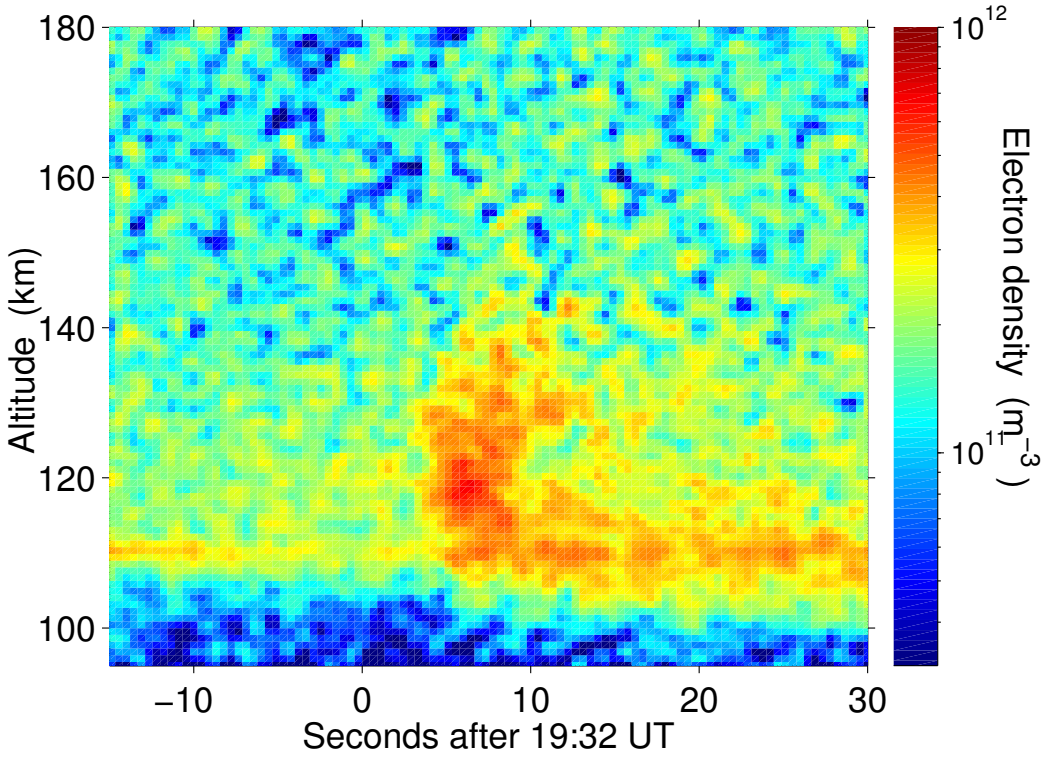

Figure 5.2: Electron density profiles measured by the EISCAT UHF radar.

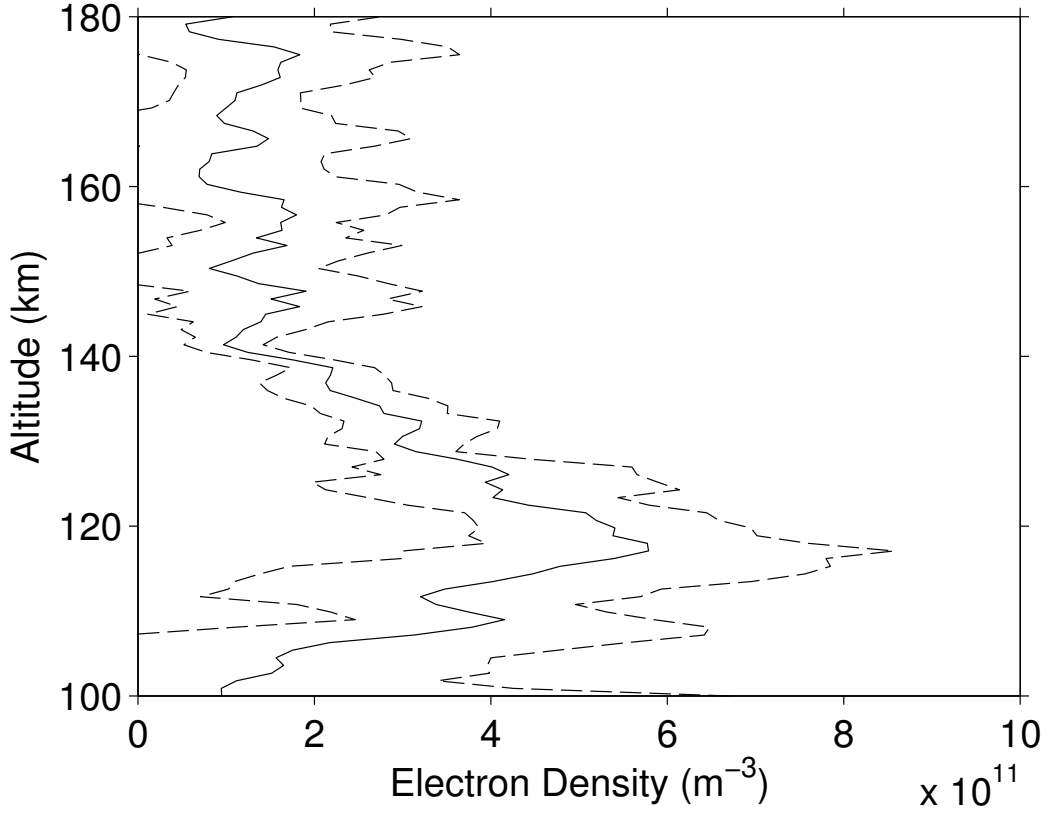

Figure 5.3: The electron density profile measured at 5.28 seconds after 19:32 UT. The solid line indicates the measured electron density. The dashed lines indicate the upper and lower bounds on the uncertainty of the measurement.

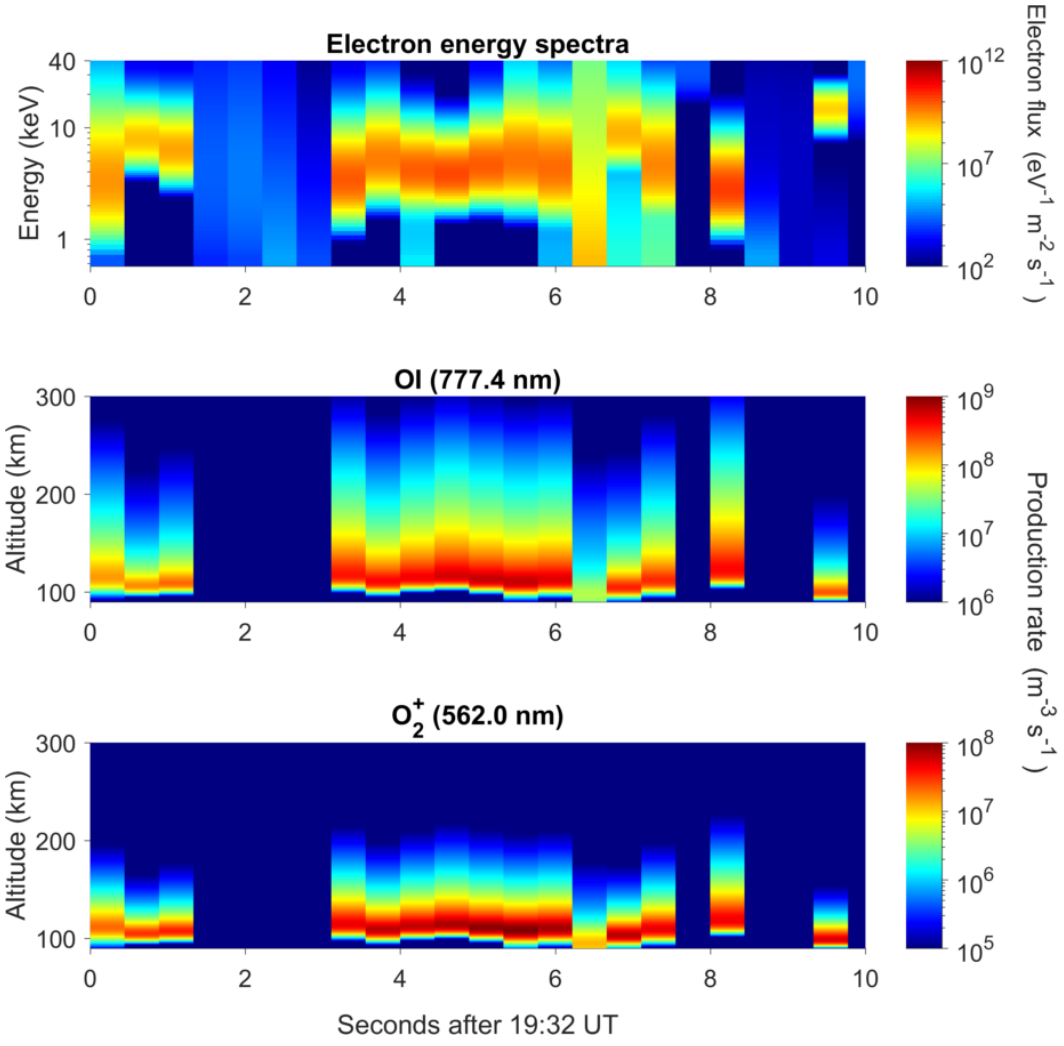

Figure 5.4: Top: Derived electron energy spectra for the 19:32 UT arc. Middle: Modelled production rate profiles for the 777.4 nm emission. Bottom: Modelled production rate profiles for the 562.0 nm emission.

8 keV is seen, corresponding to the arc moving into the radar field of view. The energy rapidly increases from 2 keV to about 5 keV and remains at 5 keV when the arc is in the radar field of view. The flux enhancements cease at 8 seconds after 19:32 UT, corresponding to the arc moving out of the radar field of view. There are some flux enhancements present at times when the arc is outside the radar field of view, such as those between 0 and 1.3 seconds after 19:32 UT, but there is no corresponding optical signature. These enhancements in the energy spectrum are due to either faint diffuse back-ground precipitation or the presence of a sporadic E-layer, which can be seen in Figure 5.2 at 110 km.

The energy spectra are used as input to the Southampton ion-chemistry model, which solves the time-dependent continuity equations for all major positive ions and minor neutral species (Lummerzheim and Lilensten, 1994; Lanchester et al., 2001). Initial conditions specific to the position and time of the event are used, including estimates

of the neutral atmosphere from the MSIS model (Hedin, 1991), the A_p index and F10.7 solar radio flux. Cross-sections for the emissions of interest are from Terrell et al. (2004) for the 562.0 nm emission and Julienne and Davis (1976) for the 777.4 nm emission.

The middle and bottom panels of Figure 5.4 show the production rate profiles for the 777.4 nm emission from atomic oxygen and the 562.0 nm emission from O_2^+ respectively. The O_2^+ profiles show high production rates at altitudes between 100 and 150 km, with the altitude of peak production varying between 105 and 115 km when the arc is in the field of view. In contrast, the production rate profiles for the 777.4 nm emission span an extended altitude range. High production rates are found between 100 and 250 km and the profiles have a higher altitude of peak production, which varies between 115 and 130 km.

5.4.2 Optical estimation of energy and flux

Energy and energy flux estimates of the electron energy spectra are obtained from multi-monochromatic observations of the aurora. The ratio of brightnesses of auroral emissions observed by the ASK instrument has been used to estimate the characteristic energy and energy flux of auroral electron precipitation (Lanchester et al., 2009; Dahlgren et al., 2011). In this work the ratio of the brightness of the 562.0 nm emission to the 777.4 nm emission is used to estimate the characteristic energy of the electron precipitation. The brightness ratio can be used because of the different sensitivities to electron energy of the two emissions.

The variation of the brightness ratio with the characteristic electron energy has been modelled using the Southampton auroral model. The model is run using monoenergetic energy spectra that have a fixed energy flux but varying peak energy to obtain production rate profiles for both the 562.0 nm and 777.4 nm emissions. Because both emissions are prompt, the emission rate profiles are identical to the production rate profiles. The emission brightnesses are calculated by height integration of the production rate profiles. The variation of emission brightness with energy is shown for both emissions in the top panel of Figure 5.5. The brightness ratio, $B_{562.0}/B_{777.4}$, is calculated for each energy to produce a look-up table as illustrated in the bottom panel of Figure 5.5.

The brightness of the 562.0 nm emission, $B_{562.0}$, is used to estimate the energy flux of the precipitation. The modelled $B_{562.0}$ is the blue line in the top panel of Figure 5.5. For energies greater than about 1 keV, the emission brightness is roughly constant at 10 R/mW/m^2. This factor is used to convert the 562.0 nm emission brightness to energy flux.

Before estimating the energy and energy fluxes, the ASK images are filtered both spatially and temporally, from a frame rate of 32 Hz to 8 Hz, to remove stars and reduce the effects of noise. The brightnesses are calculated by averaging over the radar field of

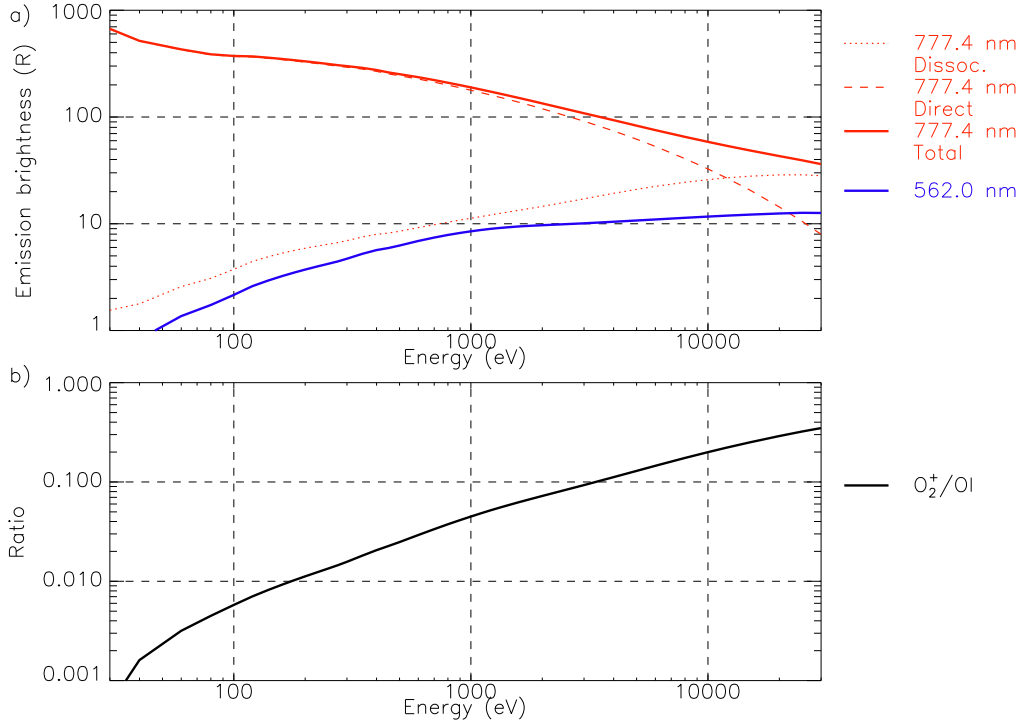

Figure 5.5: Top: Modelled ASK brightnesses against characteristic energy. Bottom: Calculated brightness ratio against characteristic energy.

view within the ASK field of view and converting from the ASK frame rate to the radar data rate.

5.4.3 Combined radar and optical method

The processes described in sections 5.4.1 and 5.4.2 produce the energy spectrum and auroral brightness only in the magnetic zenith. To extend this method to three dimensions and obtain the energy spectrum of the electron precipitation in a region surrounding the magnetic zenith a further look-up table is used. This look-up table characterises each energy spectrum, as estimated from the radar data, with an optical estimate of the energy and energy flux.

The optical estimates of the energy and energy flux are presented in Figure 5.6. The coloured line, whose colour variation indicates time, shows how the optical energy and energy flux vary throughout the event. The numbered circles indicate the time, in seconds, after 19:32 UT when energies and fluxes are calculated. As the arc enters the radar field of view, marked 'IN', the optical estimates of the flux increase greatly and the energy falls slightly. When the arc is in the radar field of view the flux estimates remain elevated and there is little variation in energy. After the arc leaves the radar field of view, marked 'OUT', the flux falls and the energy rises as the radar samples a region of diffuse aurora. The times are used to connect in-beam optical energy and flux

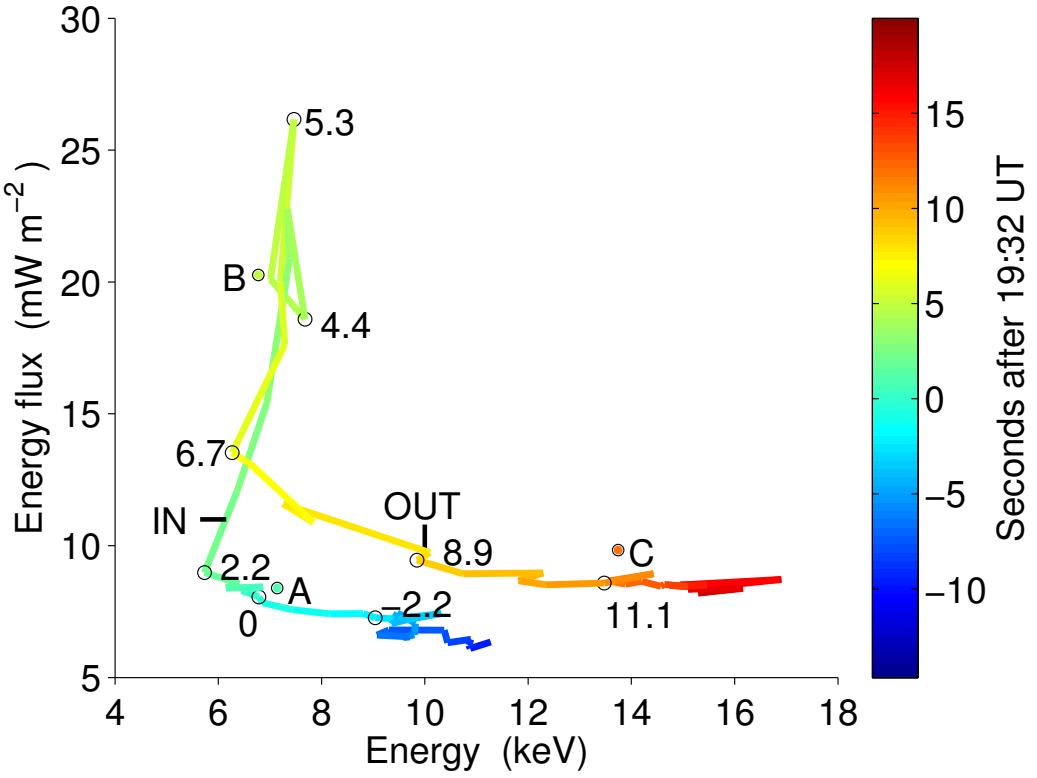

Figure 5.6: The optical energy and flux estimates used to characterise the electron energy spectra. The coloured line and numbered circles indicate the time of a radar measurement. The circles labelled A, B and C are the energy and flux estimates at three selected pixels.

estimates with the ISR-estimated electron spectra, producing an optics-radar look-up table.

Estimates of the energy spectrum across the ASK field of view are obtained using this second look-up table. All energy and flux estimates are normalised to the minimum and maximum values of the optical energy and flux estimates obtained inside the radar field of view throughout the event. The normalisation gives equal weighting to the energy and energy flux when finding the energy spectrum mostly likely to produce the intensities observed at that pixel. The matching process assumes that the atmospheric and geomagnetic parameters do not vary significantly throughout the event.

This process is illustrated at the points A, B and C in Figure 5.6 which correspond to the circled pixels, from left to right, in Figure 5.7. Pixel A comes from a region before the arc is seen in the radar and has energy and flux estimates of 7.1 keV and 8.4 mWm^{-2} respectively. The pixel A energy and flux estimates are compared to the energies and fluxes that characterise each energy spectrum to determine the energy spectrum causing the observed brightness. At pixel A, the energies and fluxes are most similar to those that characterise the energy spectrum estimated at 0.9 seconds after 19:32 UT. Using the

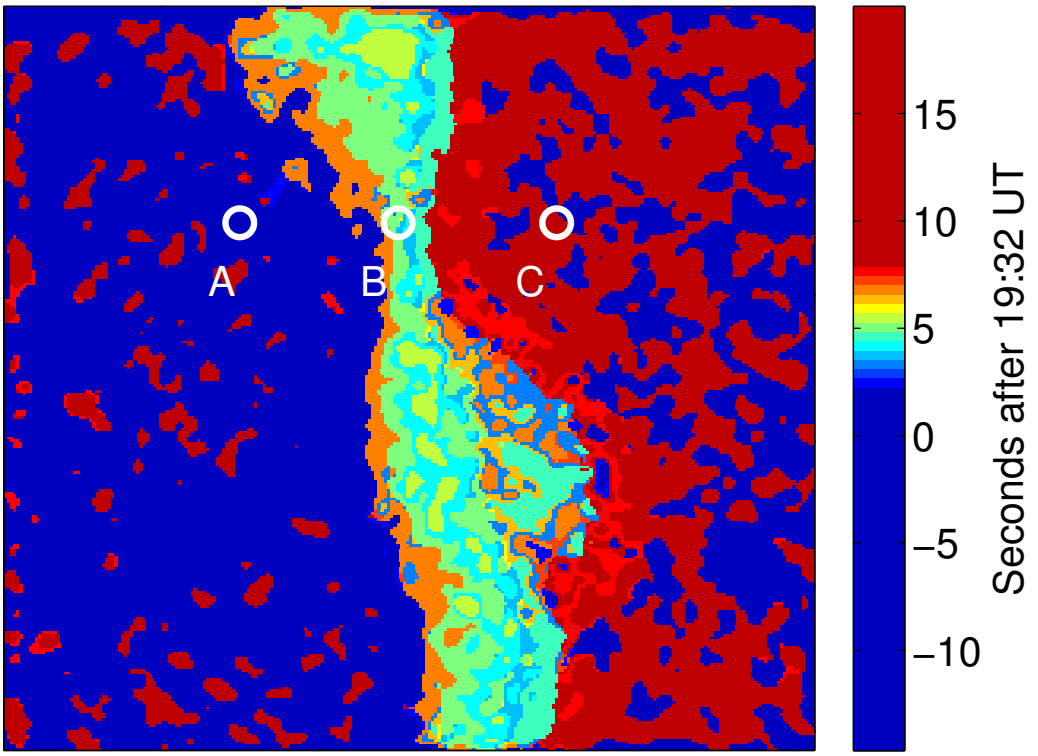

Figure 5.7: Estimate of the closest matching energy spectrum for each pixel in the ASK images at 6.5 seconds after 19:32 UT. The colour indicates the time when the matching spectrum was obtained. The pixels labelled A, B and C here correspond to the energies and fluxes labelled A, B and C in Figure 5.6.

same process, the spectra for pixels B and C are those measured at 4.9 and 12 seconds after 19:32 UT respectively.

A map of the most likely spectrum is produced by performing the matching process for each pixel in the image. Figure 5.7 shows the map at 6.5 seconds after 19:32 UT; the colour indicates the time that the closest matching energy spectrum was present in the radar. Pixels in regions of the image before the arc has passed (left side of map) are matched to energy spectra measured at a time before the arc passes into view of the radar, similarly for pixels covering the regions of the arc itself (centre of map) and regions after the arc has passed (right side of map). There are some pixels which are cross-matched, matching spectra obtained before the arc has passed to pixels in regions after the arc has passed, but no spectra calculated when the arc is in view of the radar are matched to pixels that are not part of the arc. The energy flux of the spectrum matched to each pixel is scaled to the optical flux at that pixel.

5.4.4 Image Modelling

The 2-D spectra maps are used to estimate the 3-D emission rates, from which modelled images of the auroral emission are subsequently obtained. A 3-D grid that fully encloses the horizontal extent of the ASK field of view and spans the altitude range of significant auroral emission is used. The production rate profiles in Figure 5.4 show that the grid should cover the altitude range 90 - 300 km, leading to a horizontal size of 30 km by 30 km to ensure the entire ASK field of view is within the grid at these altitudes. The grid has a resolution of 200 m and has one axis aligned with the magnetic field, which is assumed to be in a fixed direction over the altitude range of the grid.

A reverse projection method is used to populate the grid with the production rates. The production rate profile at each pixel is projected along the pixel line of sight to the altitude of peak production to determine the horizontal position of the grid column, or magnetic field line, along which the electrons travel and the production occurs. The resolution and size of the grid result in multiple pixels projecting to the same grid column. The production rate profiles along any grid column will therefore be an average of all the contributing profiles, weighted by the contribution of each pixel to that grid column.

Some columns in the grid are not populated by this method, leaving regions of the grid with no production because the altitude of peak production ranges between 100 and 130 km, whereas the grid extends to 300 km. The ASK field of view covers a larger horizontal extent at higher altitudes, so some of the regions with no production will be visible in the modelled images. Therefore the auroral brightness is lower than expected around the edges of the modelled image. To reduce this effect the production rates are extrapolated into the unpopulated regions of the grid. A quiet border of zero production is used to ensure the extrapolated production rates are sensibly bound.

Modelled images of the aurora are formed by projecting the production rates, which are equal to the emission rates, to an image plane on the ground using the blob-based dot projection method of Rydesäter and Gustavsson (2001). A modelled calibration image of a uniform 1 Rayleigh emission brightness is used to convert the modelled images to Rayleighs. The calibration image is produced by setting the emission rate along each column in the grid to 10^{10} photons $m^{-2}s^{-1}$ and projecting to the image plane on the ground. The brightness, in Rayleighs, of the modelled image is calculated by dividing the value at each pixel in the modelled image by the value of the pixel in the calibration image. The reduction in brightness of the modelled emission due to the passband and transmittance of the ASK filters is taken into account. The modelled brightnesses are multiplied by a factor of 0.063 for the 562.0 nm emission and by 0.70 for the 777.4 nm emission.

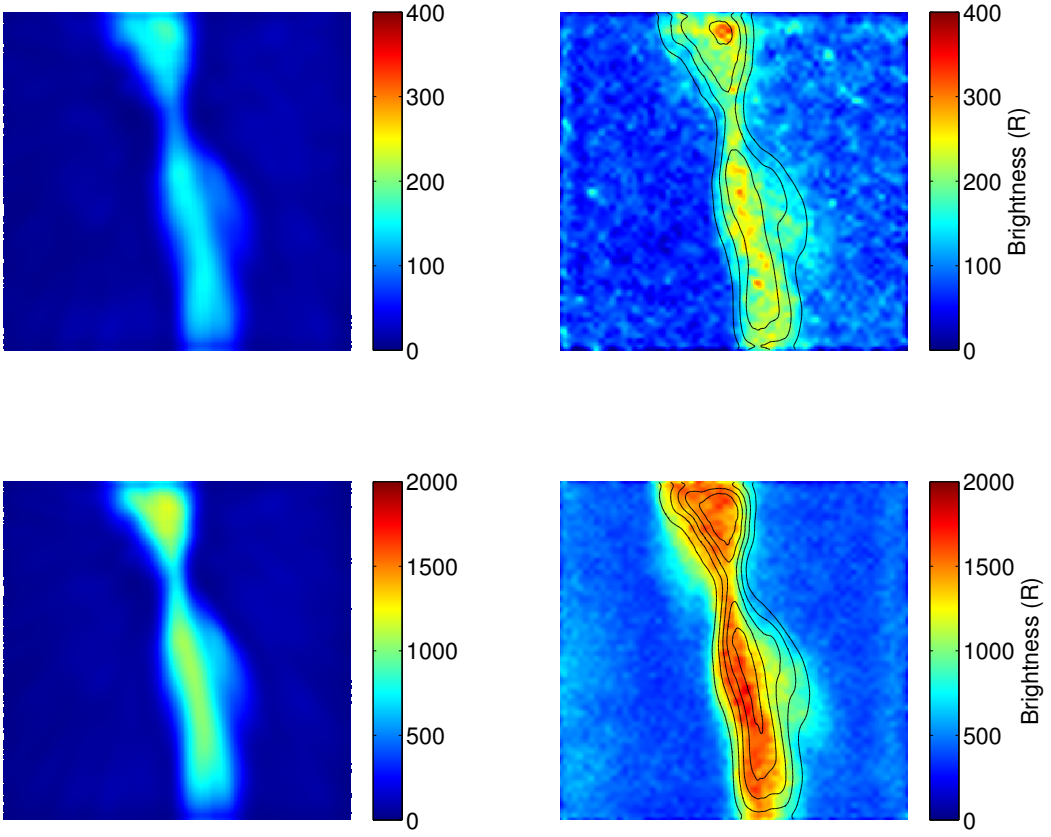

Figure 5.8: Modelled (left) and measured (right) images of the 562.0 nm (top) and 777.4 nm (bottom) emission brightnesses at 6.5 seconds after 19:32 UT. The black curves on the observed images are brightness contours of the modelled images at intervals of 40 R and 200 R for the 562.0 nm and 777.4 nm emissions respectively.

Figure 5.8 shows the modelled (left) and observed (right) images of the 562.0 nm (top) and 777.4 nm (bottom) emission brightnesses at 6.5 seconds after 19:32 UT. The black lines are contours of brightness for the modelled images. The shape and structure of the arc is reproduced but the brightnesses are underestimated by about 30% in the central part of the arc and by up to 50% along the edges of the arc.

5.5 Discussion

In the absence of measurements of electron energy spectra outside the radar field of view, the purpose of the image modelling is to verify the estimated energy spectra in the region outside the magnetic zenith. The modelled images, at both emission wavelengths, reproduce the observed aurora. The brightness structure is well modelled even reproducing the dynamic sheared motions along the arc as it crosses the zenith.

The underestimation of the brightness is likely caused by the sampling of the arc by the radar. At no time does the arc uniformly fill the field of view of the radar. At times

the radar is sampling both the arc and the region in the vicinity of the arc where the flux is lower. This would cause the measured electron density to be lower than if the arc completely filled the radar field of view. An underestimate of the electron density would lead the inversion model to underestimate the energy flux of the energy spectrum. This effect is greater when the arc is at the edge than when it is in the centre of the radar field of view.

The uncertainty in absolute brightness is estimated from the spread of calibration values, each value obtained by calibrating to a single star in the ASK field of view using the Pulkovo stellar catalogue. This uncertainty is estimated by Whiter et al. (2010) to be 20%. The main additional uncertainty in the present data is the lack of clear sky, free of aurora, close in time to the event. Such a measurement is used for the level of background brightness. In the present case, an estimate of the background is obtained from a clear sky period, with no aurora present, about 10 minutes before the event. In the absence of any cloud in the data we estimate an extra uncertainty of 10% due to changes in the background light levels in the 10 minutes between the background estimate and the event.

Uncertainties are also present in the brightnesses from the ion-chemistry model; these are estimated to be at least 35% (Whiter et al., 2010). The electron transport component of the ion-chemistry model has uncertainties of at least 20%, which will be increased if the atmospheric densities are not well known. Uncertainties in the cross-sections for the species of interest are about 25% (Terrell et al., 2004).

The effect of variations in the oxygen density on the estimated energy of the primary electrons and modelled brightnesses of the 562.0 nm and 777.4 nm emissions was studied by Lanchester and Gustavsson (2012). For example, with an oxygen density of half the calculated MSIS value, the peak energy was found to increase by less than 5% for energies above 1 keV.

Electron density measurements at altitudes between 90 and 150 km are required to estimate the auroral electron energy spectrum. These measurements must be made at sub-second temporal resolution, to capture the dynamics of the electron precipitation, and at a high spatial resolution, ideally less than 1 km range resolution. Therefore, the application of this method is primarily limited by the availability of and resolution requirements on the radar data. Amplification of noise, which enters through the time derivative of the electron density, is avoided by not calculating the ionisation rate profile from inversion of the electron continuity equation. Instead, smooth estimated electron spectra produce smooth ionisation rate profiles from which the electron densities are calculated. By this method noise damping is achieved as only the altitude averaged noise propagates to the estimated electron energy spectra.

A complete catalogue of energy spectra is necessary for the matching process. Energy spectra, and hence electron density measurements, are needed from before, during and

after the passage of an auroral feature across the radar field of view. Each feature analysed using this process requires such a catalogue of energy spectra in order to prevent cross-matching of energy spectra between features. For the event studied here, the catalogue of spectra is complete and there is only one auroral feature present in the data. Further the matching of appropriate electron spectra to appropriate regions of the image, as illustrated in Figure 5.7, indicates that the method is robust in the matching.

5.6 Conclusions

A new method to determine the structuring and dynamics of the auroral electron precipitation in an extended region surrounding the magnetic zenith is presented. Radar estimates of the energy spectra are combined with optical estimates of energy and energy flux to extrapolate out of the radar beam and provide an estimate of the energy spectrum across the ASK instrument field of view. Such a method is only applicable in the region surrounding the magnetic zenith and is only suitable because the ASK field of view is narrow enough to eliminate possible overlapping auroral features. Auroral emission due to the electron precipitation is calculated and used to produce modelled images of the aurora. The modelled images reproduce the shape, structure and dynamics of the observed aurora extremely closely. The underestimation of the modelled brightnesses is most likely to be caused by the arc not completely filling the radar field of view as it passes through.

The ability to estimate auroral electron energy spectra and the resulting emissions at high resolution will allow further investigation of the highly structured and dynamic small scale aurora. By attempting to solve the continuity equation for species of interest, such as electrons or the metastable $O^+(^2P)$ ion, the three-dimensional structuring and dynamics of a species can be investigated. The metastable $O^+(^2P)$ ion is of particular interest because the motion of these ions can be used as a tracer of ionospheric electric fields. Modelling of emissions from $O^+(^2P)$ ions in addition to observations of said emissions should allow investigation of the electric fields associated with small scale aurora at sub-second resolution.

Chapter 6

Optical-only modelling of the aurora

6.1 Introduction

The technique of combined radar and optical modelling described in chapter 5 is limited in its application to observations where simultaneous radar observations of the E-region ionosphere at high range and temporal resolution are available. The radar observations must be of sufficient range and temporal resolution to allow reliable inversion of the observed electron densities to obtain the energy spectrum of the precipitating electrons, as described in section 4.1.

However, there may be events observed by ASK which do not have simultaneous radar observations, or the radar observations are of an unsuitable resolution to reliably invert. In the absence of suitable radar observations, the techniques described in chapter 5 cannot be used, and an alternative method must be used to determine the electron energy spectrum. Such an alternative method is presented in this chapter, which uses optical observations obtained from the ASK instrument to determine the energy spectrum.

A key requirement of this method is that the selected wavelengths of observations have some sensitivity to low energy electron precipitation. This requirement precludes the use of the 562.0 nm emission used in chapter 5, due to the insensitivity of this emission to low energy precipitation (see Figure 4.1). A suitable new event, which appears to exhibit significant production of O^+ ions and emission at 732.0 nm after the prompt emissions (673.0 nm and 777.4 nm) cease, is identified and analysed using the optical-only method.

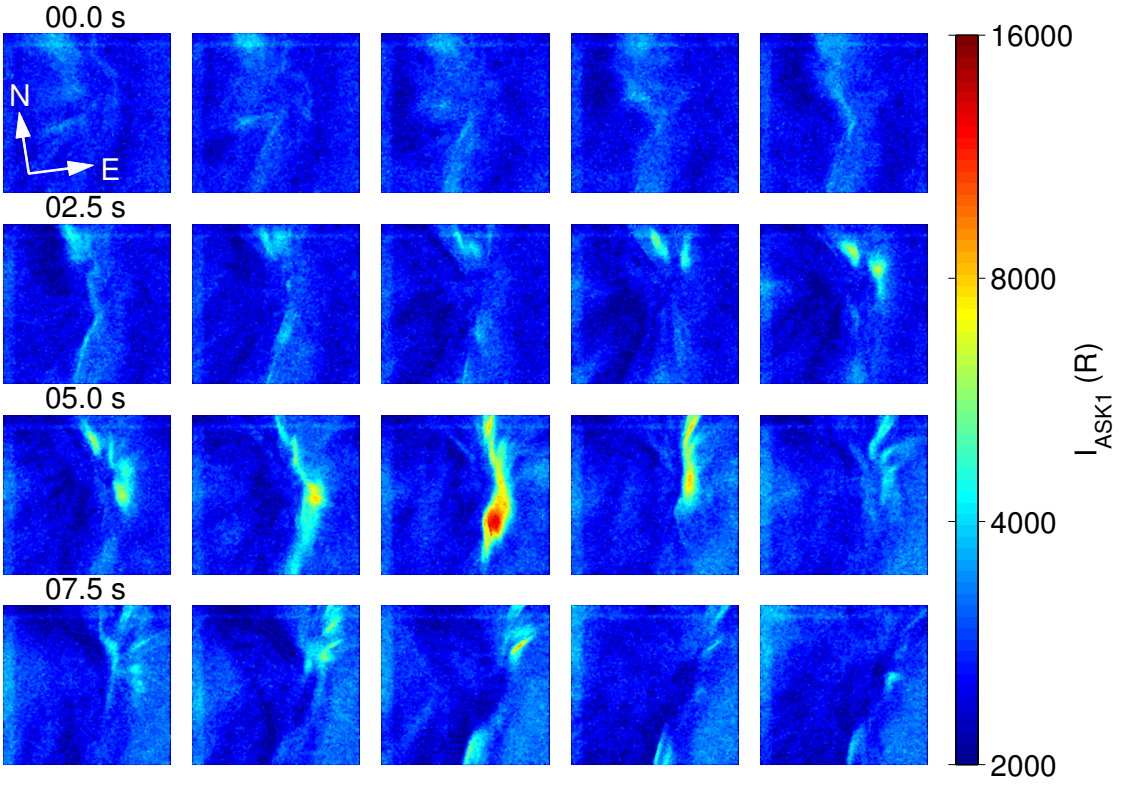

Figure 6.1: A sequence of images of the auroral brightness observed by ASK1 at 0.5 s intervals. A logarithmic colour scale is used to illustrate auroral structuring at both high and low intensity. The numbers above the images are the number of seconds after 21:25 UT when the corresponding image was acquired.

6.2 Observations

The event analysed in the present work occurred on 9 November 2006 during an auroral substorm. During this period ASK was equipped with filters centred on 673.0 nm (ASK1), 732.0 nm (ASK2) and 777.4 nm (ASK3). Shortly after 21:25 UT intense, highly structured and dynamic aurora was observed in and close to the magnetic zenith by ASK. Figure 6.1 is a ten second sequence of images from ASK1 at 0.5 s intervals. Before 21:25 UT there was diffuse aurora with no structure (not shown). As shown in the figure, up until 21:25:04 UT, the aurora moves closer to the magnetic zenith, brightens and begins to exhibit structure. At 21:25:04 UT the structured aurora intensifies, rising from 5 kR to 12 kR in ASK1 and from 2 kR to 6 kR in ASK3 (not shown). The intensification lasts for two seconds until 21:25:06.5 UT, after which the auroral brightnesses diminish to the levels at the start of the interval. After the bright prompt emissions have subsided, observations at 732.0 nm (ASK2) show continued emission at this wavelength. These emissions are from O^+ ions which were produced when the prompt emissions intensified but, due to the metastable nature of the O^+ ion, did not produce their emission during the intensification of the prompt emissions.

6.3 Modelling and Results

6.3.1 Optical estimates of energy and flux

Production and emission rates for the emissions observed by ASK are modelled using the Southampton ion-chemistry model. The model calculates a time series of production and emission rate profiles using an input time series of electron energy spectra. The model applies the electron transport method of Lummerzheim and Lilensten (1994) and the auroral model described in the appendix of Lanchester et al. (2001). Initial conditions relevant to the event are used and include estimates of neutral densities from the Mass Spectrometer Incoherent Scatter (MSIS) model (Hedin, 1991) and solar and geomagnetic indices, such as the $F_{10.7}$ solar radio flux and the A_p index. The cross-sections used are those described in Ashrafi et al. (2009) for the ASK1 emission and Julienne and Davis (1976) for the ASK3 emission. Modelled emission brightnesses are obtained by height integrating the emission rate profiles.

As the feature studied here is a discrete auroral form, monoenergetic electron energy spectra are more appropriate to use as input to the model than Maxwellian distributions. The monoenergetic spectra are approximated as Gaussian distributions with a narrow full-width at half maximum in energy. Figure 4.2 in section 4.2 shows the modelled emission brightness as a function of energy for the input electron energy spectra used here. These modelled emission brightnesses are calculated by height-integrating the emission rates and are a vital step in estimating the energy and energy flux of the precipitating electrons.

The modelled emission brightnesses are used in conjunction with observations of the aurora from ASK1 and ASK3 to estimate the energy and flux of the electron precipitation in the magnetic zenith (Lanchester et al., 2009). The ratio of the observed emission brightnesses is compared to the ratios of the modelled emission brightnesses to estimate the peak energy of the electron precipitation. Further, due to the relative insensitivity of the ASK1 emission brightness to precipitation energy, the energy flux is estimated using the ASK1 emission brightness.

To determine the energies and fluxes in the magnetic zenith, the position of the zenith within the images must be known. Models of the geomagnetic field, such as the International Geomagnetic Reference Field (IGRF), are often used to the calculate the position of the magnetic zenith at auroral altitudes. However, such models do not account for dynamics of the magnetic field under auroral precipitation conditions. Variations in the direction of the magnetic field of up to one degree have been observed (Whiter, 2008), which is significant for narrow field of view imagers such as ASK.

The method used here to determine the location of the magnetic zenith is that described by (Whiter, 2008). This method places the magnetic zenith at the vanishing point of

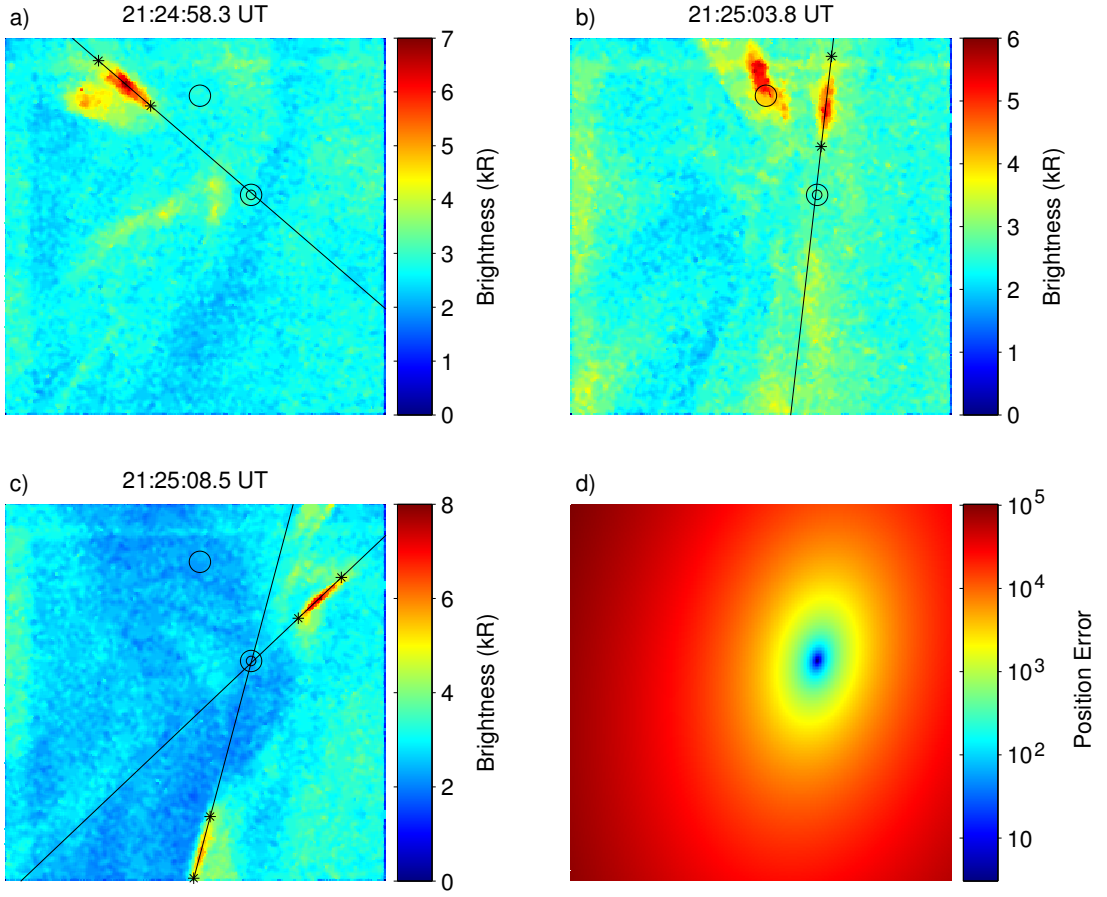

Figure 6.2: (a), (b), (c): Images of the auroral brightness observed by ASK1. The black lines pass through the rayed structures and the asterisks indicate the region of the line drawn manually. The single circle in each image is the position of the IGRF estimate of the magnetic field. The double circles indicate the estimate of the zenith position from the four rays. (d) The sum of the squares of the distances between a given pixel and each ray line.

auroral rays. Auroral rays are features that are spatially confined perpendicular to the magnetic field, but can extend several hundreds of kilometres parallel to the field. This method requires the presence of multiple rays, as a single ray cannot exactly determine the vanishing point. Rayed structure is present at times during the interval studied here. Figures 6.2(a), 6.2(b) and 6.2(c) show auroral forms that exhibit rays at 1.6 s before and at 3.8 s and 8.5 s after 21:25 UT.

For each ray, a line is drawn manually along the ray; the start and end points of this line are indicated by the asterisks in the figure. The line is extended across the image and the minimum distance from each pixel to the line is calculated. The location of the magnetic zenith within the images is at the pixel which minimises the sum of the squares of the distances between that pixel and each of the ray lines. The error at each pixel is shown in Figure 6.2(d) and the estimated position of the magnetic zenith is found to be at the minimum error. In Figures 6.2(a), 6.2(b) and 6.2(c) the double circles indicate

the magnetic zenith obtained using the ray method presented here; the single circles indicate magnetic zenith calculated using the IGRF model. The azimuth and elevation angles of the magnetic zenith are given by the azimuth and elevation of the line of sight of the pixel at the position of the magnetic zenith. This pixel is known as the zenith pixel, (u_z, v_z).

6.3.2 Perspective Correction

The large vertical-to-horizontal aspect ratios of aurora can cause significant perspective effects when observing off the magnetic zenith by even fractions of a degree; refer to section 2.1.2 for discussion. This perspective effect is highlighted by figure 6.3 which shows the observed 777.4 nm emission at 21:25:05.85 UT when the brightnesses of the prompt emissions were greatly enhanced. The black dashed line roughly delineates the extent of the observed auroral feature at 673.0 nm across the image. The position of the magnetic zenith is at the same position within the images of the 673.0 nm and 777.4 nm emissions. On the zenithward side of the feature, the 777.4 nm emission extends beyond the extent of the 673.0 nm emission; the reverse is seen on the anti-zenithward side of the feature. This difference in position of the auroral feature between the images is due to the differing responses of molecular nitrogen and atomic oxygen to the particle precipitation. Figure 4.1 shows that, for electron energy spectra that carry the same total energy flux and have the same peak energy, the emission rates profiles for the atomic oxygen peak at higher altitudes than the molecular nitrogen profiles, and that in general the 777.4 nm emission occurs at a higher altitude than the 673.0 nm emission. This is the perspective effect which needs to be corrected for if an emission ratio method is to be used to calculate the characteristics of the electron precipitation.

To correct for these perspective effects, instead of taking the ratio of the observed brightness at identical pixels (u, v) in both the 673.0 nm and 777.4 nm images, the pixel in the 777.4 nm emission should be closer to the magnetic zenith to allow the perspective effect to be corrected. The shift will be both dependent on both the position of the pixel in the 673.0 nm emission and the energy of the precipitation. A simple geometrical method is used here to correct for the perspective effect by calculating this shift toward the zenith in terms of the pixel co-ordinates (u, v). Figure 6.4 depicts a situation when aurora occurs along a magnetic field line that is not in the magnetic zenith. The field line on which there is aurora is some perpendicular distance, d, away from the magnetic zenith. Example emission rate profiles for the emissions observed by ASK1 and ASK3 are shown on the right of figure 6.4 and highlight the separation of the peak emission altitude. The altitude of peak emission for each profile is marked by the dashed lines. The pixel lines of sight through the positions of the altitudes of peak emission subtend angles θ_1 and θ_3 with the magnetic zenith for the emissions observed by ASK1 and ASK3 respectively.

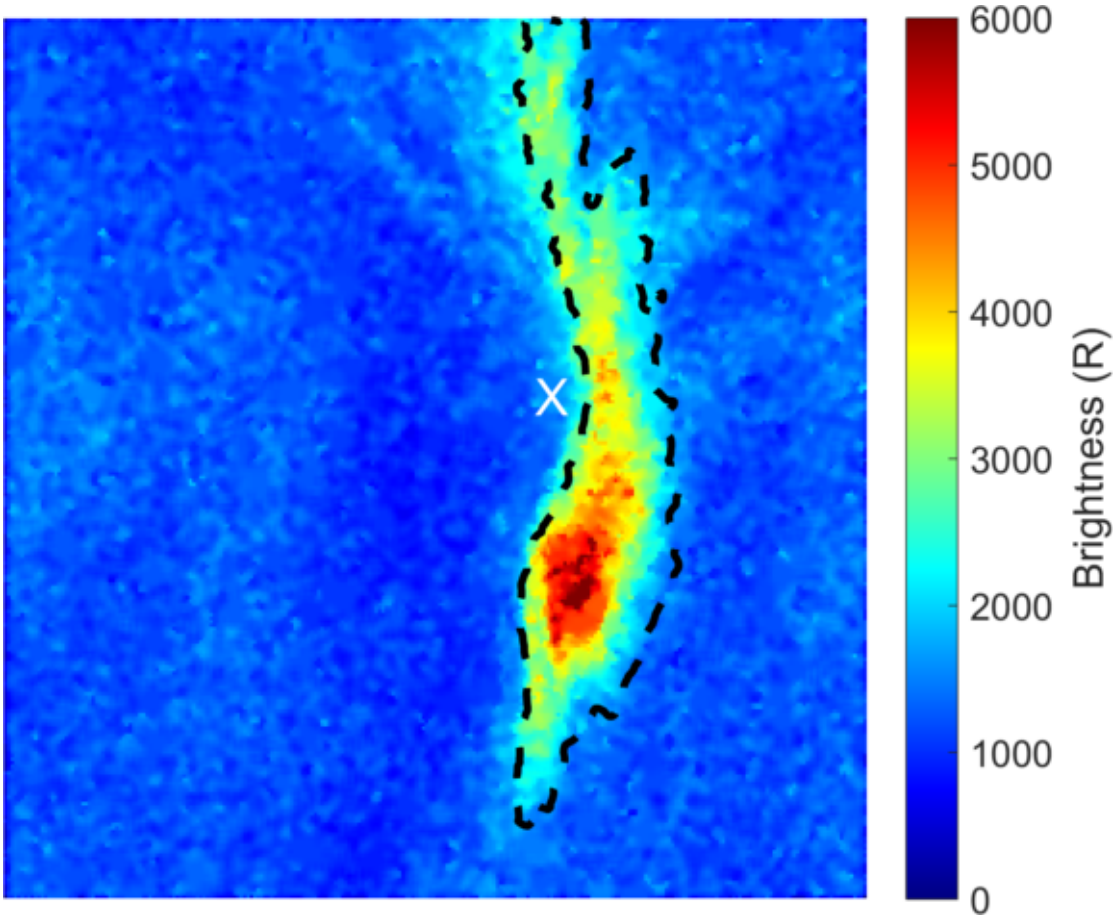

Figure 6.3: Observed auroral 777.4 nm emission brightness at 21:25:05.85 UT. The black dashed line is the 4 kR brightness contour for the 673.0 nm emission. The position of the magnetic zenith is marked by the white cross.

We define the image distance between the zenith pixel, (u_z, v_z), and the pixels whose lines of sight pass through the altitudes of peak emission to be n_1 in the ASK1 image and n_3 in the ASK3 image. The unit vector $\hat{\underline{r}}$ from any given pixel (u, v) toward the zenith pixel is given by:

$$\hat{\underline{r}} = \frac{(u_z - u)\hat{\underline{u}} + (v_z - v)\hat{\underline{v}}}{\sqrt{(u_z - u)^2 + (v_z - v)^2}} \tag{6.1}$$

where $\hat{\underline{u}}$ and $\hat{\underline{v}}$ are unit vectors in image co-ordinate directions. As emissions observed by ASK3 originate from a higher altitude than those observed by ASK1, features in ASK3 will appear closer to the zenith pixel than features in ASK1. This fact allows the image positions of the ASK1 image to be used as a reference and the perspective correction to be applied to the ASK3 image. The denominator in equation 6.1 is also simplified; if the ASK1 image is used as a reference, then the denominator is the image distance n_1. The image distance of the apparent shift in position is defined as:

$$n_s = n_1 - n_3 \tag{6.2}$$

where n_s is the image distance that the position of the ASK3 peak emission altitude

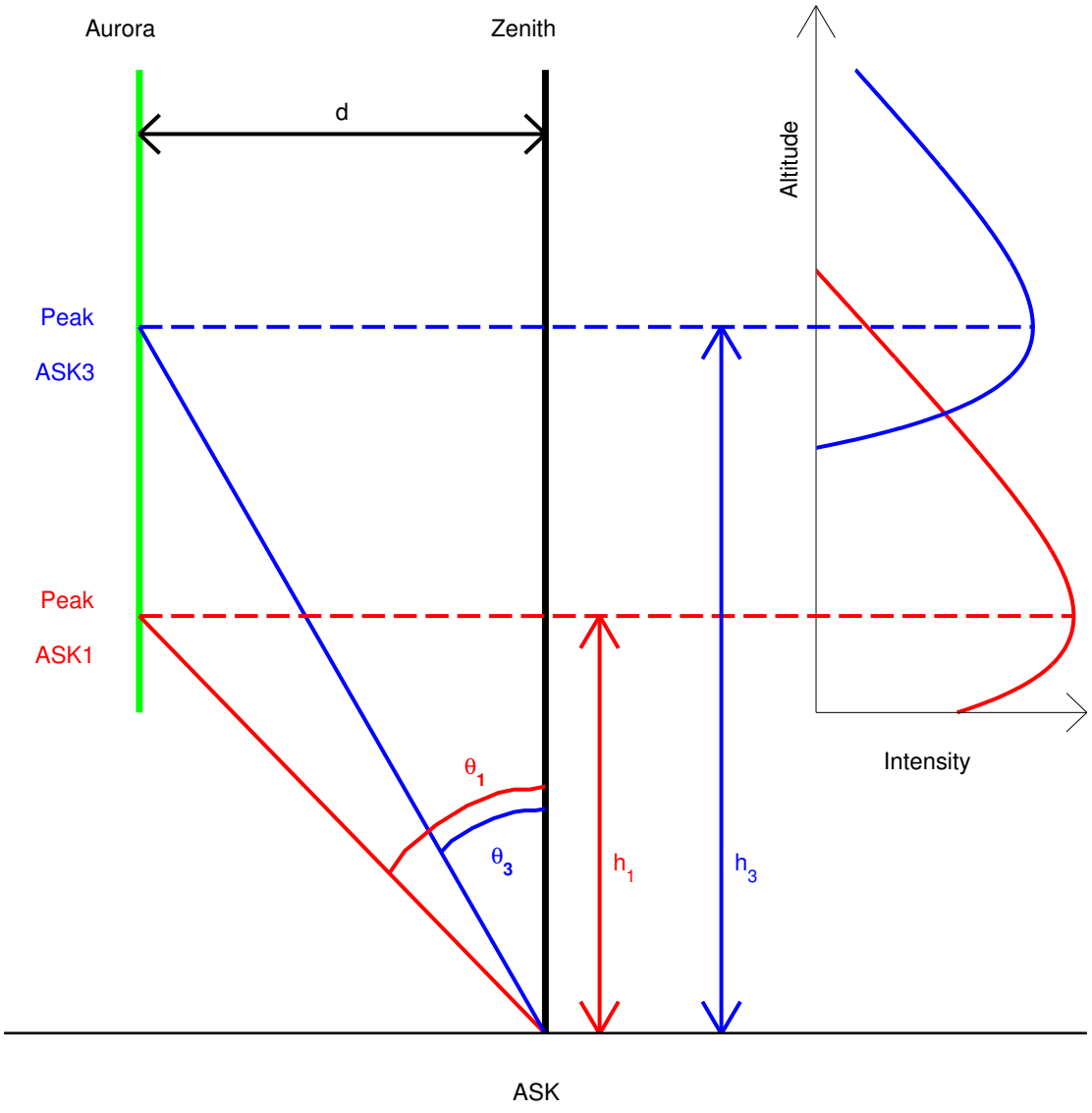

Figure 6.4: The simple geometric model used to estimate the perspective effects. The plot in the upper right shows idealised ASK1 and ASK3 emission rate profiles.

appears shifted toward the zenith compared to the position of the ASK1 peak emission altitude. This shift is the perspective effect that needs correction.

The variation of image distance with angle is linear and obeys the following relation:

$$\frac{\theta_T}{n_T} = \frac{\theta_1}{n_1} = \frac{\theta_3}{n_3} \tag{6.3}$$

where n_T is the image distance across the entire image and θ_T is the field of view of the observed image. The angles in equation 6.3 are eliminated, using trigonometry and the small angle approximation, to yield the following relation between the image shifts and the altitudes of peak emission, h_1 and h_3:

$$n_3 = n_1 \frac{h_1}{h_3} \tag{6.4}$$

The altitudes of peak emission are obtained from an initial estimate of the energy that is obtained using the methods described in section 6.3.1. Equation 6.4 can be combined with equation 6.2 to yield a relation between the apparent shift in position to the ASK1 image distance and the altitudes of peak emission:

$$n_s = n_1(1 - \frac{h_1}{h_3}) \tag{6.5}$$

Combining the image distance of the shift from equation 6.5 with the expression for $\hat{\underline{r}}$, the displacement of the shift toward the zenith, $\underline{r}_s$ is found:

$$\underline{r}_s = n_s\hat{\underline{r}} = (1 - \frac{h_1}{h_3})\{(u_z - u)\hat{\underline{u}}) + (v_z - v)\hat{\underline{v}})\} \tag{6.6}$$

Decomposing $\underline{r}_s$ from equation 6.6, shows that shifts along the image co-ordinate directions are given by:

$$\Delta u = (1 - \frac{h_1}{h_3})(u_z - u) \tag{6.7}$$

and

$$\Delta v = (1 - \frac{h_1}{h_3})(v_z - v) \tag{6.8}$$

Therefore, to account for perspective effects when calculating the energy, the following ratio of brightnesses should be used:

$$R(u, v) = \frac{B_1(u, v)}{B_3(u + \Delta u, v + \Delta v)} \tag{6.9}$$

where $B_1(u, v)$ is the brightness in the ASK1 image at pixel (u, v) and $B_3(u+\Delta u, v+\Delta v)$ is the brightness in the ASK3 image at pixel $(u + \Delta u, v + \Delta v)$. By taking this ratio at every pixel in the ASK1 images, a map of the energy of the electron precipitation is produced.

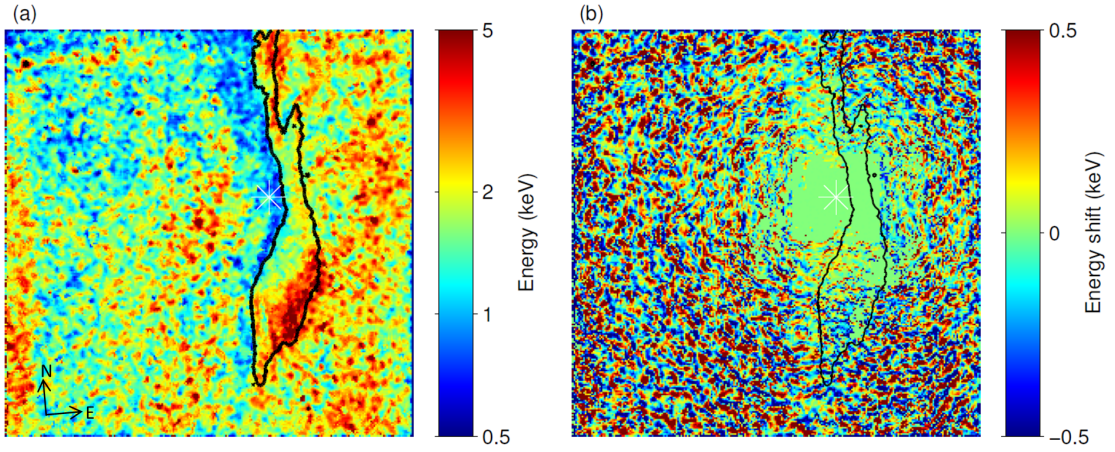

Figure 6.5: (a) Perspective corrected estimate of energy across the ASK field of view. (b) Shift in energy after application of the perspective correction. The black lines are contours of the ASK1 image brightness at 4 kR and the white asterisk indicates the position of the magnetic zenith.

The perspective-corrected map of energy across the ASK field of view at 21:25:06 UT is shown in figure 6.5(a) and the change in energy due to the perspective-correction is shown in figure 6.5(b). The black lines are brightness contours, at 4 kR, of the observed ASK1 brightness at this time. The perspective-corrected estimates of the energy suggest the energies of the precipitating electrons are approximately 1 keV along the western edge of the feature and rise to 5 keV on the eastern edge. Figure 6.5(b) shows that in this instance there is little change in the estimated energies when the perspective correction is applied, because of the proximity of the feature to the magnetic zenith. There are small changes in energy along the southernmost section of the feature, with estimates of the energies rising slightly along the edge closest to the zenith and falling slightly along the edge furthest from the zenith.

6.3.3 Volume emission rates

Maps of energy flux and perspective-corrected energy are used to model the volume emission rates of the auroral emissions observed by ASK. A 3-D volume that fully encloses the ASK field of view at auroral altitudes between 90 km and 350 km is used, measuring 30 × 30 × 260 km. The volume has a resolution of 200 m and the long axis is aligned with the magnetic zenith, so that each column in the volume represents a magnetic field line through the volume. Emission from each voxel in the volume is modelled as a blob that varies spatially as the square of a cosine function. The cosine function produces a maximum in emission at the centre of the voxel and a minima, of zero, at the centre of the orthogonally adjacent voxels. The projection of a blob of this shape is invariant to projection direction.

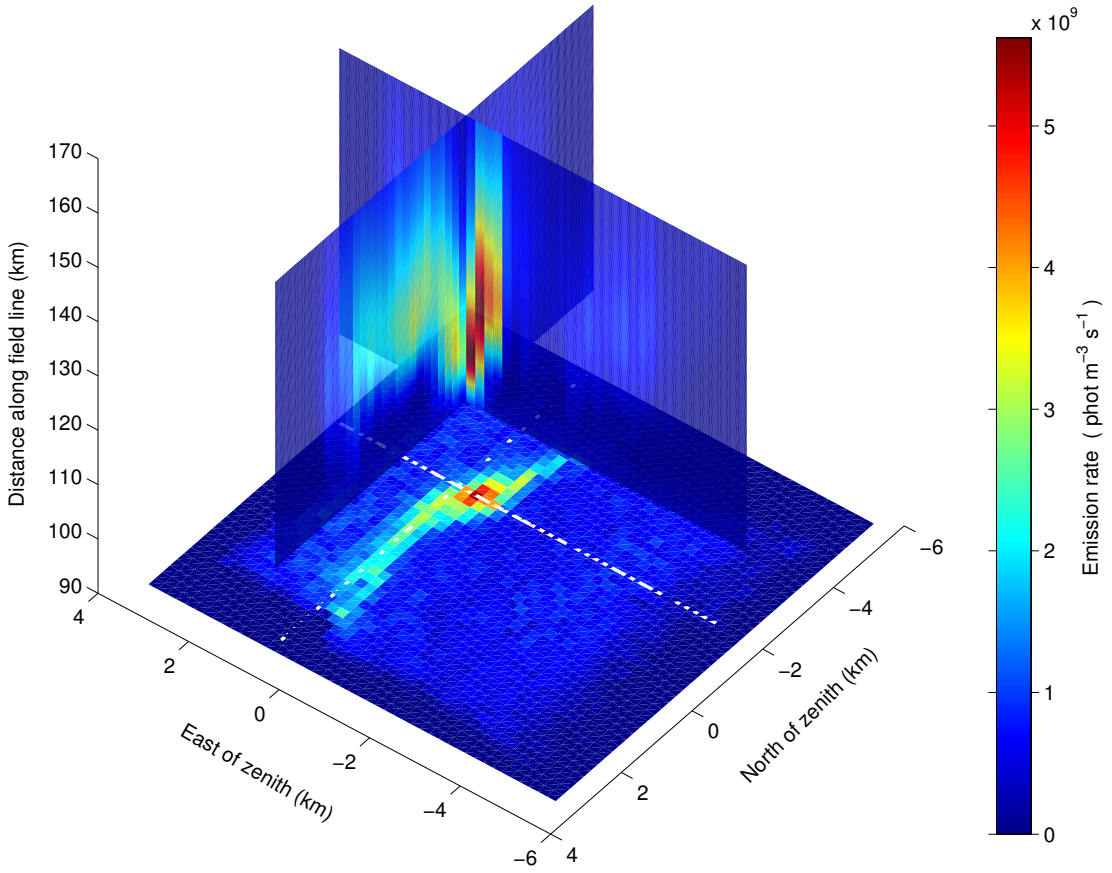

Figure 6.6: Volume emission rates for the 673.0 nm emission at 21:25:06 UT showing emission rate profiles across the feature, in the vertical slices, and the height integrated emission rates, in the horizontal plane below the vertical slices. The height integrated emission rates have been scaled, by a factor of 1/200, to ensure features in both the vertical slices and the horizontal plane are visible. The dashed lines on the horizontal plane indicate the spatial extents of the vertical slices.

The volume is populated using the maps of peak energy and energy flux. At each pixel an emission rate profile is calculated using the peak energy at that pixel. The intersections of the pixel line of sight with the magnetic field aligned columns of the volume are found using the method described in section 4.3. The emission rate profile is placed along the field-aligned column that minimizes the separation, along the field-aligned column, of the intersection and the peak emission altitude of the profile. The energy flux is scaled from the fixed value of 1 mWm^{-2} to that of the optical value obtained from the ASK1 brightness. This process is repeated for all pixels in the image. As there are more pixels in the image than field-aligned columns in the 3-D volume, multiple pixels may project to the same field-aligned column. Where this occurs, the emission rate profile along that field-aligned column is the mean of all contributing emission rates.

Figure 6.6 demonstrates the full 3-D result of the analysis for the 673.0 nm emission. Two vertical slices through the volume in north-south and east-west directions reveal

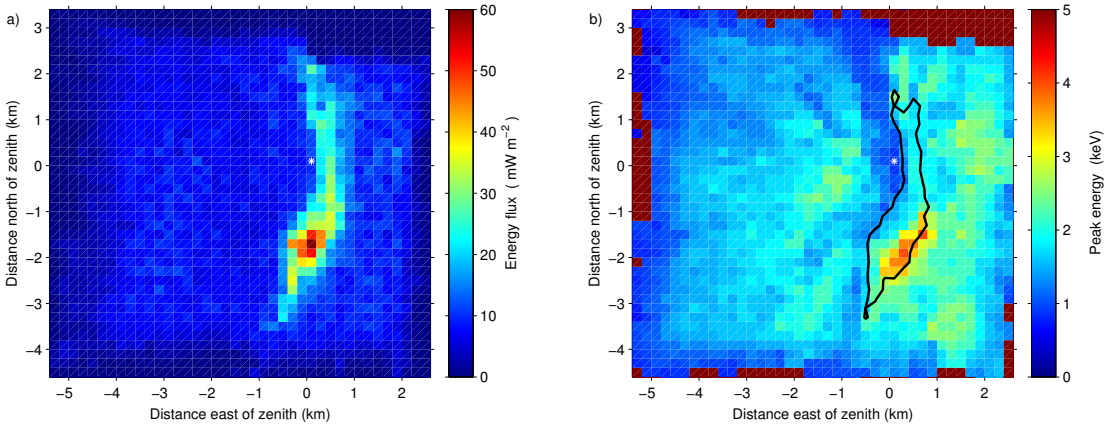

Figure 6.7: Energy flux (a) and peak energy (b) of electrons precipitating along magnetic field lines in the volume observed by ASK at 21:25:06 UT. The white asterisk indicates the position of the magnetic zenith at auroral altitudes as observed from the location, on the ground, of the ASK instrument. The black line is the contour of energy flux at 20 mWm^{-2}.

the structuring of the modelled emission rates both perpendicular and parallel to the magnetic field. Additionally, the height integrated volume emission rates are shown in the horizontal plane below the volume to reveal the structure of the auroral feature perpendicular to the magnetic field. The emission rate profiles peak at altitudes between 120 km and 135 km. The peaks are at lower altitudes on the eastern and southern edges of the feature where the energy is higher (5 keV).

Maps of the spatial variation of the precipitation energy and energy flux are shown in Figure 6.7 when the auroral feature was near peak brightness at 21:25:06 UT. The map of energy flux (a) shows the auroral feature is less than 1 km in width and in places only 400 m across. Within the auroral feature there is a small region of intense energy flux, of up to 60 mWm^{-2}, to the south of the magnetic zenith. The energy fluxes in most of the volume are lower and exhibit little structure. At the fringes of the volume the energy fluxes are greatly diminished because these field lines are close to or outside the ASK field of view at typical auroral altitudes; therefore there are few or no pixels which project to these field lines. The net energy fluxes also exhibit a strong similarity to the observed structure of the aurora, which is a result of the relative insensitivity of the 673.0 nm emission to the energy of the precipitation. On the energy map (b), the black line is the 20 mWm^{-2} energy flux contour and roughly delineates the spatial extent of the discrete auroral feature. The energy map shows the energy rises across the feature from west to east. There is also a difference in the peak energy of the precipitation on either side of the feature, with the peak energy being lower on the western side (1 keV) than on the eastern side (2-3 keV).

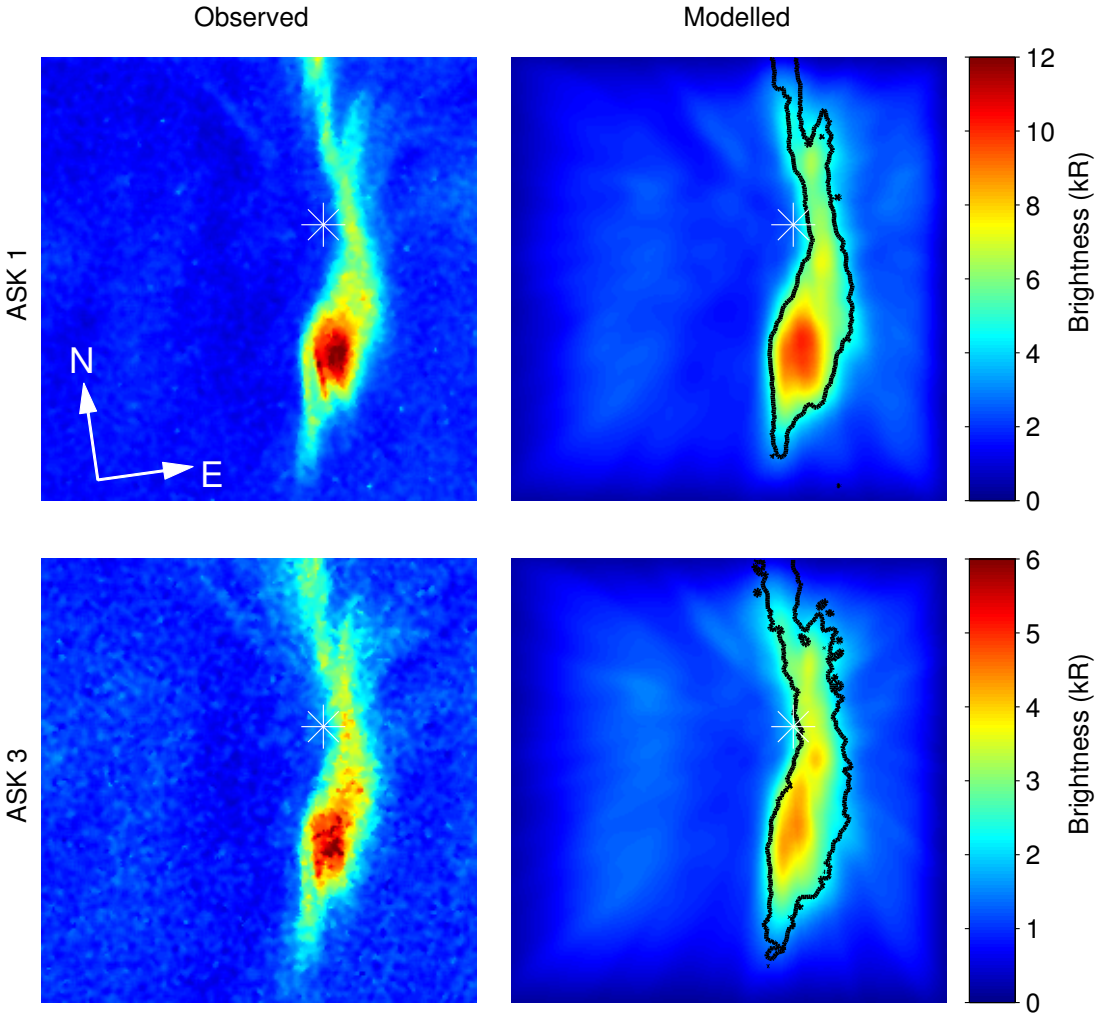

Figure 6.8: Observed (left column) and modelled (right column) images of the auroral brightness as observed by ASK1 (top row) and ASK3 (bottom row) at 21:25:06 UT. The black lines on the modelled images are intensity contours of the observed images at 4 kR (ASK1) and 2 kR (ASK3). The white asterisks indicate the position of the magnetic zenith.

6.3.4 Image modelling

The accuracy of the emission rates is verified by comparing the observed images from ASK1 and ASK3 with modelled images. The latter are formed by projecting the emission rates to an image plane on the ground, at the ASK location, using the blob-based dot projection method of Rydesäter and Gustavsson (2001). A calibration image of a uniform 1 Rayleigh emission rate is produced. The brightnesses of the modelled images in Rayleighs are obtained by dividing the image of the projected emission rates by the calibration image. Finally, the effects of the passbands and transmittances of the filters on the modelled brightnesses are accounted for by multiplying the modelled brightnesses by a filter factor of 0.72 for ASK1 and 0.70 for ASK3.

A comparison of the modelled and observed images from both ASK1 and ASK3 is shown in Figure 6.8. The black lines delineate the extent of the discrete auroral feature in the respective observations. The position, structure and brightness of the discrete auroral feature in the observed and modelled ASK1 images show excellent agreement. For ASK3, the modelled brightnesses underestimate the observed brightnesses and the feature has a small shift toward the position of the magnetic zenith in the image.

A quantitative comparison of the observed and modelled images is performed using a measure of similarity known as the structural similarity index (SSIM) (Wang et al., 2004). The SSIM between two images, x and y, is defined as:

$$SSIM(x,y) = \frac{(2\mu_x\mu_y + C_1)(2\sigma_{xy} + C_2)}{(\mu_x^2 + \mu_y^2 + C_1)(\sigma_x^2 + \sigma_y^2 + C_2)} \tag{6.10}$$

where μ_x and μ_y are the respective means of images x and y, σ_x^2 and σ_y^2 are the respective variances, σ_{xy} is the covariance of the two images, and C_1 and C_2 are constants. These constants are included to prevent instabilities in the SSIM, which can arise if the mean or variance is zero. The means and variances, on both global and local image scales, of the observed and modelled images studied here are never zero. Therefore, both C_1 and C_2 are set to zero. The SSIM takes a value in the range $-1 \leq \text{SSIM} \leq 1$. A SSIM of $+1$ implies the two images are identical, a SSIM of zero indicates the images have no similarity and a SSIM of -1 means that the images are inversely related. The SSIM is evaluated locally, here using a square sliding window with a width of nine pixels, to obtain a map of the similarity across the image.

Figure 6.9 shows such maps for (a) the ASK1 and (b) the ASK3 images. The black lines indicate the observed spatial extent of the auroral feature in the corresponding emission. Figure 6.9 shows that within and surrounding the auroral form the SSIM is generally high, however there are some small regions of the ASK1 image and a larger region, elongated along the feature, of the ASK3 image where the SSIM is low. In the regions of diffuse aurora, some distance from the auroral form, the SSIM shows much greater variation, but in general there appears to be little similarity in these regions.

6.4 Discussion

In the absence of direct observations of the spatial distribution of auroral electron energy spectra, the purpose of the modelled images is to verify the accuracy of the inferred energy spectra of the precipitation and the resulting 3-D emissions. The modelled and observed images are very similar, with the brightnesses and large scale structure well modelled. However, a quantitative analysis reveals that only the regions of the images that correspond to bright feature showed high similarity. There are several factors that affect the similarity of the modelled images. Some of these are related to the setup of

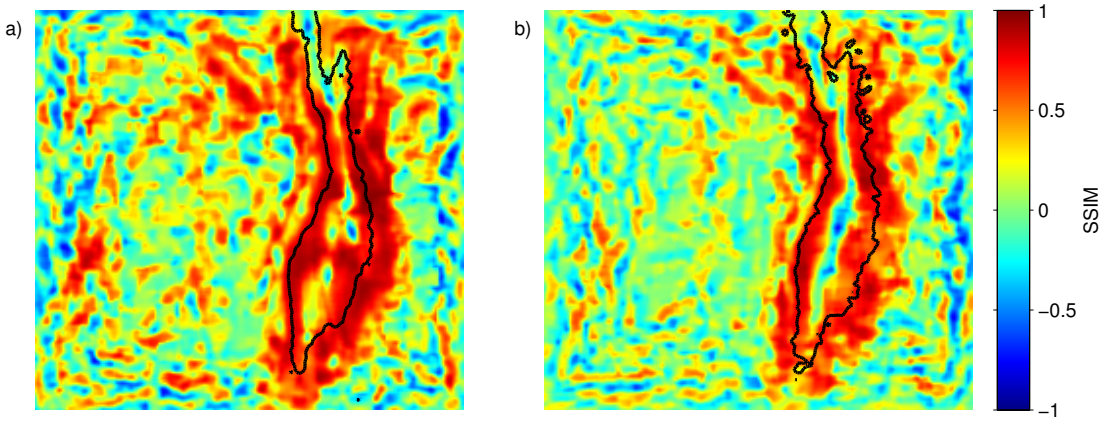

Figure 6.9: Local values of the structural similarity index at 21:25:06 UT, when the discrete auroral form was brightest for (a) ASK1 and (b) ASK3. The black lines are brightness contours at 4 kR and 2 kR in the ASK1 and ASK3 observations respectively.

the modelling volume, such as the orientation of the magnetic field and the resolution of the volume, and others are a result of properties of the images, such as residual noise.

One of the most important parameters in production of the modelled images is the magnetic field direction at auroral altitudes within the volume enclosed by the ASK field of view. The magnetic field direction, and hence the position of the magnetic zenith within the images, has been calculated using both the IGRF model and a method using rayed auroral structures (Whiter, 2008). Figure 6.2 shows there is a discrepancy in the position of the magnetic zenith obtained using these methods of approximately 0.9 degrees, most of which is due to differences in the elevation angle. It is likely that the discrepancy is a result of the auroral activity. It is well known that auroral activity is correlated with magnetic disturbances on the ground. These disturbances are due to magnetic fields that are generated by currents in the ionosphere. Field-aligned currents around auroral features will cause a perturbation on the background magnetic field. In our method, the lines which pass through the rays are drawn manually, so there are uncertainties in position of not more than five pixels in selected points on each ray line. However, all ray lines pass within two pixels of the recovered position of the magnetic zenith, suggesting this uncertainty is small in the event presented here. Further, the rays used to reconstruct the position of the magnetic zenith are separated in time, by up to 10 seconds. The reconstruction assumes that during this interval, the position of the magnetic zenith does not vary.

The perspective-correction is affected by the proximity of the auroral feature to the magnetic zenith. Because of this proximity, the positional shifts that result from the perspective-correction are small. However, there is evidence that the perspective-correction works. In the southern region of the observed feature, the perspective-corrected energies are reduced on the side of the feature furthest from the zenith and increased on the side

closest to the zenith. Where the energy is 5 keV the difference in peak emission altitude is a few hundred metres, resulting in small or negligible positional shifts no matter how far from the zenith the feature is. Where the energy is 1 keV, the difference in peak emission altitude is a few kilometres, which causes significant perspective effects. However, for the feature studied here, the regions of the bright feature where the energy is low are close to the zenith, which reduces the magnitude of the required perspective-correction.

A second important factor in producing modelled images of the aurora is the altitude to which the emission rates are projected when populating the 3-D volume. In this work, the projection is to the altitude of peak emission, which is the altitude at which the emission rate is a maximum. However, the prompt emission rate profiles shown in figure 4.1 show an imbalance in net emission rate above and below this peak altitude; with the net emission rate above the altitude of peak production is greater than that below. Instead it would have been better to use an average emission-weighted altitude, such that equal amounts of emission occur above and below this altitude. As the average emission altitude is higher than the peak altitude for all prompt emission rate profiles, the emission rate profiles are not projected far enough perpendicular to the magnetic field. As a result, the emission rates have not been projected far enough perpendicularly the modelled features will appear closer to the magnetic zenith than they should. This effect can be seen in the 'bright spot' directly below the position of the magnetic zenith in the modelled image for the 777.4 nm emission, which is shown in bottom row of figure 6.8; this bright spot is closer to the magnetic zenith in the modelled images than the observed images. This effect can also be seen in the negative values of the SSIM along the centre of the bright feature for the 777.4 nm emission, shown in figure 6.9. These poorly matched regions of the images are due to comparing regions in which there are large differences in both the image brightness, and the image gradient. A lessened effect is observed when comparing images of the 673.0 nm emission. This difference is likely because the emission rate profiles for the 673.0 nm emission have a narrower altitudinal extent and a lower average emission altitude.

The resolution of the volume in which the emissions are modelled also affects the similarity of the modelled images. Both modelled images in Figure 6.8 show emission that extends beyond the spatial extent of the observed auroral feature. As the auroral feature is close the magnetic zenith, this 'overflow' may also be due to the finite resolution of the modelled volume, in addition to the assumed emission height effect discussed above. Studies of the auroral width spectrum have shown auroral structures have widths down to a few tens of metres (Sandahl et al., 2008), which is contrasted with the 200 m spatial resolution of the volume. The choice of using a 200 m resolution for the volume was a trade-off between the precision of the modelling and the available computational hardware and time to perform the modelling. The modelling of the 3-D volume is linear, allowing the volume to be broken down into several sub-volumes which together comprise the entire 3-D volume. The modelled images of the whole 3-D volume could then

be formed by a superposition of the images from the sub-volumes. Such a method would allow for the resolution of the modelling to be decreased at the expense of computational time used.

Accurate estimates of the energy and energy flux of the precipitation require adequate subtraction of any background. The event studied here occurs during an auroral substorm, with discrete and diffuse aurora present both before and after this event. The presence of diffuse aurora during the event analysed here means that a 'quiet' region of the image could not be used for background subtraction. Instead observations from approximately 20 minutes before and after the event were analysed, for both prompt emissions, to find a period of time devoid of auroral emissions. The background brightness is then calculated from this time period. However changes in the background brightness between the period devoid of emissions and the event studied here are unaccounted for. Such changes would be due to changes in atmospheric conditions, for example haze or thin cloud in the field of view. Uncertainties in the brightness of the background would have a negligible effect on the estimates of energy and energy flux from bright features. However, energies and fluxes estimated for features with a lower emission brightness, such as the diffuse aurora which accompanies the event studied here, would be more uncertain.

Estimates of the energy and flux for features where the emission brightnesses is low, such as the diffuse aurora during this event, are strongly affected by any residual noise in the images. Residual noise in the 673.0 nm emission propagates through to the estimates of energy flux, which will then propagate through to the modelled images. However as the resolution of the 3-D grid on which the production and emission rates are modelled is much larger than the resolution of the observations at typical auroral altitudes, 200 m compared to 20-40 m respectively, the effect of noise in the modelled images is suppressed by averaging. The averaging occurs naturally here because the modelled emission rates along each column of the 3-D grid have contributions from many pixels in the images. Residual noise in the observations has a much greater effect on the estimates energy. As a ratio of the brightnesses is used to estimate energy when the brightnesses are low, small changes in either of the brightnesses can cause large changes in the resulting energy. This manifests as a noise-like appearance in the estimates of the energy, which can be seen in Figure 6.5(a). When the estimates of energy and flux are projected to the 3-D grid, the noise-like behaviour in the energy is somewhat suppressed by the same averaging that affects the flux, as can be seen in Figure 6.7.

Residual noise in the images also affects the similarity of the images, through the covariance term of the SSIM, with the SSIM lower when the images are noisier. Additionally, the noise also propagates through to the modelled images and produces the ray-like structures that can be seen in the modelled images in Figure 6.8. The cause of these structures is the variability in the energy flux along neighbouring field lines in the regions

of diffuse aurora, which can be seen in Figure 6.7(a). This variability causes the emission produced along that field line to appear brighter or dimmer than the surrounding emission, leading to the ray-like structures in the observed images.

In this work it is assumed that the magnetic field lines are straight and parallel within the modelled volume. Field line curvature means that the position of the magnetic zenith depends on the altitude at which the magnetic field direction is calculated. This curvature has an effect when the emission rate profiles have a large (hundreds of km) altitude extent. Such profiles are obtained only when there is a large contribution to the profile from electrons with energies of hundreds of eV of less. For the feature studied here the energies are greater than 1 keV, therefore the effect of field line curvature can be neglected.

As well as evaluating the accuracy of the estimated spectra, the results of this work provide further evidence in support of the theory that bright and discrete auroral features can be a consequence of elevated energy fluxes and that such features act as boundaries between contrasting precipitation distributions. Lanchester et al. (1997) used optical and radar observations in conjunction with ionospheric modelling to analyse a bright and narrow (100 m) auroral filament, finding the filament was due to greatly enhanced energy fluxes within a broader region of precipitation. Later, using the ASK instrument, Dahlgren et al. (2008b) and Dahlgren et al. (2011) analysed discrete auroral features that exhibited sub-kilometre structuring. The analysed features were found to be a result of enhanced energy fluxes and the bright features were at the boundary between two regions of diffuse aurora, each of which had a different energy distribution of precipitating electrons. In this work, the structure of the observed auroral brightnesses more closely matches the structuring of the energy flux than the structuring of the peak energy. This is in agreement with the previously discussed works, and shows that the structuring and dynamics of the bright feature studied here is due to changes in energy flux rather than changes in energy. Further, the energy map suggests that the feature separates two regions of diffuse aurora that have different peak energies.

6.5 Conclusions

Modelling of the structuring and dynamics of volume emission rates for selected auroral emissions in a region surrounding the magnetic zenith is described. The method corrects for the perspective effects of auroral features away from the magnetic zenith direction; estimates are found of the energy and flux of the electron precipitation across the 3 degree field of view of a state-of-the-art multi-monochromatic imaging instrument. The estimates of energy and flux are used to model the observed volume emission rates of emissions at wavelengths of 673.0 nm and 777.4 nm. The agreement between modelled and measured images verifies the estimated peak energies and energy fluxes. However

further work is needed to investigate the effect to the altitude to which the emission rates are projected when populating the 3-D volume.

The spatial and temporal changes in the peak energy and energy flux of the electron precipitation through a volume surrounding the magnetic zenith are also investigated. It is found that the increases in brightness correspond to increases in the energy flux of the precipitation rather than the peak energy. The maximum energy flux within the feature is found to be 60 mWm^{-2} and the energy is found to vary between 1 and 5 keV. It is also found that the discrete feature is at a boundary between two regions of diffuse aurora, each with different energy and flux characteristics. Such results are in agreement with the results of Lanchester et al. (1997), Dahlgren et al. (2008b) and Dahlgren et al. (2011).

The direction of the magnetic zenith has been calculated using both the IGRF model and a novel method using auroral rays. A discrepancy is found between the established and novel methods; this discrepancy is real and is due to magnetic fields generated by ionospheric currents present during times of auroral activity. The proximity of low energy regions of the discrete auroral feature to the magnetic zenith causes the perspective correction to the energy to be small. To investigate the effectiveness of this perspective correction effect, further low energy events should be studied. However, for the purposes of the work here, the results are sufficient to attempt three-dimensional modelling of the distribution of O^+ ions during this event.

Electric fields present during this event would affect the motion of any O^+ ions produced during this event. The success of the modelling presented in this section allows the motion of the O^+ ions to be investigated at the spatial and temporal resolutions of the modelling and observations.

Chapter 7

The flow model

7.1 Introduction

In this chapter the electric fields surrounding the auroral features analysed in chapters 5 and 6 are investigated. These electric fields are inferred from plasma velocities obtained from three-dimensional modelling of the dynamics of the long-lived $O^+(^2P)$ ion, which has a lifetime of approximately 5 s. A critical step in the modelling of the structuring and dynamics of the $O^+(^2P)$ ion is the production of this ion by auroral electron precipitation. The methods developed in chapters 5 and 6 were used to determine the energy spectrum of this precipitation, and the resulting production rates of $O^+(^2P)$ ions are modelled using the Southampton ion-chemistry model, described in section 4.2.

Existing methods and results from previous investigations of auroral electric fields are presented in section 2.4. However none of these methods are able to obtain estimates of the electric fields surrounding dynamic fine-scale auroral features at the temporal resolution of the observed features.

Rockets and satellites provide in-situ measurements, allowing the electric fields surrounding auroral features to be directly measured. However the rapid motion of such observation platforms mean that in-situ measurements are unable to capture the dynamics of the electric field as all measurements originate from a short period of time. Such in-situ measurements of electric field are often interpreted as spatial, rather than temporal, observations.

Ground-based observations rely on inferring the electric field from measurements of velocity. Coherent and incoherent scatter radars, such as SuperDARN and EISCAT, measure the line-of-sight Doppler shift in the frequency of radio waves scattered by electrons in the ionosphere. Observations from multiple radar stations, with different look-directions, are combined to give the 3-D plasma flow in the observed volume. However, the time-scale of resulting velocities is typically of the order of minutes (SuperDARN) or

a few tens of seconds (EISCAT), neither of which would allow the sub-second dynamics of the electric-field to be investigated.

Optical observations have also been used to estimate plasma flows. Both ground-, and satellite-based line-of-sight Doppler shift measurements from auroral emissions have been used, (Smith, 1982) and (Carr, 1992) respectively; however this method requires combining measurements from multiple look-directions obtained at different times, yielding a result which itself is an average over a longer time-scale. Further, this method cannot be applied to observations of the aurora in the magnetic zenith as the motion perpendicular to the magnetic field would not produce a Doppler shift.

Methods that have been more successful in reaching sub-second time resolutions involve modelling and tracking the motion of long-lived excited states. Long-lived artificial emissions, excited using high-power radio waves, such as the 630.0 nm emission from atomic oxygen have been tracked and used to infer plasma drifts and neutral winds in the F-region ionosphere at the resolutions of the observed images (Bernhardt et al., 2000; Gustavsson et al., 2001). The significance of these investigations lies in the techniques used to model, in 3-D, the distribution and evolution of the excited emitting state. In particular, the modelling technique of Gustavsson et al. (2001) is adapted and applied to the $O^+(^2P)$ ion, with the necessary production rates of $O^+(^2P)$ ions coming from the work presented in chapters 5 and 6.

A technique to model and track the emissions from drifting $O^+(^2P)$ ions have previously been developed. Dahlgren et al. (2009) tracked the motion of an 'afterglow', which is the emitting $O^+(^2P)$ ions which are left behind after the prompt emissions have ceased. Using an assumed emission height, based on the energies of the electron precipitation which caused the prompt emissions, they were able to extract plasma velocities of the order of hundreds of m/s, which yielded electric fields of tens of mV/m. However, this method is reliant on there being no auroral precipitation occurring during the analysis of the afterglow. If auroral precipitation is occurring, then the relative effects of the production and drift of the $O^+(^2P)$ ions cannot be resolved. This issue can be resolved if the 3-D distribution and evolution of the $O^+(^2P)$ ions is modelled and both production and drift effects are considered.

In this chapter, such a method of modelling the 3-D distribution and evolution of $O^+(^2P)$ ions is presented. This method is adapted from the method of Gustavsson et al. (2001), which poses finding the flow velocities as an optimisation problem. The dynamics of the $O^+(^2P)$ ion are discussed in the context of this method. Two possible parameterisations of the flow velocities are motivated and discussed; the first is a simple uniform flow perpendicular to the magnetic field, the second is a sheared flow also perpendicular to the magnetic field.

The modelling process is first applied to a mock dataset of $O^+(^2P)$ production rates to determine whether the techniques used are robust to the noise inherent in the observations from the ASK instrument. The event from chapter 6 is analysed using the uniform flow parameterisation, and the recovered electric fields are discussed and compared against radar observations of the electric fields from the SuperDARN radar. The event from chapter 5 is then analysed using the sheared flow parameterisation.

7.2 Dynamics of the O^+ ion

The dynamics of the $O^+(^2P)$ ion are governed by a continuity equation, which has terms for production, quenching, emission, drift and diffusion:

$$\frac{dn}{dt} = q - \sum_j A_{ij} n - \sum_k \alpha_k n_k n - \nabla \cdot (n\mathbf{v}) - D\nabla^2 n \tag{7.1}$$

where n is the density of $O^+(^2P)$ ions, q is the production rate of $O^+(^2P)$ ions, A_{ij} is the Einstein coefficient for radiative transfer from state i to state j, n_k is the density of quenching species k, α_k is the rate coefficient for quenching by species k, $\mathbf{v}$ is the velocity of $O^+(^2P)$ ions and D is the diffusion coefficient.

Production of $O^+(^2P)$ ions occurs by impact ionization of neutral atomic oxygen by precipitating electrons through the following process:

$$e^- + O \longrightarrow 2e^- + O^+(^2P, ^2D, ^4S) \tag{7.2}$$

with the 18% of O^+ ion production into the ^2P state (Rees, 1982). The ^2P state is further split into the $J_{1/2}$ and $J_{3/2}$ angular momentum states.

There are two loss processes affecting the $O^+(^2P)$ ion: quenching and emission. Quenching is the dominant loss process at high atmospheric densities, and hence lower altitudes. When a particle is quenched, it loses energy through collisions with other particles. $O^+(^2P)$ ions are quenched by electrons, atomic oxygen and molecular nitrogen. These quenching reactions and rate coefficients given by Rees (1989) are shown in table 7.1. Of these rate coefficients, only those for quenching by electrons are used in this study. Further studies, both laboratory based and from airglow observations, have examined the rate coefficients for quenching by nitrogen and oxygen; these are listed in table 7.2. These studies show some disparity between the obtained quenching rates, particularly so for the oxygen rate coefficient obtained by Chang (1993). This was highlighted by Stephan (2003) to be due to a relationship, in their model, between the rate coefficient and solar flux. The nitrogen rate coefficient obtained by Stephan (2003) shows good agreement with experimentally measured rates, which are a factor two smaller than previous airglow results. In this work, the oxygen and nitrogen rate coefficients obtained

Table 7.1: Quenching reactions and rate coefficients for $O^+(^2P)$

Reaction	Coefficient (cm^{-3} s^{-1})
$O^+(^2P) + N_2 \longrightarrow N_2^+ + O$	4.8×10^{-10}
$O^+(^2P) + N_2 \longrightarrow N^+ + NO$	1.0×10^{-10}
$O^+(^2P) + O \longrightarrow O^+(^4S) + O$	5.2×10^{-11}
$O^+(^2P) + e^- \longrightarrow O^+(^4S) + e^-$	$4.0 \times 10^{-8}(T_e/300)^{-0.5}$
$O^+(^2P) + e^- \longrightarrow O^+(^2D) + e^-$	$1.5 \times 10^{-7}(T_e/300)^{-0.5}$

by Stephan (2003) are used due to the good agreement with previous experimental and airglow rates.

Table 7.2: Quenching rate co-efficients for $O^+(^2P)$ ions by nitrogen and oxygen

Oxygen (10^{-11} cm^3s^{-1})	Nitrogen (10^{-10} cm^3s^{-1})	Method	Study
5.2 ± 2.5	4.8 ± 1.4	Airglow	Rusch (1977)
–	$1.5 \pm 30\%$	Lab	Glosik (1978)
40 ± 19	3.4 ± 1.5	Airglow	Chang (1993)
–	$2.0 \pm 25\%$	Lab	Li (1997)
5.0 ± 3.4	1.8 ± 0.3	Airglow	Stephan (2003)

Emission occurs when $O^+(^2P)$ ions de-excite by spontaneously emitting a photon; there are no stimulated emissions. There are two radiative paths, (^2D) - (^2P) and (^4S) - (^2P), through which there are six possible transitions. These transitions are listed in table 7.3 and are depicted on an energy level diagram in figure 7.1. Chamberlain (1961) provides wavelengths, energy levels and Einstein coefficients for these transitions, however updated Einstein coefficients have been calculated by Zeippen (1987) and are used instead. These transitions form emission doublets at 733 nm, 732 nm and 247 nm, with only the 732 nm doublet observed by the ASK2 filter. The 732 nm doublet emission has contributions from both the $J_{1/2}$ and $J_{3/2}$ states, which means that equation 7.1 cannot be solved for the ^2P state as a whole and must instead be solved for each angular momentum state.

In isolation, the emission and quenching terms can be inverted to obtain an altitude dependent effective lifetime for the $O^+(^2P)$ ion (Dahlgren et al., 2009). This lifetime is

Table 7.3: Radiative transfers from the (^2P) state of the O^+ ion

Transition	Wavelength (nm)	Einstein coefficient (s^{-1})
$^2D_{3/2}$ - $^2P_{3/2}$	733.07	5.78×10^{-1}
$^2D_{3/2}$ - $^2P_{1/2}$	732.99	9.39×10^{-2}
$^2D_{5/2}$ - $^2P_{3/2}$	731.94	1.07×10^{-1}
$^2D_{5/2}$ - $^2P_{1/2}$	731.86	5.63×10^{-2}
$^4S_{3/2}$ - $^2P_{3/2}$	247.04	5.70×10^{-2}
$^4S_{3/2}$ - $^2P_{1/2}$	247.03	2.34×10^{-2}

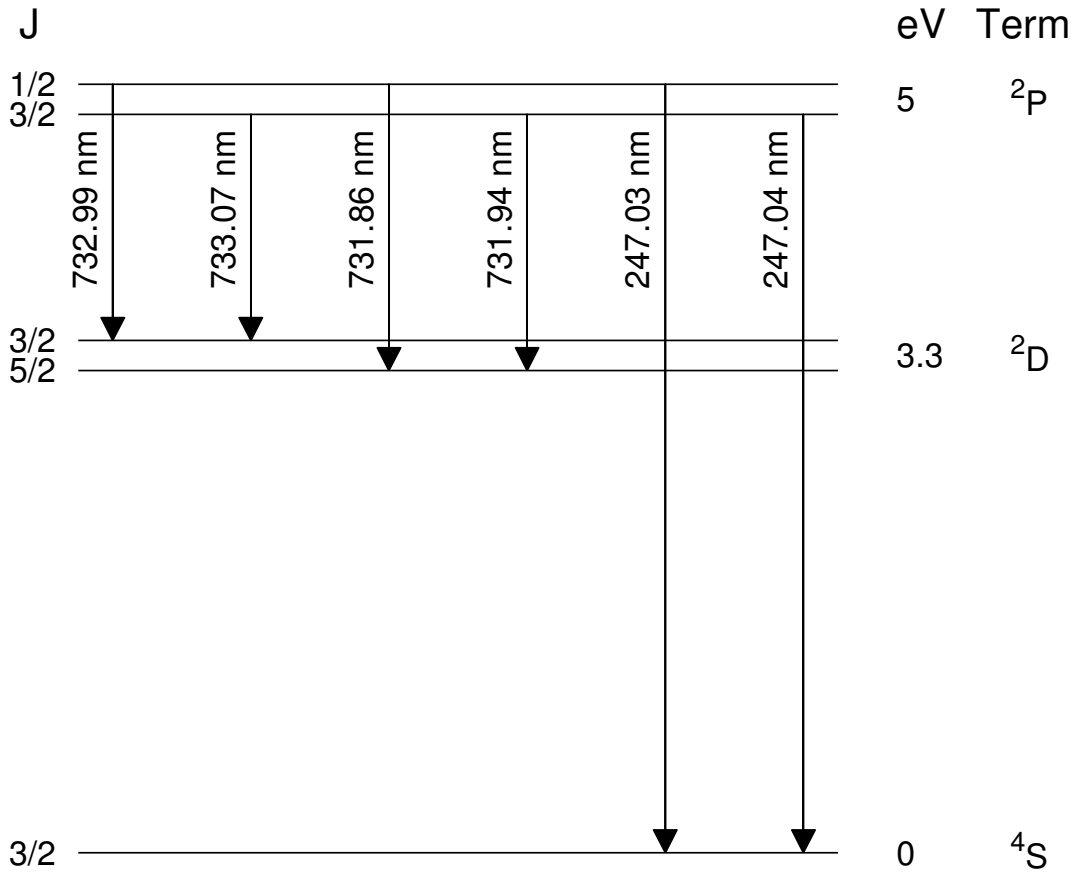

Figure 7.1: Energy level diagram for radiative transitions from the ^{2}P state of the O^+ ion

calculated using:

$$\tau_{eff}(z) = \frac{1}{\sum_k \alpha_k n_k(z) + \sum_j A_{ij}} \tag{7.3}$$

with the altitude dependence arising from the density profiles of the quenching species.

The diffusion term can be neglected for $O^+(^2P)$ ions. This is because collisions that would ordinarily redistribute the thermal motions of the ion instead cause the ion to quench. Perpendicular to the magnetic field, strong density gradients may exist. These are maintained by the magnetic field as any horizontal component of the thermal motion of an ion would result in a gyratory motion.

The third and fourth terms in equation 7.1 arise due to the flux term, $\nabla \cdot (n\mathbf{v})$, of the continuity equation. Rather than solving these terms explicitly to determine $\mathbf{v}$, the velocities in the modelled region are parameterised as discussed the next section (section 7.3).

7.3 The Flow model and flow parameterisations

Estimates of the velocities of $O^+(^2P)$ ions, and hence the electric fields, are obtained by searching for the free parameters, P, to a model brightness function that minimizes the error between observed and modelled brightnesses of emission from $O^+(^2P)$ ions as observed by the ASK2 camera. The model brightness function, I_{mod}, is given by:

$$I_{mod}(u, v, n(\vec{r}, P)) = f(n(\vec{r}, P)) \tag{7.4}$$

where u, and v are the image pixel co-ordinates, $n(\vec{r}, P)$ is the 3-D density distribution of $O^+(^2P)$ ions at position $\vec{r}$ from the ASK instrument obtained using the model parameters for the flow, P. Here f is the forward model that produces modelled images of the emission from the distribution $n(\vec{r}, P)$ using the projection methods described in section 4.3.

The 3-D density distribution of $O^+(^2P)$ ions is found by applying the continuity equation $O^+(^2P)$ ions (equation 7.1), using a flow velocity specified by the free-parameters, P. Two possible parameterisations of the flow velocity are used here; a uniform flow that is perpendicular to the magnetic field, and flow that is sheared across the auroral feature. For both cases, the unit basis vectors of the 3-D grid on which the distribution of $O^+(^2P)$ ions is being modelled are used as the orthogonal directions for the components of the flows. The orientation and resolutions of the 3-D grids used for each event are discussed in chapters 5 and 6 where the events were analysed, and information about the unit basis vectors can be found in section 4.3. Other, more complex parameterisations are possible, but are not explored further in this work.

Figure 7.2(a) shows flow parameters used in the case of a uniform flow. In this parameterisation the only free parameters are v_{e_1} and v_{e_2}, which are the components of the flow velocity along the unit basis vectors $\mathbf{e_1}$ and $\mathbf{e_2}$. These basis vectors are perpendicular to the magnetic field. The motion of ions parallel to the magnetic field is neglected as such motion is due to effects that are not of interest here, for example upwelling due to heating, or magnetic field aligned electric fields. This parameterisation is chosen to represent the flow which results from ions drifting in the presence of uniform, perpendicular electric and magnetic fields. For a given flow velocity $\vec{v}$, the electric field, $\vec{E}$, that is causing the drift is given by:

$$\vec{E} = -\vec{v} \times \vec{B} \tag{7.5}$$

where $\vec{B}$ is the magnetic field.

Figure 7.2(b) shows the layout and parameters used in the case of a sheared flow. In this parameterisation a separatrix, the dashed line in figure 7.2(b), divides the volume into two regions. This separatrix extends parallel to the magnetic field throughout the

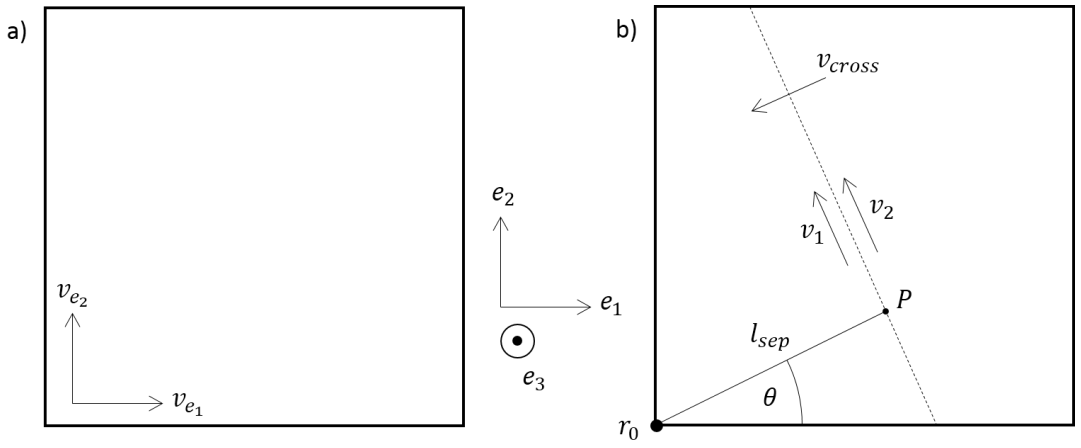

Figure 7.2: Diagrams for: (a) the 'uniform flow', and (b) the sheared flow, parameterisations for the $O^+(^2P)$ ion velocity used in this thesis. These diagrams show a cut perpendicular to the magnetic field through the 3-D volume in which the modelling of the $O^+(^2P)$ ion behaviour is performed. The black squares indicate the extent of the volume perpendicular to the magnetic field. The arrows outside the black squares indicate the directions of the basis vectors used in the setup of the 3-D modelling volume.

entire volume along the basis vector e_3. The position and orientation of the separatrix is determined by two parameters, θ and l_{sep}. The length l_{sep} is the distance between the reference point r_0 and the point P, which is the closest point along the separatrix to r_0. Here, r_0 is the bottom south-west vertex of the modelled volume. The angle θ describes the orientation of the line which connects r_0 and P. As this line is the shortest distance between r_0 and the separatrix, it will always intersect the separatrix at right angles. Therefore, as the angle θ changes, the orientation of the line between r_0 and P changes, and so too does the orientation of the separatrix. The motion of the plasma is parameterised using three drift velocities. Two of these, v_1 and v_2, lie parallel to, but on opposite sides of, the separatrix. A third velocity, v_{cross}, is used to allow plasma to move across the separatrix. The directions of the arrows in figure 7.2(b) indicate the direction of motion if the given velocity is positive. The rationale for the parameterisation used in the case of a sheared flow comes from both observations and modelling of kilometre (small) and sub-kilometre (fine) scale auroral arcs.

Otto and Birk (1992) developed and used a plasma-neutral gas model to show that a resistive instability, caused by a shear in the magnetic field, could produce small, but not fine scale auroral features. Further analysis (Birk and Otto, 1997), using a more developed plasma-neutral model that explicitly modelled the ionosphere (Birk and Otto, 1996), showed that such shear-induced resistive instabilities in the upper ionosphere can produce field-aligned electric potentials that exhibit fine scale structuring.

MHD simulations of magnetic reconnection have also shown the formation of fine scale structure within auroral current sheets and the development of intense currents along field-aligned potential drops (Otto and Birk, 1993; Lanchester et al., 1997). These

locations of these fine scale potentials and intense currents were interpreted as locations where fine scale aurora would be observed. Lanchester et al. (1997) also investigated the motion of plasma surrounding these fine scale features, finding a sheared flow with velocities in opposite directions on opposing sides of the fine scale potential structure.

Observations have also shown large horizontal electric fields ($>$ 100 mV m^{-1}) pointing towards auroral features, accompanied by large plasma velocities ($>$ a few km s^{-1}) tangential to the feature (Lanchester et al., 1996, 1998). Therefore, the modelled velocities of Lanchester et al. (1997) suggest electric fields, inferred from the $\mathbf{E} \times \mathbf{B}$ drift (equation 7.5), are directed towards the modelled potential structure. In this chapter, the event studied in chapter 5 is analysed using the sheared flow parameterisation to investigate these arc-directed electric fields by searching for tangential flows.

The optimal free parameters for the flow velocities are obtained by minimising an error function. The error function used here is the sum of squares difference between the observed and modelled images of emission from the $O^+(^2P)$ ions, with the modelled images obtained using equation 7.4, and is given by:

$$err(P) = \sum_{u,v} [I_{obs}(u,v) - I_{mod}(u,v,n(\vec{r},P))]^2 \tag{7.6}$$

where $I_{obs}(u,v)$ is the observed brightness at pixel (u,v) and $I_{mod}(u,v,n(\vec{r},P))$ is the modelled brightness at the same pixel (u,v), and $err(P)$ is the value of the error function for the parameters, P. The observed images (I_{obs}) come from ASK2 observations at 732.0 nm, and are processed to remove contaminating auroral emissions and background. A more complete description on the background and contamination removal is provided in the analysis of each event in section 7.4. Finally, electric fields are calculated using the magnetic field, obtained using either the IGRF-12 model for the event in chapter 5 or the ray method described in section 6.3.1 for the event in chapter 6 and flow vectors.

Not all observations of discrete aurora will be suitable for analysis using the flow model. The observed aurora is required to have sufficient structure and brightness to allow the key characteristics of the energy spectrum of the precipitating electrons to be found. Further, the nature of the altitude-dependent lifetime of the $O^+(^2P)$ ion requires that this precipitation be of sufficiently low energy to produce observable and trackable distributions of emission at 732.0 nm. Structure is required to allow the drift of the $O^+(^2P)$ ions to be determined. A uniform distribution of emission would be unsuitable as it would contain no features that can be tracked.

This requirement for structure is stronger for the sheared flow than for the uniform flow parameterisation. The uniform flow parameterisation should work as long as there is a discrete feature in the observations, even if this feature does not exhibit much structuring itself, because this method tracks the overall auroral feature rather than structure within the feature. The sheared flow parameterisation however requires structure to track

within the feature so that the resulting plasma motions on either side of the feature can be determined. Therefore the events studied in chapters 5 and 6 make ideal targets to test these flow parameterisations. The event in chapter 6 does not exhibit much structure within the observed feature, but the event does show clear evidence of an overall drift in the 732.0 nm emission. This event is therefore be suitable for testing the uniform flow method. The event in chapter 5 is more structured and exhibits clear structure, and variation in structure, making this event a suitable candidate to test the sheared flow method.

7.4 Results

7.4.1 Mock Dataset

A mock dataset of production rates and modelled images is first used to test whether the flow model is able to track the flows, and whether the modelling process can handle the noise present in the observations of the 732.0 nm emission obtained using the ASK instrument. As discussed in section 7.3, a key requirement in any observations to be analysed using the flow model is the presence of structure in the observed 732.0 nm emissions.

A set of production rates for a mock, structured auroral feature are produced. Gaussian energy spectra with a peak energy of a few hundred eV are used. Low energies are used here so that the altitude of peak production of $O^+(^2P)$ ions is high enough to ensure the $O^+(^2P)$ ions decay radiatively, and produce emission, rather than quench. These production rates are produced at a temporal resolution of 0.03125 s, which matches the ASK instrument framerate of 32 Hz. Figure 7.3 shows the height-integrated mock production rates at three timesteps from the start of the flow optimisation, separated by 0.5 s. The structure in this mock feature is modelled as a narrow, spatially varying sinusoid which has a feature thickness of a few hundred metres, an east-west horizontal extent of about 2 km, and is extended throughout the modelled region in the north-south direction.

The sinusoidal feature and associated production rates move eastward and southward. As the feature moves east, $O^+(^2P)$ ions are produced over an extended region in the east-west direction, resulting in a 3-D distribution of $O^+(^2P)$ ions. This distribution is subjected to the mock flow velocities that surround the feature. In these tests the sheared flow parameterisation is used. The separatrix is placed at the centre of the feature, outlines by the production rates shown in figure 7.3, and moves with the feature. The l_{sep} parameter is therefore a function of the eastward speed of the feature and time, and the θ parameter is fixed to 0 radians. Flow velocities of $v_1 = -1$ km s^{-1} to the west of the separatrix, $v_2 = 0.5$ km s^{-1} to the east of the separatrix, and $v_{cross} = 0.5$ km s^{-1}

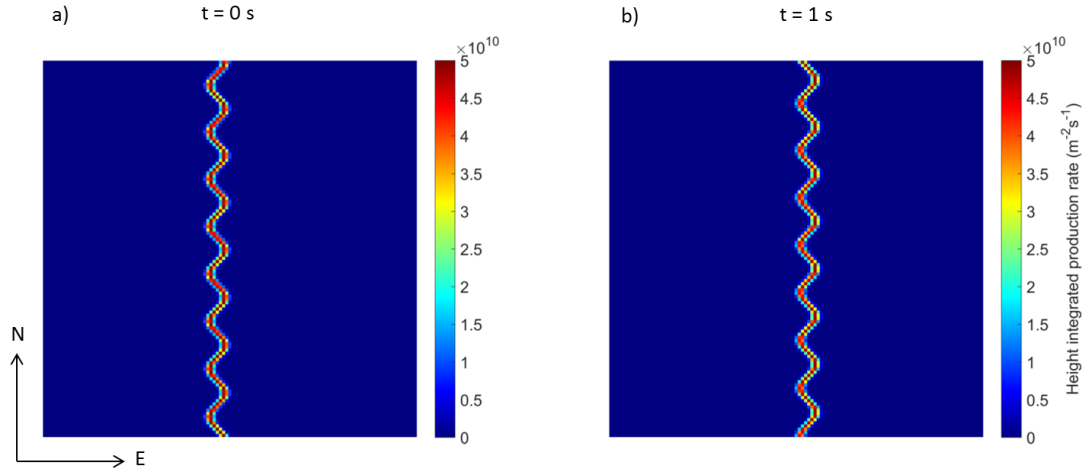

Figure 7.3: Height integrated mock production rates for the $O^+(^2P)$ ion. The horizontal extent of the modelled region is 30 km by 30 km and the arrows indicate the directions of north (N) and east (E).

across the separatrix are used. The orientation of the separatrix results in v_1 being directed southward, v_2 northward, and v_{cross} eastward.

The model is then iterated in time using the described flow parameters to generate an initial distribution of $O^+(^2P)$ ions to be tracked. To test the optimisation process, modelled images of the emission from this distribution are produced. As a set of images is required, the model is further iterated using the known flow parameters and a modelled image is produced from the distribution of $O^+(^2P)$ ions at each timestep. Noise can then be added to the modelled images to simulate observations acquired using the ASK instrument. A histogram analysis of observations from the ASK2 camera at 732.0 nm show that the noise obeys a brightness-dependent normal distribution. Noisy modelled images are obtained using the following equation:

$$I(u,v)_{noisy} = I(u,v)_{model} + 4 \times I(u,v)^{0.5} \times N(0,1) \tag{7.7}$$

where $I(u,v)_{noisy}$ and $I(u,v)_{model}$ are the brightnesses at pixel (u,v) in the noisy and ideal images respectively. The factor of four is obtained experimentally from analysis of the images from the ASK2 camera at 732.0 nm. These images, noisy or otherwise, are hereafter referred to as the mock observed images.

The distribution of $O^+(^2P)$ ions is then reverted back to the initial distribution and the tracking part of the model is then used to search for the optimal flow parameters. All five parameters, l_{sep}, θ, v_1, v_2 and v_{cross}, are allowed to vary. Initial guesses for l_{sep} and θ are estimated using a moment analysis on the height-integrated production rates to determine the position of the separatrix. Initial guesses for the flow velocities are obtained by running a combination of flow velocities through the model and selecting the velocities which minimise the error, as calculated using equation 7.6, as the input

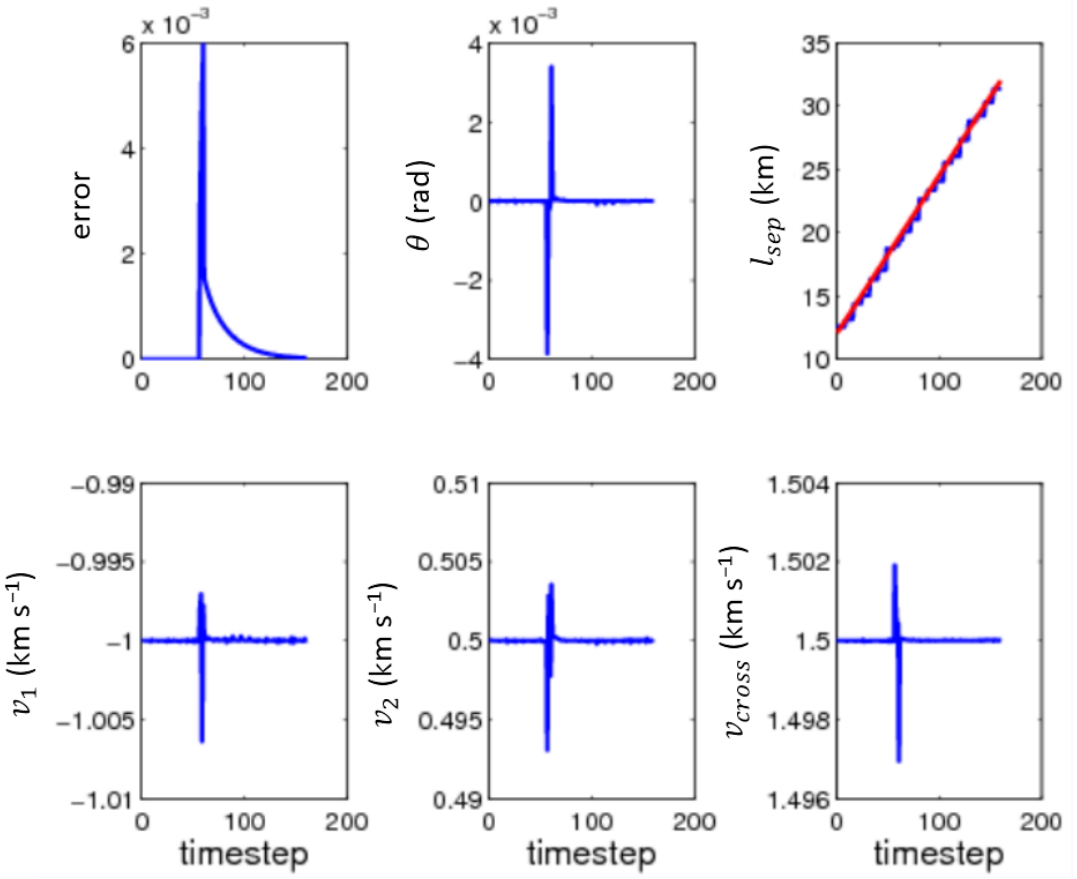

Figure 7.4: Recovered flow parameters for the test of the flow model using mock observed images with no noise. Each timestep corresponds to an interval of 0.03125 s. The red line indicates the value of the flow parameter that should have been recovered at each timestep.

parameters to the model. The combinations of flow velocities use values in the range $-5\ km\ s^{-1} \leq v \leq +5\ km\ s^{-1}$ and a step of 1 km s^{-1}. The model then further optimises the parameters of the flow using the Nelder-Mead optimisation (Nelder and Mead, 1965). For subsequent timesteps, the optimal parameters at the current timestep are used as the 'initial guess' for the parameters at the next timestep.

Figure 7.4 shows the results of the optimisation if no noise is added the modelled images. The timestep used in the modelling here is 0.03125 s, which corresponds to the commonly used framerate of 32 Hz for the ASK instrument. These results therefore span a time interval of approximately 5 s, which is the maximum lifetime of the $O^+(^2P)$ ion. All flow parameters are well-tracked, albeit with a sudden increase in the error between the modelled and mock observed images around timestep 60. This increase in error is accompanied by errors in the optimal flow parameters, though these parameters stabilise to their correct values in the following timesteps. The stepwise changes in the l_{sep} parameter are a consequence of the finite resolution of the modelled 3-D volume.

This modelling process is then repeated using noisy mock observed images. These noisy

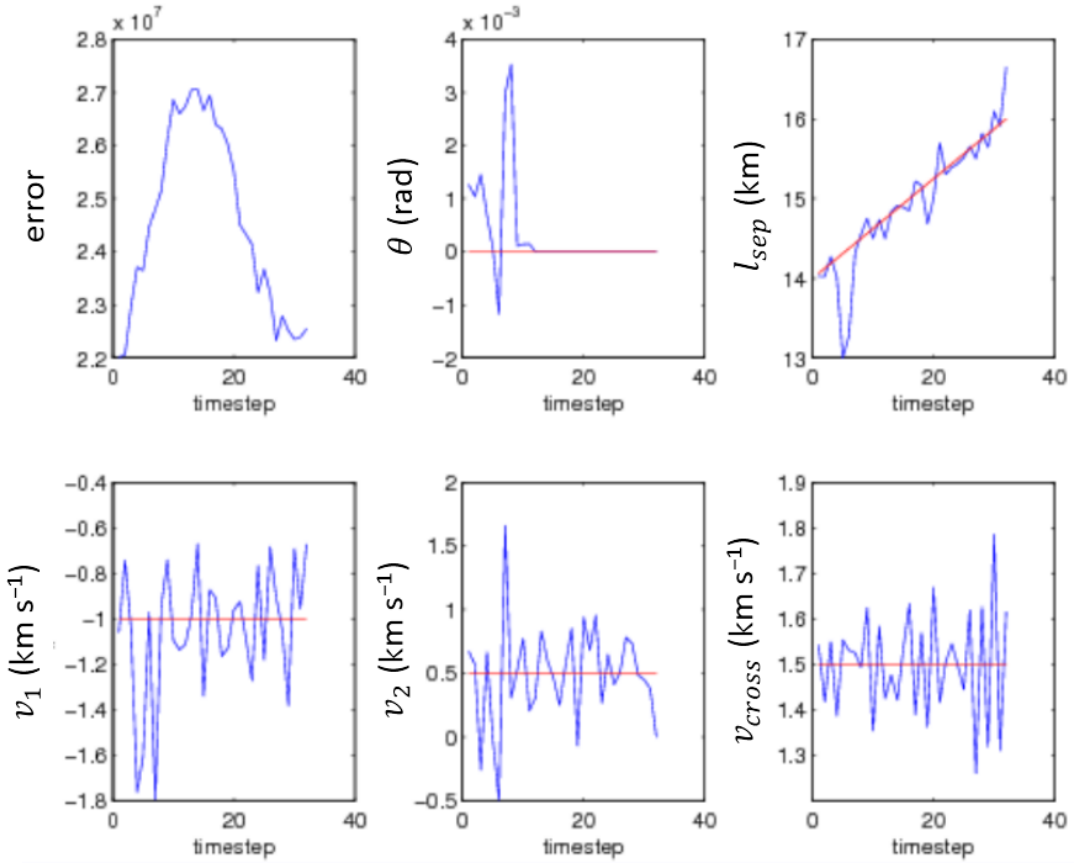

Figure 7.5: Recovered flow parameters for the test of the flow model using noisy mock observed images. Each timestep corresponds to an interval of 0.03125 s. The red line indicates the value of the flow parameter that should have been recovered at each timestep.

images are filtered using a combination of median and Weiner filtering to remove noise but preserve sharp brightness gradients in the images. The parameters and timestep are identical to those used for the non-noisy results, however the noisy model run lasts only one second. Figure 7.5 shows the results of the optimisation if noise is added to the mock observed images. The red lines in the plots of figure 7.5 indicate the input flow parameters used to produce the non-noisy modelled images. There are large variations timestep-to-timestep in the flow parameters recovered from the noisy images, with some parameters, for example v_2, exhibiting much greater variation than others, such as v_1 or v_{cross}. The parameters that describe the position of the separatrix were more robust to the noise, as can be seen from the plots in figure 7.5 for the l_{sep} and θ parameters.

7.4.2 Uniform Flow

The event studied in chapter 6 is analysed using the uniform flow parameterisation described in section 7.3. Production rates for the $O^+(^2P)$ ions are obtained using the Southampton ion-chemistry model and the electron energy spectra obtained in chapter 6.

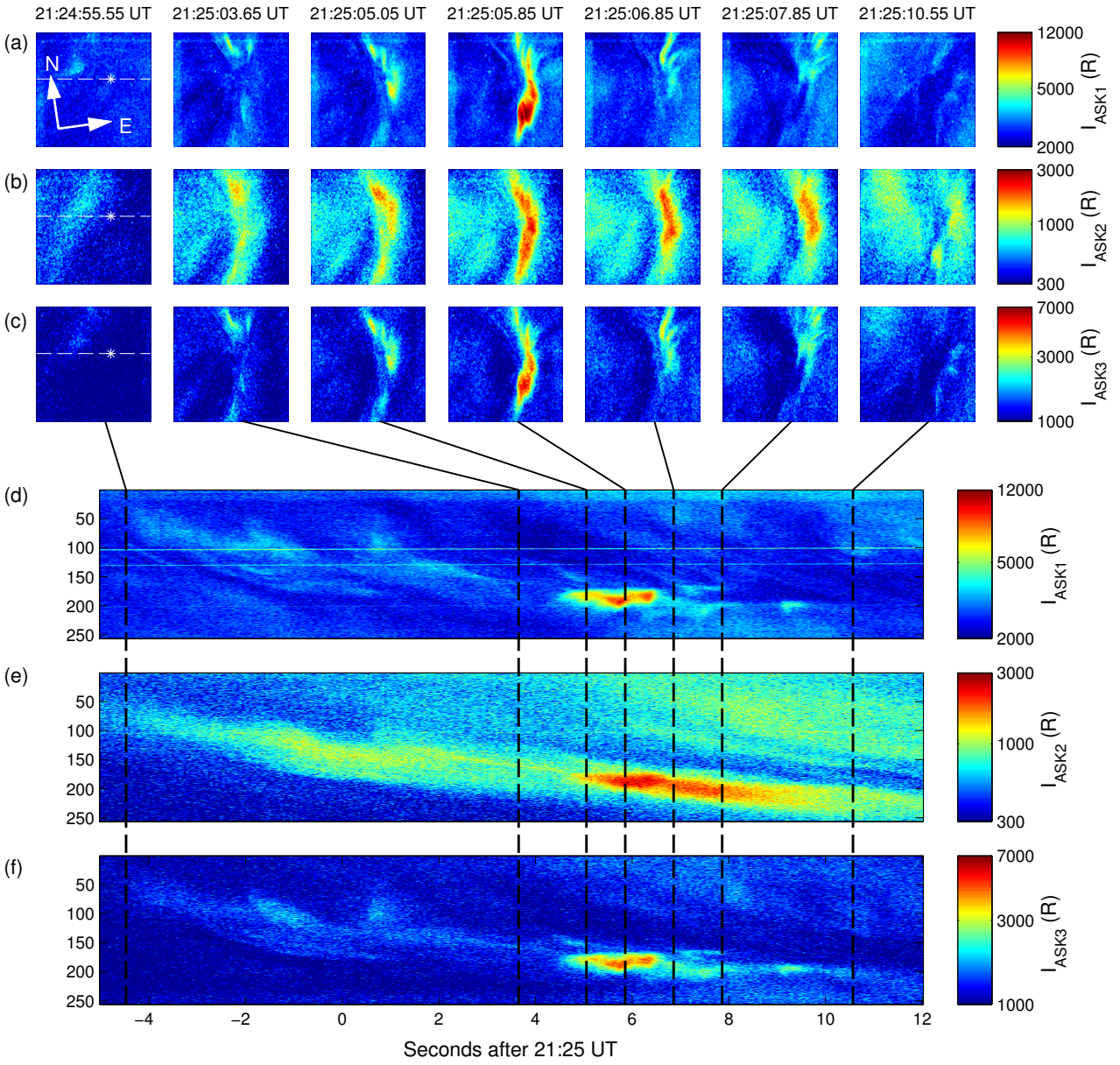

Figure 7.6: (a), (b) and (c) Images of the auroral brightness observed by ASK1 (673.0 nm), ASK2 (732.0 nm) and ASK3 (777.4 nm) respectively. (d), (e) and (f) Stackplots of almost east-west aligned cuts, 5 pixels wide, through images from ASK1 (673.0 nm), ASK2 (732.0 nm), and ASK3 (777.4 nm) respectively. West is at the top and east is at the bottom of the vertical axis of each stackplot. The black lines link the images to the respective times in the stackplot. Logarithmic intensity scales are used to highlight both bright and faint features throughout the event.

Figure 7.6 shows observations and west-east aligned stackplots from the event studied in chapter 6 for all three ASK cameras, which were observing at 673.0 nm, 732.0 nm, and 777.4 nm. This event occurred shortly after 21:25 UT, during an auroral storm caused by the Earth entering a solar wind stream with negative B_z at around 20 UT. These observations have been background subtracted, but contaminating auroral emission from the (5,3) band of the N_2 1PG band system has not been removed from the 732.0 nm emissions. Suitable backgrounds for each emission are found by searching the 20 minutes either side of the observed event to find periods with no auroral activity. Images for each wavelength from these times are then averaged over 2 s and the median brightness of these averaged images is found. The lowest values of the image brightness for each observed wavelength are then used as the minimum background, which is then subtracted from each analysed image.

Panels a–c show false colour images of the observed auroral forms in all three observed wavelengths, over a 15 s interval. Panels d–f are stack plots of west-east slices across the feature through the magnetic zenith for all three wavelengths. West is at the top of the vertical axis, and east is at the bottom, in the stack plots, and the position of the slice through the images is marked on the first image of panels a–c. The images of emission at 673.0 nm and 777.4 nm (panels (a) and (c)) indicate the presence of electron precipitation, which begins with a diffuse aurora that exhibits no distinguishable features. Over the next 10 seconds a north-south aligned filament forms close to the magnetic zenith. At 21:25:04 UT the aurora brightens significantly over a two second interval, rising from 5 kR to a peak brightness of 12 kR in the 673.0 nm emission and from 2 kR to 6 kR in the 777.4 nm emission at 21:25:06.5 UT. The auroral brightness then falls to about 5 kR in ASK1 and 3 kR in ASK3 at 21:25:08 UT, then further abates over the next few seconds until the feature is no longer distinguishable.

The brightnesses of the 732.0 nm emission do not exhibit the same behaviour as 673.0 nm and 777.4 nm emissions; structures appear wider and last longer in the 732.0 nm emission. After the intensification at 21:25:06.5 UT, the 732.0 nm brightness does not fall as rapidly as that of either the 673.0 nm or 777.4 nm brightness. These effects are both the result of the metastable nature of the $O^+(^2P)$ ion and can be clearly seen in the 732.0 nm slices shown in figure 7.6(e). The 732.0 nm emissions continue for up to 5 seconds after the prompt emissions diminish with an apparent eastward motion of the emission, evidenced by the downward motion in the stackplot (e) after the prompt emissions diminish. This motion is not caused by motion of the source, which is shown in the prompt emissions of the 673.0 nm and 777.4 nm emissions, but is instead a result of the E×B drift caused by horizontal electric fields in the ionosphere, and which is observed due to the finite lifetime of the emissions from the metastable $O^+(^2P)$ ion.

The stackplots also show that fainter emissions from the discrete feature persist for approximately 4 s after 21:25:06.5 UT, indicating that electron precipitation is still occurring, albeit with a reduced intensity. This precipitation produces $O^+(^2P)$ ions

which render the application of other flow methods, such as that of Dahlgren et al. (2009), impossible as the effects of precipitation and drift cannot be disentangled. These observations highlight both the long-lived nature of the 732.0 nm emission, and the necessity to consider the production and motion of the $O^+(^2P)$ ion separately. Only by fully modelling the spatio-temporal distribution and evolution of the $O^+(^2P)$ ion to account for the production, loss and drift, can the effects of production and drift be distinguished.

Prior to application of the flow method, the contaminating auroral emission from the N_2 1PG (5,3) band in the 732.0 nm emission must be removed. The observed emission at 673.0 nm also contains emission from the same band system, albeit from the (5,2), (4,1) and (3,0) bands. The brightness of the 673.0 nm emission can therefore be used to estimate the brightness of the (5,3) band emission for removal from the observed images at 732.0 nm. The method described in Spry et al. (2014) is used. Synthetic spectra of emission from the bands of the N_2 1PG band system which contribute to the observed emissions are produced (Jokiaho et al., 2008). The total emission brightnesses, as observed through the 732 nm and 673 nm filters on the ASK instrument, are calculated by convolving the band intensities with the filter transmission functions, both of which are wavelength-dependent, and integrating. The ratio, R_{mod}, of these two modelled emission brightnesses is given by:

$$R_{mod} = \frac{I_{732}}{I_{673}} \tag{7.8}$$

where I_{732} and I_{673} are the emissions brightnesses of the N_2 1PG bands observed through the 732.0 nm and 673.0 nm filters on the ASK instrument. The temperature of the parent N_2 molecule determines the relative production into each band of the N_2 1PG band system, therefore the modelled ratio of N_2 1PG band emission at 732 nm to 673 nm is dependent on the neutral temperature, which is obtained from the MSIS-E90 atmospheric model. The neutral temperature is taken at the altitude of peak production. However the energies in the event studied here, which range from 1-5 keV, give a large range of altitudes of peak production, between approximately 120-170 km, which results in a range of modelled ratios for R, between 0.03 and 0.045. An energy of 2 keV, which is consistent with the energy of most of the large discrete feature (see figure 6.7(b)) is used for this event, which results in a modelled ratio of $R = 0.043$. Decontaminated images of the 732.0 nm emission are produced by subtracting this fraction of the 673.0 nm emission from the 732.0 nm emission.

The flow model is run for a 15 second interval, starting at 21:24:57.50 UT, that includes times before, during and after the arc brightening. A timestep of 0.1 s, which is twice the interval between the ASK observations, is used. This model timestep is chosen to try and minimise the effect of the variations in flow parameters seen in the noisy test case (see figure 7.5). The modelled volume is unchanged from the analysis of the prompt emissions for this event presented in chapter 6. For the first five seconds the

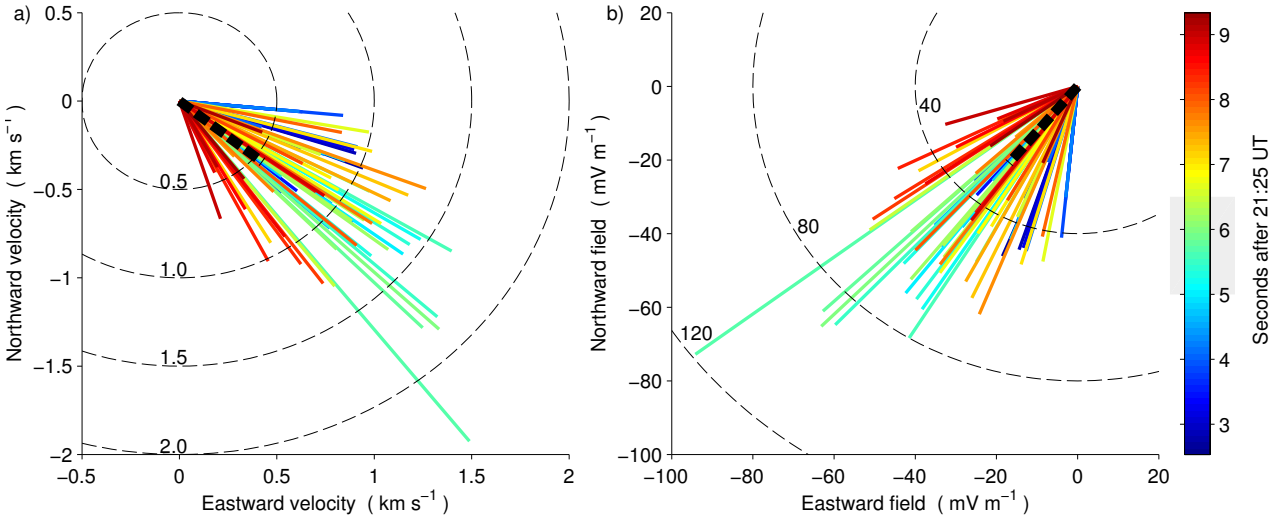

Figure 7.7: Magnitudes and directions of the best-fit plasma velocities (a) and the inferred electric fields (b). The dashed arcs are magnitude of velocity contours. The thick dot-dashed line is an average of the magnitudes and directions of the four measurements in table 7.4. The colour of each line indicates the time of the velocity or field and the shaded region of the colourbar indicates when the arc was intensified.

model is run without the optimization, using a plasma velocity of zero, to generate an initial distribution of $O^+(^2P)$ ions to be tracked. As the lifetime of the $O^+(^2P)$ ion is five seconds, any ions produced more than five seconds before the event studied here are irrelevant. In the ten seconds following the five second warm-up, the optimization is active and the model searches for the flow parameters at each timestep using the methods described in section 7.3.

Figure 7.7(a) shows the recovered velocities. The velocities all have southward and eastward components. The times when the arc brightness is intensified is indicated by the shaded region on the colourbar. The thick dot-dashed line is the average of the radar measurements. Both before and after the feature intensifies, the recovered velocities are between 0.4 and 1.2 kms^{-1}. When the feature is intensified the velocities are larger, with a peak velocity of 2.4 kms^{-1}. Figure 7.7(b) shows a similar pattern in the inferred electric fields, with enhanced electric fields when the arc is brighter. These fields are calculated from the E×B drift (equation 7.5) using the magnitude of the magnetic field at the altitude of peak emission. The magnitude of the magnetic field at 200 km altitude within the ASK field of view is calculated using the IGRF-12 geomagnetic model, and found to be 48.9 μT. The inferred electric fields are found to have southward and westward components and have magnitudes of between 20 and 120 mVm^{-1}.

A sequence of modelled images of the 732.0 nm emission from the convected distribution of $O^+(^2P)$ ions are shown in figure 7.8. The corresponding observations of the background subtracted and decontaminated 732.0 nm emission are shown in figure 7.9.

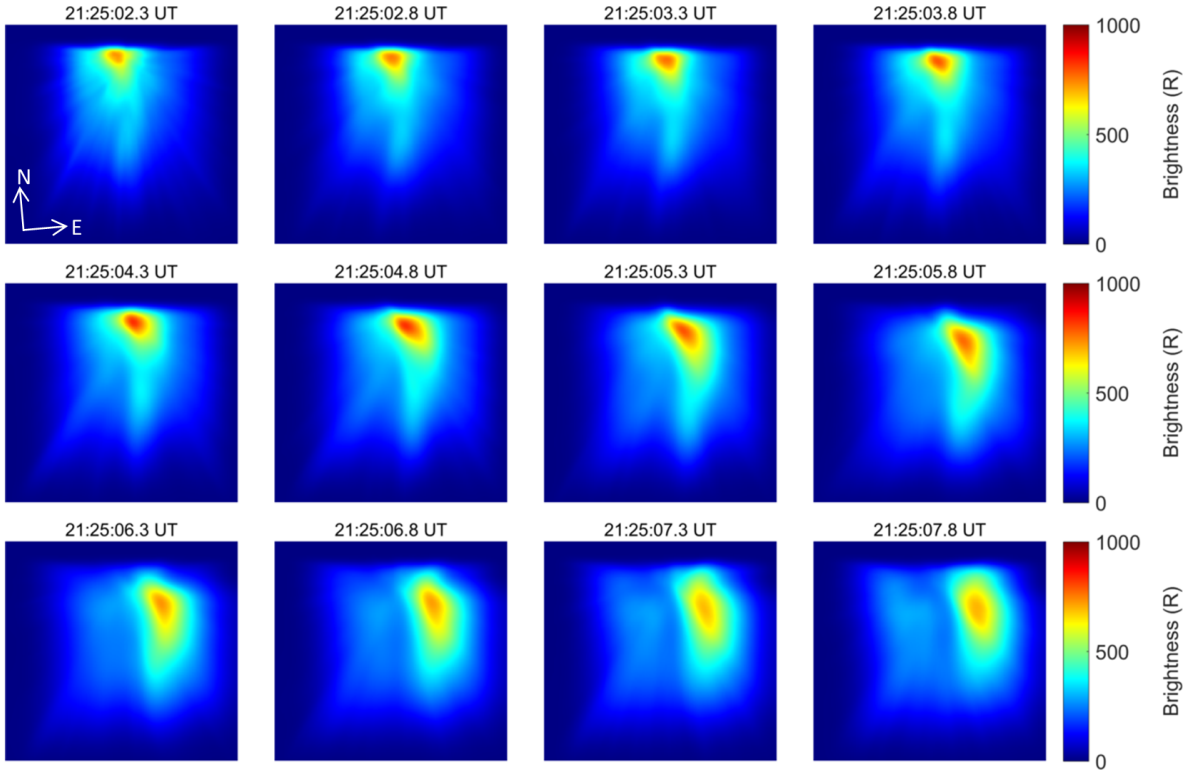

Figure 7.8: A sequence of modelled images of the 732.0 nm emission from the distribution of ions that convects with the velocities given in figure 7.7(a).

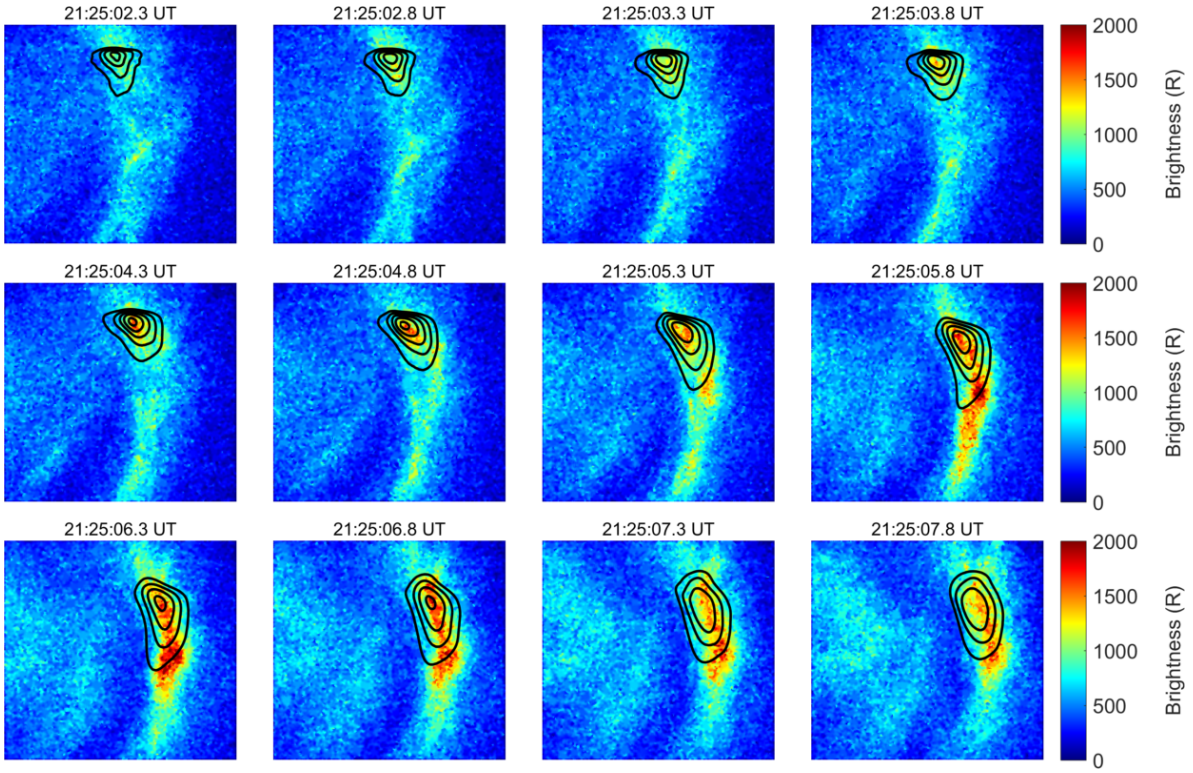

Figure 7.9: A sequence of observed images of the 732.0 nm emission. The black lines are brightness contours from 400 R to 800 R at 100 R intervals.

Table 7.4: Merged velocities, for the numbered observations in figure 7.10, obtained from the Hankasalmi and Pykkvibaer radars between 21:24 UT and 21:26 UT on 9 November 2006

Observation	Magnetic Latitude	Magnetic Longitude	Velocity (ms^{-1})	Azimuth angle
1	67.5	100.4	621	126.8
2	67.5	103.0	622	137.8
3	66.5	101.3	430	154.5
4	66.5	103.8	639	141.0

Contours of modelled brightness are superimposed on the observed images showing that the modelled images capture the structure of the observed images well. The brightness of the modelled images are underestimated by up to 50%.

These recovered velocities are compared to radar observations of plasma velocity obtained using the SuperDARN radars. Observations of the line-of-sight plasma drift in the region above northern Scandinavia from two radars at Pykkvibaer, Iceland, and Hankasalmi, Finland are used. At the time of the event studied here, the radars were operating in common time mode, where each radar performs a sweep of its field of view every minute. A sweep is comprised of 16 separate beams, separated in azimuth by 3.24 degrees. The radar measures the Doppler shift of the backscatter from irregularities in plasma density along each beam sequentially each minute. Each beam is separated into 75 range gates, each with a range of 45 km. Where overlapping measurements from multiple radar exist, the data can be combined to give the horizontal plasma velocity (Ruohoniemi and Baker, 1998).

Figure 7.10 shows the magnitudes and directions of the plasma velocities, as measured by the two SuperDARN radars discussed above, during the interval that contains the event analysed here. Magnetic coordinates, plasma velocities and azimuthal angles of the observations labelled 1 through 4 in this figure are presented in table 7.4. The SuperDARN measurements of the plasma velocity and direction are shown in Figure 7.7 by the black line. All four labelled velocities have southward and eastward components and a narrow spread in direction, with azimuth angles of between 127 and 154 degrees. The velocities labelled 1, 2 and 4 have similar magnitudes, between 621 and 639 ms^{-1}, but the velocity labelled 3 is lower than the other three, at 430 ms^{-1}. The velocities and directions of the plasma flow suggest that there is a motion of plasma southward and eastward with a velocity of around 600 ms^{-1}. The plasma velocities extracted from the flow model are consistent in direction with the SuperDARN observations but have larger magnitudes, even more so during the time when the brightness of the discrete auroral feature was high.

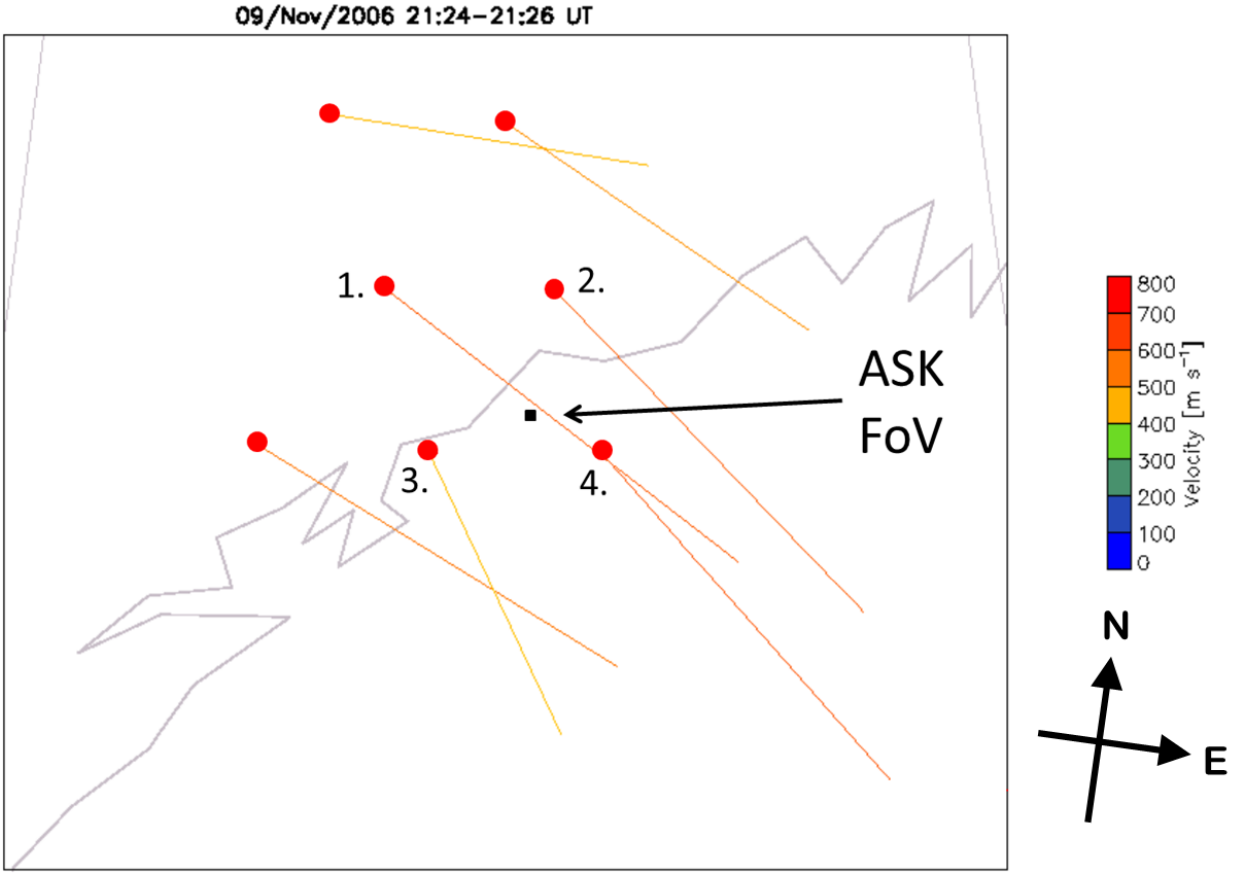

Figure 7.10: Merged plasma velocities over northern Scandinavia obtained between 21:24 and 21:26 UT on 9 November 2006. The grey jagged line is the coastline of Norway. The length and colour of the lines indicate the magnitude of the plasma velocities. The red dots indicate the position of the measured velocities and the direction of the velocity is given by the direction of the line from the dot. The black square indicates the approximate size and location of the ASK field of view at 200 km altitude. The arrows labelled 'N' and 'E' indicate the directions of north and east at the location of the ASK field of view.

7.4.3 Sheared Flow

Results from the analysis of the event on 9 November 2006 in section 7.4.2 show that the flow model is capable of tracking the motion of the emitting $O^+(^2P)$ ions using a simple parameterisation of the flow velocity. However, the sheared flow parameterisation is not attempted on this event because it does not exhibit sufficient structure in the 732.0 nm emission for the shear method to work. Instead, the shear flow method is applied to the event at 19:32 UT on 12 December 2006, analysed in chapter 5, to investigate the electrodynamics of auroral features.

Figure 7.11 shows a sequence of filtered, background subtracted and decontaminated images of the observed 732.0 nm emission. A suitable background for this event is determined in the same way as for the uniform flow event discussed in section 7.4.2. However, the decontamination of the 732.0 nm emission is performed using a slightly

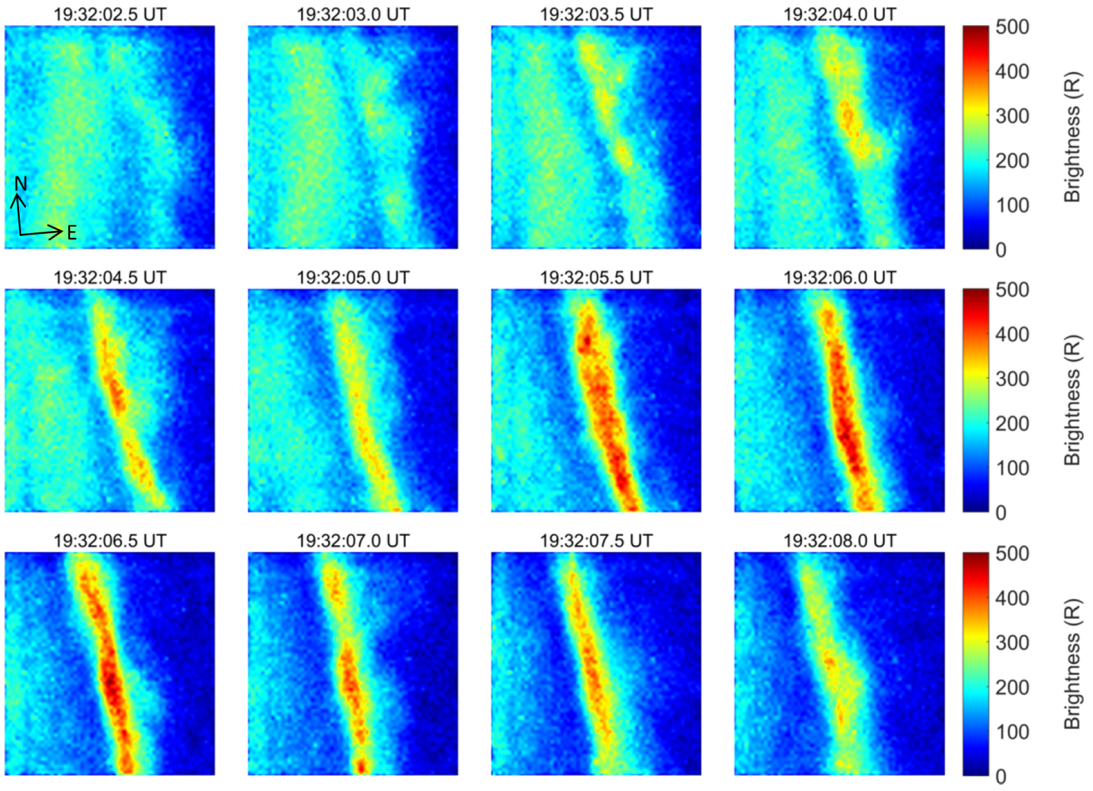

Figure 7.11: A sequence of processed images of the 732.0 nm emission observed by ASK during the event on 12 December 2006 at 0.5 s resolution. The processing filters out stars, reduces the effect of noise and removes any background or contaminating emissions.

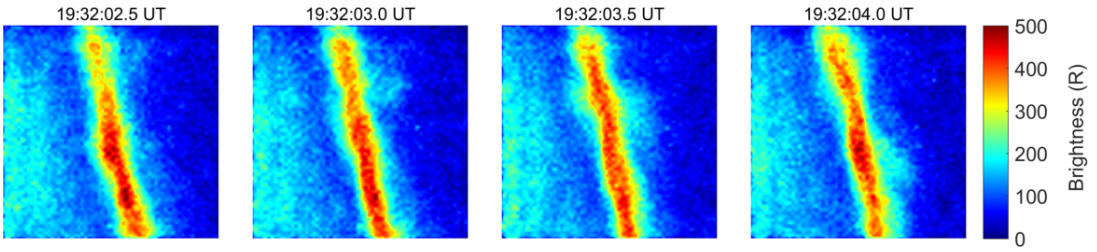

Figure 7.12: A sequence of processed images of the 732.0 nm emission at 0.125 s resolution showing the presence of fine structure within the arc.

different method to the uniform flow event because the 673.0 nm emission is not observed for this event. Instead, modelled images of the prompt 673.0 nm emission are produced, using the methods described in chapter 5. In the absence of observations of the 673.0 nm emission, these modelled images are instead used to remove the contaminating (5,3) band emission from the observed 732.0 nm emission. The peak energy of the electron precipitation during this event is around 5 keV, which yields a peak emission height of around 120 km, and a modelled ratio, R, of 0.029.

Structure present in the auroral arc shown in figure 7.11 can be more clearly seen at higher time resolutions. The short sequence of images shown in figure 7.12 shows the fine structure present in the arc on shorter timescales, 0.125 s compared to 0.5 s. Small

regions of emission, so-called 'Ruffs' (Dahlgren et al., 2011), appear to counter-flow along the edges of the arc, with the ruff on the eastern side of the arc moving northward and the ruff on the western side of the arc moving southward. This fine scale structure provided by these ruffs is vital for the flow model to be able to track the motion of the emitting plasma.

For this event the flow model is run for a 7.5 second interval, starting at 19:32:00.5 UT, which contains the structured auroral feature. A timestep of 0.125 s is used here, a multiple of four of the ASK framerate of this event. As in the uniform flow case, this timestep is chosen to reduce the effect of image noise on the recovered flow parameters. The production rates of $O^+(^2P)$ ions are found using the electron energy spectra obtained in chapter 5. The production rates from the first 2 seconds, from 19:32:00.5 until 19:32.02.5 UT, of the modelled interval are averaged to allow the production of an initial distribution of $O^+(^2P)$ ions to track. This initial distribution is obtained by running the flow model with the averaged production rates and no plasma convection for 10 seconds to ensure a steady-state solution has been reached.

The flow model is then run for a further 5.5 seconds, covering the interval from 2.5 s until 8 s after 19:32 UT, using the sheared flow parameterisation to determine the optimal flow parameters. To reduce the number of free-parameters in the optimisation the l_{sep} and θ parameters, which control the position of the separatrix, are determined using the production rates at each modelled timestep. An analysis using image moments is applied to plots of the height-integrated production rates to find the position of a line which bisects the production rates. Figure 7.13 shows the result of such an analysis, with the separatrix clearly placed along the centre of the feature as defined by the production rates. The position and orientation of the separatrix remains roughly the same throughout the event.

Using figure 7.13 as a reference, and using the layout and orientation of the sheared flow parameterisation shown in figure 7.2(b), the velocity of the plasma to the east of the arc is referred to as the 'eastern' velocity, likewise the velocity of the plasma to the west of the arc is referred to as the 'western' velocity. Positive values of the eastern or western velocities indicate a roughly northward motion, whereas negative values indicate a southward motion. The velocity of plasma across the arc is referred to as the 'cross-arc' velocity, and positive values indicate a roughly eastward motion.

Figure 7.14 shows the recovered plasma velocities for this event. At the initial timestep, the plasma velocities are large (>10 km s^{-1}). These large initial velocities are likely due to the model moving the initial distribution of $O^+(^2P)$ ions, which is formed assuming no plasma motion, to better match the observed emission from this distribution, which may be moving. The eastern velocity is directed southward throughout, falls to a few km s^{-1} for the first second of the analysis. After the first second it reduces to, and remains at, zero for the remainder of the event. The western velocity is also directed southward

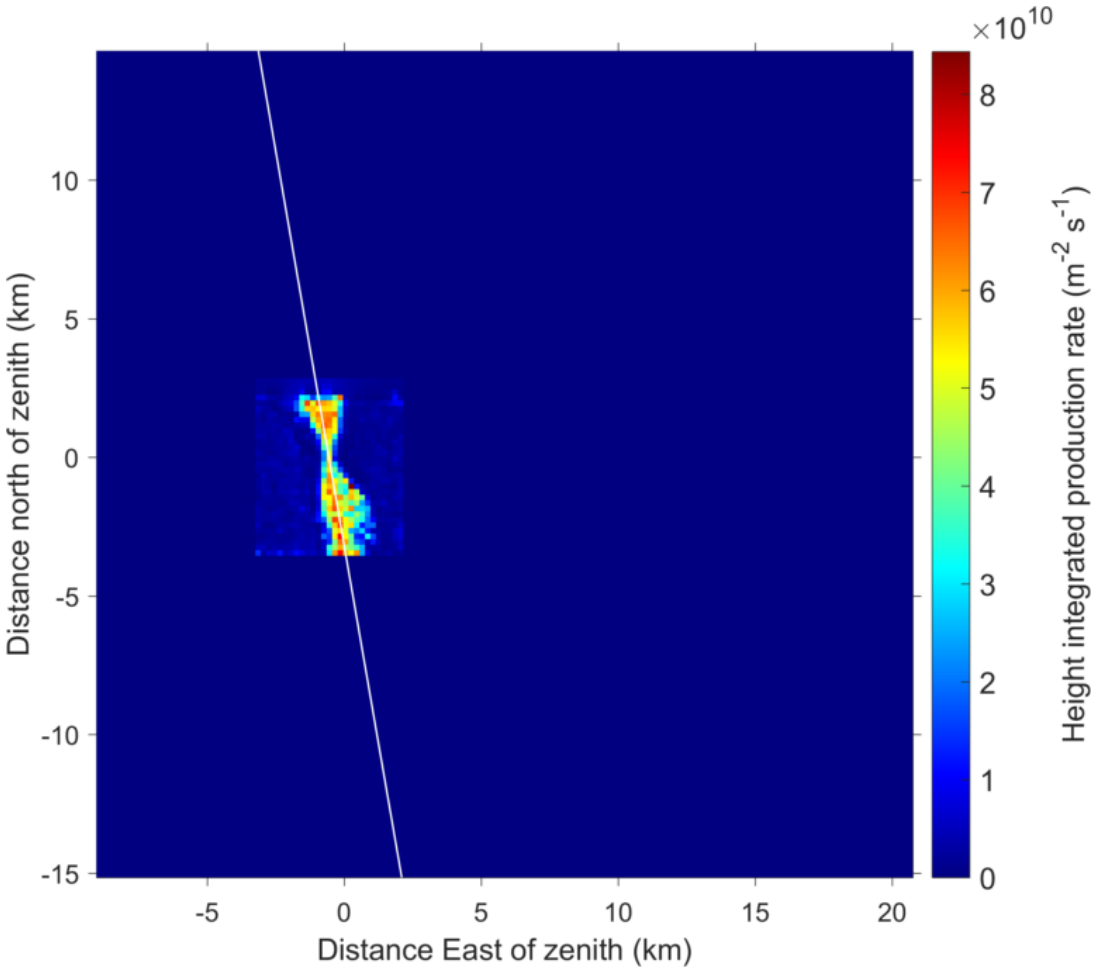

Figure 7.13: Height-integrated production rates for the $O^+(^2P)$ ion at 19:32:06.5 UT. The straight red line indicates the position of the separatrix at this timestep in the flow model.

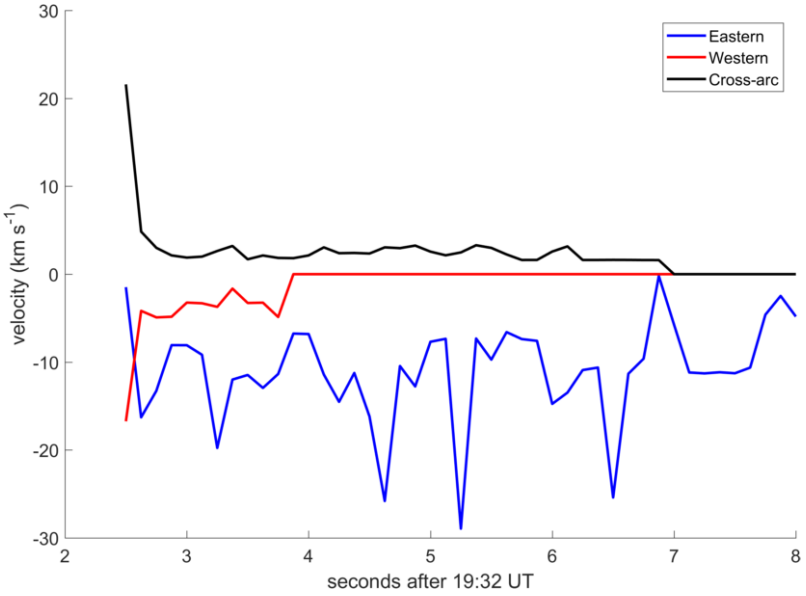

Figure 7.14: A time-series of the optimal flow velocities from the event at 19:32 UT on 12 December 2006.

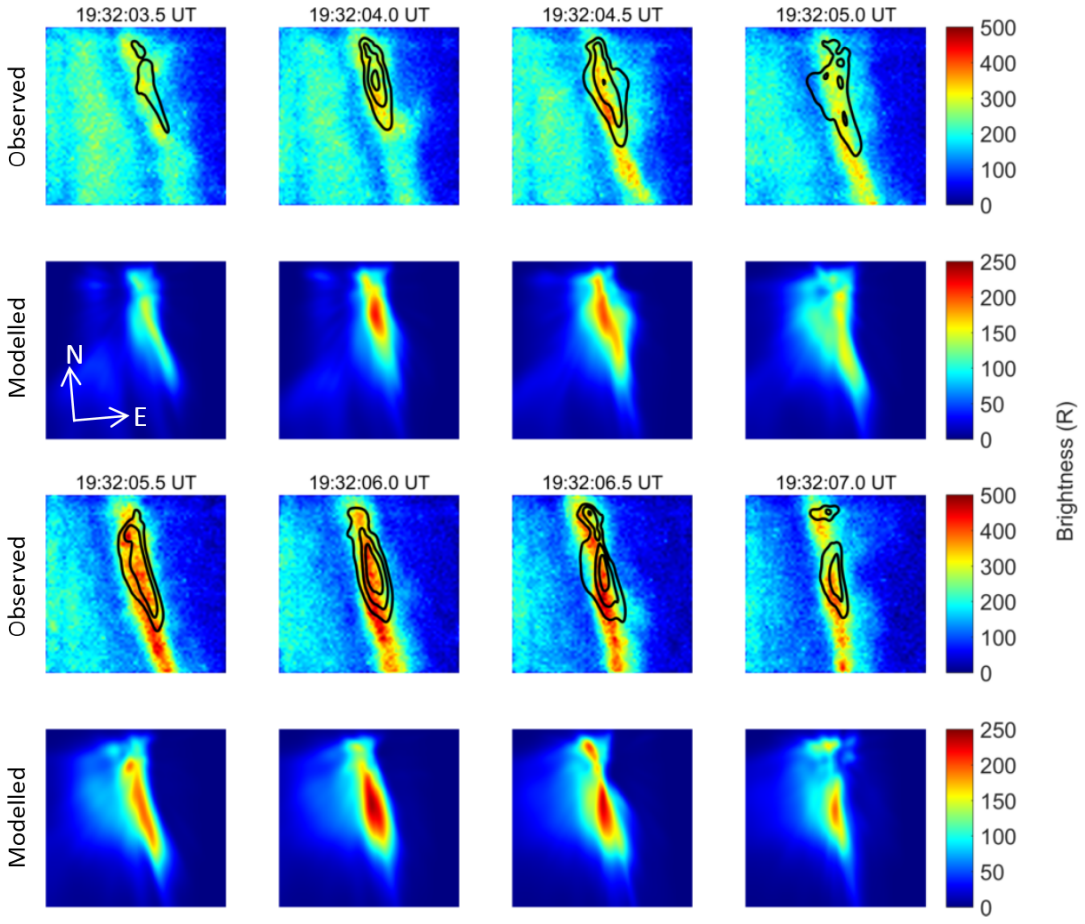

Figure 7.15: A time-series of observed and modelled images of the 732.0 nm emission. The black lines are brightness contours of the modelled emission at intervals of 50 R starting at 100 R. The directions of the arrows labelled 'N' and 'E' indicate the directions of north and east respectively.

throughout the event and exhibits large fluctions in velocity between 1 and 29 km s^{-1}. The cross-arc velocity is directed eastward and remains roughly constant, at 2-3 km $s^{-}1$, for the majority of the event before falling to zero at 19:32:07 UT, and remaining zero for the rest of the analysed interval.

These velocities should be interpreted in the context of the modelled images of the 732.0 nm emission, which are shown in figure 7.15. The modelled images show the large scale structure is reasonably well-modelled and at times, such as 4.0 s, 5.5 s and 6.0 s, the finer scale structure is also well modelled. There are however some times where the structure is not well modelled, such as 5.0 s or 7.0 s. Similarly to the modelled images for the uniform flow event, the brightnesses of the modelled images here are also significantly undermodelled.

7.5 Discussion

In section 7.4.1 the sheared flow parameterisation was tested using a set of mock production rates and modelled images. For the case of images without noise, the model successfully recovered the input flow parameters with excellent accuracy. At around timestep 60 (see figure 7.4) there is a large increase in the value of the error function. The increase in the error coincides with rapid fluctuations in the recovered parameters for the flow velocities and the orientation of the separatrix. While the cause of these fluctuations is unknown, they do show that the model is able to error-correct somewhat as the error introduced around timestep 60 does not grow. The fluctuations of the flow parameters around this time allow for the under- or overestimated velocities to be corrected by using an over- or underestimated velocity at the next timestep.

The noisy image case was not able to recover the velocities at any individual timestep successfully, but was able to successfully determine the parameters which determine the location and orientation of the separatrix. However, when the time-averaged values of the recovered flow parameters are compared to the input parameters, a reasonable agreement is found. The noise present in the mock images analysed in the noisy case is of the same level as the noise present in the ASK images. The results obtained in the analysis of the mock data show that the flow model should be able to recover a time-averaged value of the flow parameter; however care will need to be taken when interpreting variations in any recovered parameters at short-time scales. As the flow model was able to recover reasonable flow parameters for a sheared flow, it should also be able to recover parameters for a uniform flow as only large scale structure is required in the case of a uniform flow. This large scale structure can be more aggressively filtered to reduce the effects of noise on the optimisation process.

In section 7.4.2 the event on 9 November 2006 was analysed using the uniform flow parameterisation. The velocities of the plasma convection perpendicular to the magnetic field are extracted and compared to radar observations of the plasma velocity from the SuperDARN radar. The average plasma velocity (600 m s^{-1}) and electric field (30 mV m^{-1}) vectors from the four SuperDARN measurements, which are shown in figure 7.7 by the thick black dashed lines, show clear agreement in direction, but with smaller magnitudes than the optically derived values for the plasma velocity and electric field vectors. Due to their lower cadence, the SuperDARN vectors are more likely to be representative of the background plasma convection, rather than the arc-related enhancement in flow obtained from the high cadence optical measurements. Both sets of observations show a southward and eastward convection of the plasma, which is consistent with the large scale dawn-ward convection of plasma which occurs in the night-side hemisphere during the Dungey cycle.

The magnitudes of the SuperDARN velocities are toward the lower end of the range of velocities obtained from the flow model at times when the brightness of the auroral

feature was not enhanced. At the times when the brightnesses of the observed auroral forms are low, there is still electron precipitation occurring and any recovered flow velocity or electric field at this time will be a spatial average over the modelled volume, and not solely the large-scale convection electric field. However, it is not expected that there should be exact agreement between the magnitudes of the SuperDARN and recovered flow parameters. There is an uncertainty of up to 1 minute in the exact time at which the two sets of SuperDARN observations were obtained, both between the radar observations, and between a radar observation and the time of the event observed by ASK. Further, the radar observations have a range resolution of about 45 km, which cover a larger region than is modelled here or visible by the ASK instrument. Therefore the radar estimates of the plasma velocity are interpreted as averages over much larger spatial scales and longer time-scales than the recovered velocities from the flow model. Additionally, the altitude at which the SuperDARN flows are measured depends on the elevation of the radar beam. These factors also mean that is it unlikely that the SuperDARN measurements coincide exactly in either time or altitude in the region surrounding the volume observed by ASK.

Large and dynamic electric fields associated with auroral features have previously been observed using both ground- and space-based instrumentation. However, very few have been at spatial and temporal resolutions that match the present observations. Lanchester et al. (1996) used the EISCAT UHF radars to study the electric field in the vicinity of a small scale auroral arc and found intense fields, of up to 400 mVm^{-1} that pointed toward bright regions of the arc. These radar-derived results were obtained at 3 s resolutions, which were the limits of the radar experiment. A further study, again using the EISCAT UHF radars, analysed an auroral arc composed of several smaller scale features, and found electric fields which point toward the bright feature as the arc approached and receded from the radar beam (Lanchester et al., 1998). Coincident optical observations with these studies showed variations and motions of the auroral arcs on timescales much less than the radar observations of the electric fields. The authors interpreted these optical variations, in the context of the changes of the electric fields with the optical observations, as indicating that even more intense electric fields may exist at shorter timescales. These results formed the initial motivation for the design of the ASK instrument and the motivated the work presented in this thesis.

Further, Lanchester et al. (1997) used a three-dimensional multi-fluid MHD model (Birk and Otto, 1996) to simulate the spatial variation of the ionospheric plasma velocity close to a narrow and dynamic arc filament, similar to that observed in the present event. The simulation includes a magnetic and velocity perturbation at its upper boundary in the inner magnetosphere, which generates field-aligned current sheets. A field-aligned electric field is generated by a resistive term in Ohm's law if the current density exceeds a threshold value. A small-amplitude perturbation is applied to initialize the formation of the acceleration region. In this simulation, the height integrated field-aligned electric

field in the volume, or the potential drop along the magnetic field, is equivalent to the resulting optical arc in the ionosphere. The resulting plasma velocities in the ionosphere are found to be mainly tangential to the arc filaments, with inferred electric fields pointing towards regions of enhanced potential, and with increased magnitudes where the arc is brightest.

In the results and analysis presented here, evidence is found that supports the idea of enhanced fields near bright features. Figure 7.7 shows an enhancement in the strength of the electric field during the brightening, with the largest electric fields found when the brightnesses of the prompt emissions, 673.0 nm and 777.4 nm, are highest. The lack of any significant change in direction of the calculated electric fields is a result of the distribution of the emitting $O^+(^2P)$ ions and the position of the 'bright spot' within the auroral feature during the brightening at 21:25:05.85 UT. As the bright spot brightens, the precipitation in this region intensifies, resulting in intensified electric fields which point towards the spot. The bright spot lies south-west of the distribution of the $O^+(^2P)$ ions, so the electric field at the location of the $O^+(^2P)$ ions should also point south-west. As the convection electric field already points south-west, when the electric field associated with the bright spot intensifies, no change in direction would be observed, only a change in magnitude.

Before moving onto discussion of the sheared flow case, the brightnesses of the modelled images of emission are discussed. The brightnesses of the modelled images presented in figures 7.8 and 7.9 are significantly undermodelled. The 732.0 nm emission is especially sensitive to low energy precipitation, as can be seen in the assumed steady-state emission profiles in figure 4.1. If the emission rates from the 1 keV and 0.1 keV profiles are compared, the 0.1 keV profile produces an emission brightness that is at least 10 times greater than the 1 keV profile. This effect is increased for higher energies. The brightnesses of the modelled images of the 732.0 nm emission are therefore extremely sensitive to the sub-keV precipitation and the low energy tail of the electron energy spectrum. However, in the results presented here no low energy tail is used as modelling of emissions from the ASK instrument is not able to inform any of the low energy tail's characteristics, such as the power law exponent in the tail or the fraction of the energy flux carried by the tail. The absence of a low energy tail in the energy spectra causes the altitude of the 732.0 nm emission to be lower. This lowered emission altitude would result in lower velocities obtained from the model as the lower-altitude distribution of $O^+(^2P)$ ions would not have to convect as far to reach the same position in the modelled image as a higher-altitude distribution. Therefore, the velocities modelled here should be taken as a rough lower-bound.

Additionally, the modelled images exhibit drop-offs in brightness at the edges of the images. These drop-offs are due to the horizontal extent of the region in which the production rates are known being smaller than the horizontal extent of the visible region in the ASK2 camera at the typical altitudes of emission from the $O^+(^2P)$ ion. This effect

cannot be fixed using the current observations, but can be reduced by having the prompt emission observed using a wider field-of-view. Future observations suing a wider field of view will allow the precipitation, and hence production rates, to be characterised over a larger horizontal extent, which will result in the horizontal extent of the modelled $O^+(^2P)$ ion distribution being wider. The wider distribution of ions, and their resulting emission, will more completely fill the modelled volume, reducing the effect of the drop-offs.

As described in chapter 6, the modelled volume used in this analysis is designed for modelling the prompt emissions presented in chapter 6, and only extends to an altitude of 350 km. Referring to figure 4.1 again, it can be clearly seen that for low energy precipitation, a maximum modelled altitude of 350 km clearly neglects a significant fraction of emission from the $O^+(^2P)$ ion for lower energies. Additionally, production of $O^+(^2P)$ ions can occur above 500 km, which is the maximum altitude used in the Southampton ion-chemistry model. These two factors are the reason why the brightnesses of the modelled images for the uniform flow case are undermodelled. The structure of the modelled images reasonably captures the structure of the observed 732.0 nm emission, which suggests that the flow model is able to track the $O^+(^2P)$ ions, despite the deficiencies in the modelling process highlighted above.

The sheared flow parameterisation is not attempted on this event because it does not exhibit sufficient structure in the 732.0 nm emission for the shear method to work. Instead, the shear flow method is applied to the event at 19:32 UT on 12 December 2006, the results of which are presented in section 7.4.3. The recovered flow velocities parallel to the arc, the 'eastern' and 'western' velocities described in the results, are in general poorly modelled. The western velocity rapidly drops to zero and remains stuck at zero for the entirety of the analysed interval. Similarly the cross arc velocity eventually sticks at zero as well. The cause for this sticking to zero is due to the initial guess of the flow parameters for times after the initial timestep.

The initial guess of the flow parameters at the next timestep is set equal to the optimal parameters obtained at the current timestep, so if a parameter goes to zero then the initial guess at the next timestep will also be zero. The Nelder-Mead optimisation can get stuck at zero as it employs an initial simplex, consisting of a 10% increase in the value of each free parameter, as its first step. At values close to zero, any further iterations of the free parameter in the search for the optimal value will also be close to zero, and require many iterations to move significantly away from zero. The number of iterations required to move away from zero may be larger than the maximum number of iterations of the optimisation specified at any given timestep, which causes the optimisation at that timestep to finish before the parameter at zero can move away from zero. To address this drawback in future runs of the flow model, the initial guess of the free parameters at the next timestep should include a simple brute force search of the flow parameters. This search would cover the suspected parameter space of the free flow parameters at a

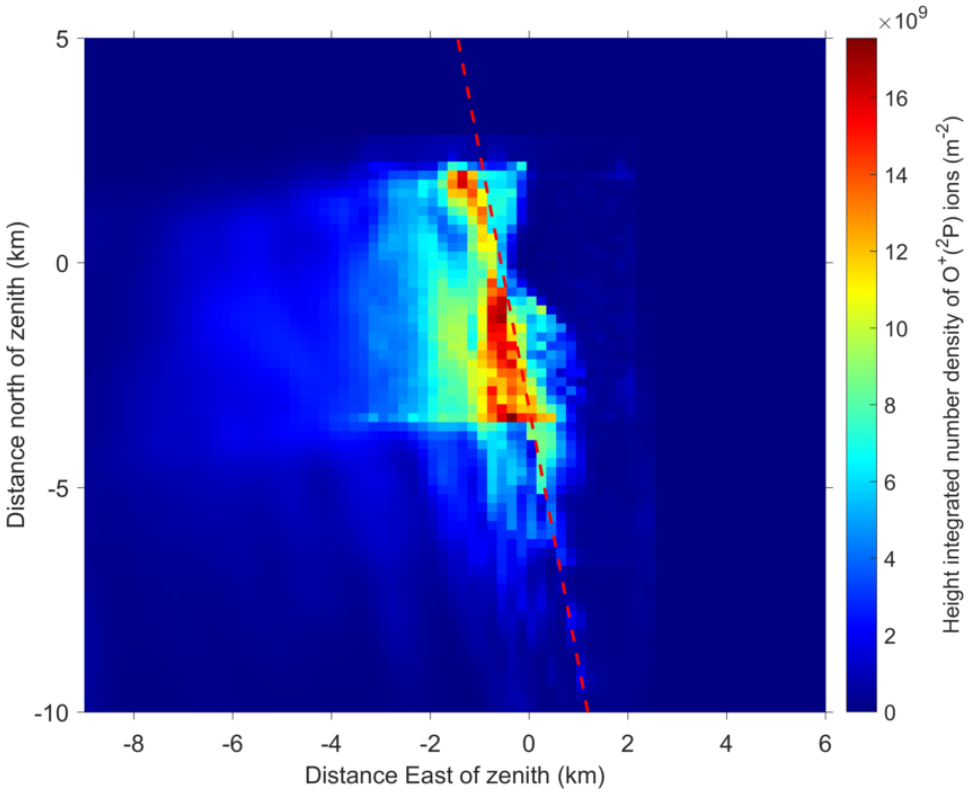

Figure 7.16: Height integrated density of the distribution of $O^+(^2P)$ ions at 19:32:06.5 UT. The red line indicates the position of the separatrix.

very course resolution. The resulting model error values for the optimal parameters from the brute force search and the optimal parameters from the previous timestep should be compared, with the lower error being used as the initial guess for the Nelder-Mead optimisation at this timestep. Such an approach was avoided here as the free-parameter space is large and such brute force searches are time-consuming.

The eastern velocity exhibits large and rapid fluctuations in its optimal value throughout the event. The cause of these fluctuations are likely not physical, and can be explained by examining the height-integrated densities of $O^+(^2P)$ ions. Figure 7.16 shows the height-integrated densities of the $O^+(^2P)$ ions at 19:32:06.5 UT, illustrating the distribution of $O^+(^2P)$ ions perpendicular to the magnetic field. The figure clearly shows the majority of the $O^+(^2P)$ ions are to the west of the separatrix, and thus will be moved only by the western and cross-arc velocities. There is a significantly smaller fraction of $O^+(^2P)$ ions on the eastern side of the separatrix. The distribution of ions with respect to the position of the separatrix means that the modelled distributions, and images of emission from these distributions, are less sensitive to the value of the eastern velocity. This reduced sensitivity makes the error function (equation 7.6) for the parameter space of the eastern velocity much flatter, allowing both large and rapidly changing velocities for the eastern velocity.

7.6 Conclusions

A novel method for estimating plasma velocities using the modelling of the 732.0 nm emission from the metastable $O^+(^2P)$ ion at sub-second resolution is presented. The plasma velocities are parameterised in one of two ways: a uniform convection of plasma perpendicular to the magnetic field, and a more complex sheared plasma flow. This method optimises the velocity of the ions, and hence plasma velocity, to minimize the residual between observed and modelled images of this emission. The method is tested against a set of mock production rates, ion distributions and resulting images of emission, to verify the model can successfully optimise the free parameters using images which exhibit noise at a similar level to observations from the ASK instrument.

The method is applied to the event on 9 November 2006 using the uniform flow parameterisation to determine the plasma velocity during a time of electron precipitation. Plasma velocities are recovered at a cadence of 0.1 s, and are between 0.4 and 2.4 km s^{-1} directed to the south and east. These velocities yield electric fields, calculated from the $\mathbf{E} \times \mathbf{B}$ drift, of between 20 and 120 mV m^{-1} directed to the south and west. The plasma velocities and electric fields are found to be enhanced during rapid brightening of the auroral form. These enhancements are interpreted to be a result of an intensification of the electric field associated with the feature, which is consistent with previous observations of fine scale auroral features (Lanchester et al., 1996, 1998).

These plasma velocities are also compared to co-incident radar observations from the SuperDARN radars. An excellent agreement in direction is found, however the plasma velocities as found by the radars are at the lower end of the velocities recovered from the optimisation. The radar velocities are lower due to the cadence and resolution of the radar observations resulting in significant spatial and temporal averaging, and uncertainties regarding the coincidence, both spatially and temporally, of the radar observations at the time of the observed event. The significant agreement between the radar observations and the results of the optimisation allow the recovered velocities and electric fields to be interpreted as a combination of the large-scale convection and the electric field associated with the observed auroral feature.

The method is also applied to the event on 12 December 2006 using the sheared flow parameterisation, using a timestep of 0.125 s. However this attempt is determined to be unsuccessful as the recovered plasma velocities are not thought to be physical. Although some structure is present in the observations of the 732.0 nm emission, it is not sufficient. Further, the observed brightness of the event is rather low which reduces the contrast of the structure. This method is only able to determine the plasma flows where there are structured distributions of emitting ions which can be modelled and tracked. Therefore future events analysed by this method should exhibit both greater structure and contrast.

Further, the observations of the prompt emissions, from which the electron energy spectra and production rates of the $O^+(^2P)$ ion are modelled, do not span a wide enough region at low altitudes to fully model the production rates of $O^+(^2P)$ ions at higher altitudes. Therefore, further work is required, through improvements to the modelling process and application to events which exhibit greater structuring and brightness, to evaluate the capabilities of the sheared flow parameterisation to determine the plasma flows and electric fields associated with fine scale auroral features.

The results show that the model is able to successfully recover plasma velocities from the ASK observations of the 732.0 nm emission during times of active auroral precipitation. Previous methods of flow extraction have relied on tracking the 'afterglow' emissions after the precipitation had ceased (Dahlgren et al., 2009). Therefore the modelling methods presented here represent a significant advancement in the capability of using observations of the 732.0 nm emission from the $O^+(^2P)$ ion to determine plasma flows and electric fields in the auroral ionosphere.

Chapter 8

Conclusions and Future Work

The techniques presented in this work are required for further investigation of small scale aurora. Aurora are simply the end result of a multitude of physical processes that structure and accelerate the electrons between the magnetosphere and the atmosphere. Better knowledge of the characteristics of the electron precipitation, such as energy and energy flux, and the results of such precipitation on the ionosphere, such as electric field enhancements, are necessary to further understand the process which produce and structure the dynamic fine scale aurora.

Chapters 5 and 6 present the techniques used to estimate the characteristics of the electron precipitation in the region surrounding the magnetic zenith. In Chapter 5 a novel technique that utilises a fusion of optical and radar data is presented. Analysis of an event in which fine scale aurora was observed showed that the optical brightening was more a result of enhanced energy fluxes rather than a change in energy, although a change in energy was also observed. This technique did not correct for any perspective effects, however due to somewhat high energy (6-8 keV) of the electron precipitation and the proximity of the feature to the magnetic zenith, the perspective effects are small.

Chapter 6 presents a similar technique that is intended for use when complementary radar data are unavailable, which renders the technique of chapter 5 unusable. This technique is applied to an event in which an afterglow is clearly present in the observed images of the 732.0 nm emission, indicating the presence of lower energy (keV or sub-keV) electron precipitation. Energy spectra are obtained and the resulting modelled images are compared to the observed images for the prompt emissions only. A quantitative comparison is made, using a measure of similarity called the structural similarity index (SSIM), and it is found that overall the similarity between the modelled and observed images is good, but that there are regions of the modelled auroral feature that are not similar to the observed feature. This is likely because the perspective correction method is not correcting for perspective effects.

The use of the 562.0 nm emission in chapter 5, where the recovered precipitation characteristics are later used in chapter 7, is sub-optimal for estimating the energy flux of low energy precipitation as the 562.0 nm emission brightness is significantly reduced when the energy of the precipitation is sub-keV. At keV energies and greater, the brightness of the 673.0 nm emission is higher than that of the 562.0 nm emission, which reduces the effect of noise on the recovered precipitation charactertics. Therefore, as both emissions can be used in the emission ratio method, the 673.0 nm emission should be used over that of the 562.0 nm emission.

Chapter 7 presents a model, and results from said model, for estimating the ionospheric electric fields at sub-second resolution during periods of auroral precipitation. Plasma velocities are parameterised in one of two ways; either a uniform flow perpendicular to the magnetic field, or a sheared flow across the auroral feature. The uniform flow parameterisation is applied to the event analysed in chapter 7. The recovered plasma velocities are interpreted in the context of radar measurements of the background ionospheric plasma convection, and a good agreement is found. The magnitudes of the velocities from the model are larger than the radar measurements, particularly at times when the brightness of the auroral feature rapidly intensified. This intensification, and the associated changes in the plasma velocity, are interpreted as an intensification in the electric field associated with the auroral feature. The uniform flow assumed here prevents detailed investigation of the electric field due to the auroral feature. The sheared flow parameterisation is applied to the event described in chapter 5, but is found to be unsuccessful.

Modelled images of the auroral emissions at 732.0 nm are found to be significantly undermodelled, by around 50 %, when compared to the observations of the same emission. Two reasons for this are suggested; the size of the volume in which the densities of the emitting ions are modelled, and effects due to the low energy tail of the electron energy spectrum. The modelled volume used for each of the events analysed in chapter 7 are identical to those used in their respective earlier chapters, which terminate at altitudes of between 350-400 km. The altitude dependent lifetime of the $O^+(^2P)$ means that significant quantities of 732.0 nm emission are produced at high altitudes, even beyond the upper altitude limit of the modelled volume. The exclusion of these ions above 350-400 km in the modelling process is a key cause of the undermodelled brightness of the modelled 732.0 nm emission.

The low energy tail is another potential source for the undermodelling of the 732.0 nm emission brightness. The inversion of radar data presented in chapter 5 fits a power-law sub-keV energy tail, or low energy tail. This low energy tail only produced changes in electron densities at higher altitudes, where the effects of convection are more important. As convection of plasma into and out of the radar beam cannot be quantified for the radar measurements here, this represents a significant uncertainty in both the energies and energy fluxes carried by the low-energy tail. The energy spectra used in the modelling

presented in chapter 6 do not have low energy tails. The rationale for excluding the low energy tail is that the characteristics of the tail simply cannot be determined from the observations available from the ASK instrument. In using observed emissions to estimate characteristics of the electron precipitation, one prompt emission or observation is needed per characteristic. With only two prompt emissions available, only two charaacteristics of the precipitation can be found, which here are the total energy flux and the peak energy. Assumptions about the power-law exponent of the tail could be made (Frank and Ackerson, 1971), however even small changes or uncertainties in the energy flux carried by this tail will result in significantly larger changes or uncertainties in the resulting densities of $O^+(^2P)$ ions at high altitudes. Therefore, at least one further simultaneous prompt observation of the aurora, preferably one that is sensitive primarily to low energies, is required to infer the energy content of the low energy tail.

The results from chapter 7 show electric fields that are enhanced when the optical brightness of the auroral feature intensifies. Coincident enhancements in electric fields and optical brightness are an indicator of auroral acceleration as a result of near-Earth magnetic reconnection (Otto and Birk, 1993). The coincident electric field enhancements have been observed (Lanchester et al., 1996), but these measurements were limited to resolutions of many seconds. These temporal limitations have a large effect on the interpretation of electric fields and their resulting effects, such as ionospheric Joule heating. Short and intense electric fields that are averaged over timescale much longer than the duration of the intensification, as a result of the observation method, result in a reduced electric field. With observations at long enough timescales, which for the short-lived fine scale aurora can be as little as 60 seconds, the electric field enhancements are removed entirely. These fields are necessary for calculating the Joule heating, as the amount of Joule heating is proportional to the square of the electric field.

Here, electric fields are determined at unprecedented sub-second resolution, which would allow the electrodynamics of the auroral feature to be investigated in greater detail. However the accuracy of the recovered electric fields is limited by the chosen parameterisation of the flow. A uniform flow, perpendicular to the magnetic field, across the entire modelled volume is used here, resulting in electric fields that are uniform across the entire volume and perpendicular to the magnetic field. Consequently, the obtained electric fields are spatial averages of electric field throughout the modelled volume, which is a serious limitation given the small scale of the observed auroral feature. Despite this limitation, the work provides an important first step in determining the electric fields during active precipitation at sub-second resolution.

8.1 Future work

Despite the issues discussed above, the techniques presented in this thesis represent a significant advance in capability over existing modelling techniques to investigate the ionospheric electric fields using the ASK instrument. However, there is much room for improvement of the modelling techniques used to estimate the energy spectrum of the auroral precipitation and model the emissions of said precipitation. These techniques are currently only applied to one event each and, ideally, should be tested against additional events to further test their accuracy and limits of applicability. Ideally, the verification of these techniques should also be performed using an independent prompt emission, rather than modelling images of the emissions that are used as inputs. Improvements to the techniques, in particular with the perspective correction, which is absent for the combined radar and optics method and somewhat ambiguous as to its effect for the optical only method, are also sought.

Further work is also needed on the flow model. One key improvement would be in the parameterisation of the plasma velocities surrounding the auroral feature. While the current parameterisation, a uniform flow perpendicular to the magnetic field, has been useful to verify the flow model works and can provide results that are in agreement with independent measurements, it is unsuitable for the study of the fine scale electrodynamics of auroral features. The event analysed using the sheared flow parameterisation was unsuccessful. Brighter, more structured event should be sought for testing of the shear flow parameterisation. Validation of any future flow parameterisations is also necessary, and would require a dedicated rocket campaign or satellite conjunction to truly verify the accuracy of the recovered electric fields.

Finally, work is needed to improve knowledge of the low energy tail of the precipitating electrons. This can come from either improvements to the observations or from a statistical study of the low energy tail. Upgrades to the ASK instrument or collaboration with other institutions who also operate small or fine scale auroral imagers are necessary to allow for more than three wavelengths to be imaged simultaneously. Alternatively, direct measurements of electron energy spectra could be studied to determine if there is any statistical relationship between the characteristics of the low energy tail, in particular the energy flux carried by the tail as a fraction of the total energy flux of the precipitation, and other auroral or geomagnetic parameters.

References

Aikio, A., Lakkal, T., Kozlovsky, A., and Williams, P. (2002). Electric fields and currents of stable drifting auroral arcs in the evening sector. *J. Geophys. Res.*, 107(A12).

Akaike, H. (1974). A new look at the statistical model indentification. *IEEE Trans. on Automatic Control*, 19(6):716–723.

Albert, R. D. (1967). Energy and flux variations of nearly monoenergetic auroral electrons. *Journal of Geophysical Research*, 72(23):5811–5815.

Ashrafi, M., Lanchester, B. S., Lummerzheim, D., Ivchenko, N., and Jokiaho, O. (2009). Modelling of $N_2$1P emission rates in aurora using various cross sections for excitation. *Ann. Geophys.*, 27:2545–2553.

Bernhardt, P., Wong, M., Huba, J., Fejer, B., Wagner, L., Goldstein, J., Selcher, C., Frolov, V., and Sergeev, E. (2000). Optical remote sensing of the thermosphere with HF pumped artificial airglow. *J. Geophys. Res.*, 105(A5):10657–10671.

Birk, G. and Otto, A. (1996). A three-dimensional plasma-neutral gas fluid code. *J. Comput. Phys.*, 125:513–525.

Birk, G. and Otto, A. (1997). On the role of macroscopic resistive instabilities in the auroral ionosphere-thermosphere system. *Advances in Space Research*, 20(6):1301 – 1304. Coupling and Energetics in the Stratosphere-Mesosphere-Thermosphere- Ionosphere System.

Borovsky, J., Suszcynsky, D., Buchwald, M., and Dehaven, H. (1991). Measuring the thicknesses of auroral curtains. *Geophys. Res. Lett.*, 44:231–238.

Carr, S. (1992). Remote-sensing observations of F-region drift velocities using Dynamics Explorer-2 doppler measurements of $O^+(^2P)$ 7320nm emission. *Geophys. Res. Lett.*, 19(14):1455–1458.

Chamberlain, J. (1961). *Physics of the Aurora and Airglow*. American Geophysical Union.

Chang, T. (1993). Re-evaluation of the $O^+(^2P)$ reaction rate coefficients derived from Atmosphere Explorer-C observations. *J. Geophys. Res.*, 98(A9):15589–15597.

Chaston, C. C. (2015). Magnetic reconnection in the auroral acceleration region. *Geophysical Research Letters*, 42(6):1646–1653. 2015GL063164.

Chaston, C. C., Peticolas, L. M., Bonnell, J. W., Carlson, C. W., Ergun, R. E., McFadden, J. P., and Strangeway, R. J. (2003). Width and brightness of auroral arcs driven by inertial alfven waves. *Journal of Geophysical Research: Space Physics*, 108(A2):n/a–n/a. 1091.

Chaston, C. C. and Seki, K. (2010). Small-scale auroral current sheet structuring. *Journal of Geophysical Research: Space Physics*, 115(A11):n/a–n/a. A11221.

Chaston, C. C., Seki, K., Sakanoi, T., Asamura, K., Hirahara, M., and Carlson, C. W. (2011). Cross-scale coupling in the auroral acceleration region. *Geophysical Research Letters*, 38(20):n/a–n/a. L20101.

Cowley, S. W. H. (2013). *Magnetosphere-Ionosphere Interactions: A Tutorial Review*, pages 91–106. American Geophysical Union.

Cravens, T. E. (1997). *Physics of Solar System Plasmas*. Cambridge Atmospheric and Space Science Series. Cambridge University Press.

Dahlgren, H., Gustavsson, B., Lanchester, B., Ivchenko, N., Brändström, U., Whiter, D., Marklund, G., Sergienko, T., Sandahl, I., and Marklund, G. (2011). Energy and flux variations across thin auroral arcs. *Ann. Geophys.*, 29:1699–1712.

Dahlgren, H., Ivchenko, N., Lanchester, B., Ashrafi, M., Whiter, D., Marklund, G., and Sullivan, J. (2009). First direction optical observations of plasma flows using afterglow of O^+ in discrete aurora. *J. Atmos. Sol. Terr. Phys.*, 71:228–238.

Dahlgren, H., Ivchenko, N., Lanchester, B., Sullivan, J., Whiter, D., Marklund, G., and Strmme, A. (2008a). Using spectral characteristics to interpret auroral imaging in the 731.9 nm O^+ line. *Ann. Geophys.*, 26:1905–1917.

Dahlgren, H., Ivchenko, N., Sullivan, J., Lanchester, B., Marklund, G., and Whiter, D. (2008b). Morphology and dynamics of aurora at fine scale: first results from the ASK instrument. *Ann. Geophys.*, 26:1041–1048.

Dungey, J. W. (1961). Interplanetary magnetic field and the auroral zones. *Phys. Rev. Lett.*, 6:47–48.

Evans, D. S. (1968). The observations of a near monoenergetic flux of auroral electrons. *Journal of Geophysical Research*, 73(7):2315–2323.

Evans, D. S. (1974). Precipitating electron fluxes formed by a magnetic field aligned potential difference. *Journal of Geophysical Research*, 79(19):2853–2858.

Fontheim, E. G., Stasiewicz, K., Chandler, M. O., Ong, R. S. B., Gombosi, E., and Hoffman, R. A. (1982). Statistical study of precipitating electrons. *Journal of Geophysical Research: Space Physics*, 87(A5):3469–3480.

Frank, L. A. and Ackerson, K. L. (1971). Observations of charged particle precipitation into the auroral zone. *Journal of Geophysical Research*, 76(16):3612–3643.

Gattinger, R., Llewellyn, E., and Jones, A. V. (1996). On i(5577 å) and i(7620 å) auroral emissions and atomic oxygen densities. *Ann. Geophys.*, 14:687–698.

Glosik, J. (1978). Measurement of the rates of reaction of the ground and metastable excited states of O_2^+, NO^+ and O^+ with atmospheric gases at thermal energy. *J. Phys. B At. Mol. Opt. Phys.*, 11:3365–3379.

Goertz, C. K. and Boswell, R. W. (1979). Magnetosphere-ionosphere coupling. *Journal of Geophysical Research: Space Physics*, 84(A12):7239–7246.

Gustavsson, B. (1998). Tomographic inversion for ALIS noise and resolution. *Journal of Geophysical Research: Space Physics*, 103(A11):26621–26632.

Gustavsson, B., Sergienko, T., Rietveld, M., Honary, F., Steen, A., Brändström, B., Leyser, T., Aruliah, A., Aso, T., Ejiri, M., and Marple, S. (2001). First tomographic estimate of volume distribution of HF-pump enhanced airglow emission. *J. Geophys. Res.*, 106(A12):29105–29123.

Hasegawa, A. (1976). Particle acceleration by mhd surface wave and formation of aurora. *Journal of Geophysical Research*, 81(28):5083–5090.

Hecht, J. H., Christensen, A. B., Strickland, D. J., Majeed, T., Gattinger, R. L., and Vallance Jones, A. (1999). A comparison between auroral particle characteristics and atmospheric composition inferred from analysing optical emission measurements alone and in combination with incoherent scatter radar measurements. *J. Geophys. Res.*, 104(A1):33–44.

Hecht, J. H., Christensen, A. B., Strickland, D. J., and Meier, R. R. (1989). Deducing composition and incident electron spectra from ground-based auroral optical measurements: Variation in oxygen density. *J. Geophys. Res.*, 94(A10):13553–13563.

Hecht, J. H., Strickland, D. J., and Conde, M. G. (2006). The application of ground-based optical techniques for inferring electron energy deposition and composition change during auroral precipitation events. *Journal of Atmospheric and Solar-Terrestrial Physics*, 68:1502–1519.

Hedin, A. E. (1991). Extension of the msis thermosphere model into the middle and lower atmosphere. *Journal of Geophysical Research: Space Physics*, 96(A2):1159–1172.

Hunten, D., Roach, F., and Chamberlain, J. (1956). A photometric unit for the airglow and aurora. *J. Atmos. Terr. Phys.*, 8:345–346.

Johansson, T., Marklund, G., Karlsson, T., Liléo, S., Lindqvist, P.-A., Nilsson, H., and Buchert, S. (2007). Scale sizes of intense auroral electric fields observed by cluster. *Annales Geophysicae*, 25(11):2413–2425.

Jokiaho, O., Lanchester, B. S., Ivchenko, N., Daniell, G. J., Miller, L. C. H., and Lummerzheim, D. (2008). Rotational temperature of $n_2{}^+$ (0,2) ions from spectrographic measurements used to infer the energy of precipitation in different auroral forms and compared with radar measurements. *Annales Geophysicae*, 26(4):853–866.

Jones, A. V. (1974). *Optical Emissions from Aurora*, pages 80–177. Springer Netherlands, Dordrecht.

Julienne, P. and Davis, J. (1976). Cascade and radiation trapping effects on atmospheric atomic oxygen emission excited by electron impact. *J. Geophys. Res.*, 81:1397–1403.

Kivelson, M. G. and Russell, C. T. (1995). *Introduction to Space Physics.*

Knudsen, D. J., Donovan, E. F., Cogger, L. L., Jackel, B., and Shaw, W. D. (2001). Width and structure of mesoscale optical auroral arcs. *Geophys. Res. Lett.*, 28(4):705–708.

Lanchester, B., Kaila, K., and McCrea, I. (1996). Relationship between large horizontal electric fields and auroral arc elements. *J. Geophys. Res.*, 101(A3):5075–5084.

Lanchester, B., Rees, M., Lummerzheim, D., Otto, A., Frey, H., and Kaila, K. (1997). Large fluxes of auroral electrons in filaments of 100 m width. *J. Geophys. Res.*, 102(A5):9741–9748.

Lanchester, B., Rees, M., Sedgemore, K., Palmer, J., Frey, H., and Kaila, K. (1998). Ionospheric response to variable electric fields in small-scale auroral structures. *Ann. Geophys.*, 16(10):1343–1354.

Lanchester, B. S., Ashrafi, M., and Ivchenko, N. (2009). Simultaneous imaging of aurora on small scale in OI (777.4 nm) and $N_2$1P to estimate energy and flux of precipitation. *Ann. Geophys.*, 27:2881–2891.

Lanchester, B. S. and Gustavsson, B. (2012). Imaging of aurora to estimate the energy and flux of electron precipitation. *Geophys. Monograph Series*, pages 171–182.

Lanchester, B. S., Rees, M., Lummerzheim, D., A.Otto, Sedgemore-Schulthess, K., Zhu, H., and McCrea, I. (2001). Ohmic heating as evidence for strong field-aligned currents in filamentary aurora. *J. Geophys. Res.*, 106(A2):1785–1794.

Le, G., Slavin, J. A., and Strangeway, R. J. (2010). Space technology 5 observations of the imbalance of regions 1 and 2 field-aligned currents and its implication to the cross-polar cap pedersen currents. *Journal of Geophysical Research: Space Physics*, 115(A7):n/a–n/a. A07202.

Li, X. (1997). A state-selected study of the ion-molecule reactions $O^+(^4S,^2D,^2P) + N_2$. *J. Chem. Phys.*, 106:1373–1381.

Lummerzheim, D. (1987). *Electron transport and optical emission in the aurora.* PhD thesis, University of Alaska.

Lummerzheim, D. and Lilensten, J. (1994). Electron transport and energy degredation in the ionosphere: evaluation of the numerical solution, comparison with laboratory expiments and auroral observations. *Ann. Geophys.*, 12:1039–1051.

Maggs, J. and Davis, T. (1968). Measurements of the thicknesses of auroral structures. *Planetary and Space Science*, 16(2):205 – 209.

Marklund, G., Blomberg, L., Fälthammar, C., and Lindqvist, P. (1994). On intense diverging electric fields associated with black aurora. *Geophys. Res. Lett.*, 21(17):1859–1862.

Marklund, G., Sandahl, I., and Opgenoorth, H. (1982). A study of the dynamics of a discrete auroral arc. *Planet. Space Sci.*, 30(2):179–197.

Marklund, G. T., Ivchenko, N., Karlsson, T., Fazakerley, A., Dunlop, M., Lindqvist, P.-A., Buchert, S., Owen, C., Taylor, M., Vaivalds, A., Carter, P., Andre, M., and Balogh, A. (2001). Temporal evolution of the electric field accelerating electrons away from the auroral ionosphere. *Nature*, 414(6865):724–727.

McFadden, J. P., Carlson, C. W., and Boehm, M. H. (1990). Structure of an energetic narrow discrete arc. *Journal of Geophysical Research: Space Physics*, 95(A5):6533–6547.

McIlwain, C. E. (1960). Direct measurement of particles producing visible auroras. *Journal of Geophysical Research*, 65(9):2727–2747.

Meier, R. R., Strickland, D. J., Hecht, J. H., and Christensen, A. B. (1989). Deducing composition and incident electron spectra from ground-based auroral optical measurements: A study of auroral red line processes. *J. Geophys. Res.*, 94(A10):13541–13552.

Milan, S. E., Yeoman, T. K., Lester, M., Thomas, E. C., and Jones, T. B. (1997). Initial backscatter occurrence statistics from the cutlass hf radars. *Annales Geophysicae*, 15(6):703–718.

Mozer, F. S., Cattell, C. A., Hudson, M. K., Lysak, R. L., Temerin, M., and Torbert, R. B. (1980). Satellite measurements and theories of low altitude auroral particle acceleration. *Space Science Reviews*, 27(2):155–213.

Nelder, J. A. and Mead, R. (1965). A simplex method for function minimization. *The Computer Journal*, 7(4):308–313.

Otto, A. and Birk, G. (1992). The dynamical evolution of small-scale auroral arc phenomena due to a resistive instability. *Journal of Geophysical Research: Space Physics*, 97(A6):8391–8397.

Otto, A. and Birk, G. (1993). Formation of thin auroral arcs by current striation. *Geophys. Res. Lett.*, 20(24):2833–2836.

Palmer, J. (1995). *Plasma density variations in the aurora*. PhD thesis, University of Southampton.

Partamies, N., Janhunen, P., Kauristie, K., Makinen, S., and Sergienko, T. (2003). Testing an inversion method for estimating electron energy fluxes from all-sky camera images. *Ann. Geophys.*, 22:1961–1971.

Partamies, N., Syrjäsuo, M., Donovan, E., Connors, M., Charrois, D., Knudsen, D., and Kryzanowsky, Z. (2010). Observations of the auroral width spectrum at kilometre-scale size. *Ann. Geophys.*, 28(3):711–718.

Rees, M. (1982). The production efficiency of $O^+(^2P)$ ions by auroral electron impact ionization. *J. Geophys. Res.*, 87(A5):3612–3616.

Rees, M. (1989). *Physics and chemistry of the upper atmosphere*. Cambridge University Press.

Rees, M. H. and Luckey, D. (1974). Auroral electron energy derived from ratio of spectroscopic emissions 1. model computations. *Journal of Geophysical Research*, 79(34):5181–5186.

Reiff, P. H., Collin, H. L., Craven, J. D., Burch, J. L., Winningham, J. D., Shelley, E. G., Frank, L. A., and Friedman, M. A. (1988). Determination of auroral electrostatic potentials using high- and low-altitude particle distributions. *Journal of Geophysical Research: Space Physics*, 93(A7):7441–7465.

Richmond, A. D. and Thayer, J. P. (2013). *Ionospheric Electrodynamics: A Tutorial*, pages 131–146. American Geophysical Union.

Roble, R. and Rees, M. (1977). Time-dependent studies of the aurora: Effects of particle precipitation on the dynamic morphology of ionospheric and atmospheric properties. *Planet. Space Sci.*, 25:991–1010.

Ruohoniemi, J. M. and Baker, K. B. (1998). Large-scale imaging of high-latitude convection with super dual auroral radar network hf radar observations. *Journal of Geophysical Research: Space Physics*, 103(A9):20797–20811.

Rusch, M. (1977). The OII (7319-7330 A) dayglow. *J. Geophys. Res.*, 82(4):719–722.

Rydesäter, P. and Gustavsson, B. (2001). Investigation of smooth basis functions and an approximated projection algorithm for faster tomography. *Int. J. Imaging Sys. and Tech.*, 11:347–354.

Sandahl, I., Brandstrom, U., and Sergienko, T. (2008). Fine structure of the aurora. *J. Atmos. Sol. Terr. Phys.*, 70:2275–2292.

Semeter, J. (2012). *Coherence in Auroral Fine Structure*, pages 81–90. American Geophysical Union.

Semeter, J. and Kamalabadi, F. (2005). Determination of primary electron spectra from incoherent scatter radar measurements of the auroral E region. *Radio Sci.*, 40:RS2006.

Sergienko, T. and Ivanov, V. (1993). A new approach to calculate the excitation of atmospheric gases by auroral electron impact. *Ann. Geophys.*, 11:717–727.

Simon-Wedlund, C., Lamy, H., Gustavsson, B., Sergienko, T., and Brandstrom, U. (2013). Estimating energy spectra of electron precipitation above auroral arcs from ground-based observations with radar and optics. *J. Geophys. Res.*, 118:3672–3691.

Smith, R. (1982). Polar cusp ion drift studies through high-resolution interferometry of O^+ 7320-A emission. *J. Geophys. Res.*, 87(A6):4455–4460.

Solomon, S. (1993). Auroral electron transport using the monte carlo method. *Geophys. Res. Lett.*, 20(2):185–188.

Spry, J., Jokiaho, O., Lanchester, B., and Whiter, D. (2014). Modelling $n_2$1p contamination in auroral o^+ emissions. *J. Atmos. Sol. Terr. Phys.*, 107:8–11.

Stasiewicz, K., Bellan, P., Chaston, C., Kletzing, C., Lysak, R., Maggs, J., Pokhotelov, O., Seyler, C., Shukla, P., Stenflo, L., Streltsov, A., and Wahlund, J.-E. (2000). Small scale alfvénic structure in the aurora. *Space Science Reviews*, 92(3):423–533.

Stephan, A. (2003). Quenching rate coefficients for $O^+(^2P)$ derived from middle ultraviolet airglow. *J. Geophys. Res.*, 108(A1):1034.

Strickland, D. J., Meier, R. R., Hecht, J. H., and Christensen, A. B. (1989). Deducing composition and incident electron spectra from ground-based auroral optical measurements: theory and model results. *J. Geophys. Res.*, 94(A10):13527–13539.

Swartz, W. E., Nisbet, J. S., and Green, A. E. S. (1971). Analytic expression for the energy-transfer rate from photoelectrons to thermal-electrons. *Journal of Geophysical Research*, 76(34):8425–8426.

Terrell, C., Hansen, D., and Ajello, J. (2004). The near-ultraviolet and visible emission spectrum of o2 by electron impact. *J. Phys. B At. Mol. Opt. Phys.*, 119(A3):1931–1949.

Tuttle, S., Gustavsson, B., and Lanchester, B. (2014). Temporal and spatial evolution of auroral electron energy spectra in a region surrounding the magnetic zenith. *J. Geophys. Res.*, 37:1931–1949.

Wang, Z., Bovik, A., Sheikh, H., and Simoncell, E. (2004). Image quality assessment: From error visibility to structural similarity. *IEEE Trans. Image Processing*, 13:600–612.

Westerlund, L. H. (1969). The auroral electron energy spectrum extended to 45 ev. *Journal of Geophysical Research*, 74(1):351–354.

Whiter, D. (2008). A study of fine auroral structure in the magnetic zenith. MPhil Thesis, University of Southampton.

Whiter, D., Lanchester, B., Sakanoi, T., and Asamura, K. (2012). Estimating high-energy electron fluxes by intercalibrating reimei optical and particle measurements using an ionospheric model. *J. Geophys. Res.*, 89:8 – 17.

Whiter, D. K., Lanchester, B. S., Gustavsson, B., Ivchenko, N., and Dahlgren, H. (2010). Using multispectral optical observations to identify the acceleration mechanism responsible for flickering aurora. *Journal of Geophysical Research: Space Physics*, 115(A12):n/a–n/a.

Zeippen, C. (1987). Improved radiative transition probabilities for OII forbidden lines. *Astron. and Astrophys.*, 173:410–414.